Université de Montréal

Excitonic behaviour in polymeric semiconductors : The effect of morphology and composition in heterostructures

par
Elham Rezasoltani

Département de Physique
Faculté des arts et des sciences

Thèse présentée à la Faculté des études supérieures
en vue de l'obtention du grade de Philosophiæ Doctor (Ph.D.)
en Faculté des arts et des sciences

Le 8 Janvier, 2016

Université de Montréal
Faculté des études supérieures

Cette thèse intitulée:

Excitonic behaviour in polymeric semiconductors : The effect of morphology and composition in heterostructures

présentée par:

Elham Rezasoltani

a été évaluée par un jury composé des personnes suivantes:

Michel Côté,	président-rapporteur
Carlos Silva,	directeur de recherche
Sjoerd Roorda,	membre du jury
Michael D. Barnes,	examinateur externe
Christian Pellerin,	représentant du doyen de la FES

Thèse acceptée le: . . . . . .

RÉSUMÉ

La compréhension des interrelations entre la microstructure et les processus électroniques dans les polymères semi-conducteurs est d'une importance primordiale pour leur utilisation dans des hétérostructures volumiques. Dans cette thèse de doctorat, deux systémes diffèrents sont étudiés ; chacun de ces systèmes représente une approche diffèrente pour optimiser les matériaux en termes de leur microstructure et de leur capacité à se mettre en ordre au niveau moléculaire.

Dans le premier système, j'ai effectué une analyse complète des principes de fonctionnement d'une cellule photovoltaïque hybride à base des nanocristaux d'oxyde de zinc (ZnO) et du poly (3-hexylthiophène) (P3HT) par absorption photoinduite en régime quasi-stationnaire (PIA) et la spectroscopie PIA en pompage modulé dépendant de la fréquence. L'interface entre le donneur (le polymère P3HT) et l'accepteur (les nanoparticules de ZnO), où la génération de charges se produit, joue un rôle important dans la performance des cellules photovoltaïques hybrides. Pour améliorer le mécanisme de génération de charges du P3HT :ZnO, il est indispensable de modifier l'interface entre ses constituants. Nous avons démontré que la modification d'interface moléculaire avec cis-bis (4, 4′ - dicarboxy-2, 2′*bipyridine*) ruthénium (II) (N3-dye) et α-Sexithiophen-2 yl-phosphonique (6TP) a améliorée le photocourant et la performance dans les cellules P3HT :ZnO. Le 6TP et le N3 s'attachent à l'interface du ZnO, en augmentant ainsi l'aire effective de la surface donneur :accepteur, ce qui contribue à une séparation de charge accrue. De plus, le 6TP et le N3 réduisent la densité de pièges dans le ZnO, ce qui réduit le taux de recombinaison des paires de charges.

Dans la deuxième partie, jai introduit une matrice hôte polymérique de polystyréne à masse molaire ulra-élevée, qui se comporte comme un solide pour piéger et protéger une solution de poly [2-méthoxy, 5- (2´-éthyl-hexoxy) -1,4-phénylènevinylène- PPV] (MEH-PPV) pour utilisation dans des dispositifs optoèlectroniques quantiques. Des travaux antérieurs ont montré que MEH-PPV en solution subit une transition de conformation, d'une conformation enroulé à haute température (phase bleue) à une conformation de chaîne étendue à basse température (phase rouge). La conformation de la chaîne étendue

de la solution MEH-PPV favorise les caractéristiques nécessaires à l'amélioration des dispositifs optoélectroniques quantiques, mais la solution ne peut pas être incorporées dans le dispositif. J'ai démontré que la caractéristique de la phase rouge du MEH-PPV en solution se maintient dans une matrice hôte polymérique de polystyrène transformé de masse molaire très élevée, qui se comporte comme un solide (gel de MEH-PPV/UHMW PS), par le biais de la spectroscopie de photoluminescence (PL) dépendant de la température (de 290 K à 80 K). La phase rouge du gel MEH-PPV/UHMW PS se manifeste par des largeurs de raie étroites et une intensité augmentée de la transition $0-0$ de la progression vibronique dans le spectre de PL ainsi qu'un petit décalage de Stokes entre la PL et le spectre d'absorption à basse température.

Ces approches démontrent que la manipulation de la microstructure et des propriétés électroniques des polymères semi-conducteurs ont un impact direct sur la performance de dispositifs pour leurs développements technologiques continus.

Mots clés : polymères semi-conducteurs, exciton, polaron, microstructure, modification d'interface, spectroscopie, P3HT :ZnO, MEH-PPV, photoluminescence, absorption photoinduite

ABSTRACT

Understanding the interrelations between microstructure and electronic processes in polymeric semiconductors is of great importance for their use in bulk heterostructures, as the active part of power-converting devices such as organic photovoltaic cells or light emitting diodes, as well as for quantum optoelectronics applications. In this doctoral thesis, two different systems are investigated; each of these systems represents a different approach to optimize materials in terms of microstructure and their ability to order on the molecular level. In the first system, by means of quasi-steady-state photoinduced absorption (PIA) and pump-modulation-frequency-dependent PIA spectroscopy, I performed a comprehensive analysis of the working principles of a hybrid photovoltaic cell based on nanocrystals of zinc oxide (ZnO) and poly(3-hexylthiophene) (P3HT). The interface surface area between donor (polymer P3HT) and acceptor (ZnO nanocrystals), where charge generation occurs, plays a significant role in the performance of the hybrid photovoltaic cells. To improve the charge generation mechanism of P3HT:ZnO, it is therefore essential to modify the P3HT:ZnO interface area. We demonstrated that molecular interface modification with cis-bis(4,4′-dicarboxy-2,2′bipyridine) ruthenium (II) (N3-dye) and α-Sexithiophen-2-yl-phosphonic Acid (6TP) as interface modifiers enhanced the photocurrent and performance in P3HT:ZnO cells. 6TP and N3 attach to the ZnO interface, thus increasing the donor:acceptor interface area that contributes to enhanced charge separation. Furthermore, 6TP and N3 reduce the ZnO traps that reduces recombination.

In the second part, I introduced a processed solid-like ultra-high-molecular-weight polystyrene polymeric host matrix to trap and protect poly [2-methoxy, 5-(2'-ethyl-hexoxy)-1,4-phenylene vinylene-PPV] (MEH-PPV) solution for use in quantum optoelectronic devices. Previous work by others has shown that MEH-PPV in solution undergoes a conformation transition from coiled conformation at high temperatures (blue-phase) to a chain-extended conformation at low temperatures (red-phase). The chain-extended conformation of MEH-PPV solution favours the characteristics needed to improve quantum optoelectronic devices, however the solution cannot be incorporated

into the device. We demonstrated that the red-phase feature of MEH-PPV in solution maintains in a processed solid-like ultra-high-molecular-weight polystyrene polymeric host matrix (MEH-PPV/UHMWPS gels), by means of temperature-dependent photoluminescence (PL) spectroscopy (ranged from 290 K down to 80 K). The red-phase of MEH-PPV/UHMW PS gels manifest itself as narrow linewidths and enhanced $0-0$ line strength in the PL spectrum as well as a small stokes shifts between the PL and absorption spectra at low temperatures. These approaches demonstrate that microstructure manipulation and electronic properties of polymeric semiconductors have a direct impact on the device performance for their continued technological developments.

Keywords: polymeric semiconductors, exciton, polaron, microstructure, interface modification, P3HT:ZnO, MEH-PPV, spectroscopy, photoluminescence, photoinduced absorption.

CONTENTS

LIST OF TABLES

LIST OF FIGURES

LIST OF APPENDICES

LIST OF ABBREVIATIONS

OLED	Organic light emitting diode
OPV	Organic photovoltaic
P3HT	3-hexylthiophene
ZnO	Zinc oxide
N3	cis-bis(4,4′-dicarboxy-2,2′bipyridine) ruthenium (II)
PL	Photoluminescence
6TP	α-Sexithiophen-2-yl-phosphonic Acid
MEH-PPV	2-methoxy, 5-(2'-ethyl-hexoxy)-p-phenylenevinylene
UHMW	Ultra high molecular weight
M_W	Molecular weight
HOMO	Highest occupied molecular orbital
LUMO	Lowest unoccupied molecular orbital
D	Donor
A	Acceptor
PCE	Power conversion efficiency
J_{SC}	Short circuit current density
V_{OC}	Open circuit voltage
QCNs	Quantum confined nanomaterials
CB	Conduction band
VB	Valence band
PIA	Photo-induce absorption
e	electron
h	hole
2DPC	Two-dimensional photocurrent
2DPL	Two-dimensional photoluminescence
FF	Fill factor

To my beloved mom

Research is what I'm doing when I don't know what I'm doing.

Wernher von Braun

ACKNOWLEDGMENTS

I would like to extend my sincerest thanks and regards to all those who supported me in reaching the PhD level.

First and foremost, I owe immense gratitude to my adviser Professor Carlos Silva. Carlos is a great scientist, full of new ideas, always supportive and understanding, with never ending optimism. Besides being a wonderful study leader, I am deeply touched by his generosity in showing others the right way and making a path for them to success. I consider myself extremely fortunate to be part of Carlos' research group where I have been exposed to a world-wide science network, have overlapped with and got to know many other world-leading groups in the field and collaborated closely with them. I hope in the future I will be able to do the same for others. I will forever remain grateful to him.

I am infinitely thankful to Professor Natalie Stingelin (department of materials, Imperial College London) for providing me the opportunity to join her group in 2015 for four months. I appreciate the time she dedicated, the scientific meetings and discussions and the ideas that were developed through her supervision. Natalie is a wonderful scientist and amazing woman. Thank you so much Natalie.

My particular gratitude goes to Dr. Jaime Martin Perez whom I can never thank enough for his support and for generously sharing his time and knowledge. Jaime is a brilliant chemist and a wonderful mentor to me and his input and advice in material processing, specially in processing protocols of the polystyrene gel helped me to start this interesting project that will lead to a publication. I will always value what I have learnt from him.

My gratitude extends to Dr. Ian Hill (physics department, Dalhousie university, leader of the project 04, PV innovation network) for our successful collaboration that have led to a publication. I am also grateful to Ian for hosting me in his group and providing me with the opportunity to learn about material processing and device fabrications and having a fruitful discussion about our project. Thank you to Yousef Alattar for hosting me at Dalhousie university for a week and for very fruitful discussions.

I would like to extend my thanks and regards to my publication co-author Dr. Mingqing Wang for her endless support. Mingqing is a great collaborator, always being ready to answer questions and clear confusions.

I would like to thank my PhD thesis committee members, Professor Michael Barnes, Professor Michel Côté and Professor Sjoerd Roorda who kindly accepted to read my PhD. thesis and to be my opponent. My particular gratitude goes to Professor Michael Barnes for accepting to travel to Montreal for my defence that makes me feel so much better than having an Skype viva with him.

During the past several years at UdeM, I have been closely working with many people as colleagues; I would like to thank them all for their collaboration, help and team work, specially those whom I became very good friends with. I would like to specially thank Claudia, Elizabeth, Pascal, Felix, Aurelie and Mariam.

My particular gratitude goes to Dr. Claudia Marcela Bazan our great chemist for always being helpful, we started a friendship that I hope will last for much longer than these 3 years.

I would like to thank Claudia, Elizabeth and Reza Mousavi Askari for friendship, great conversations, the tea breaks, for being fun and cooperative in the office.

My particular gratitude goes to Dr. Gianluca Latini for a fruitful discussion, about pump-modulation frequency dependent experiments. Gianluca passed away unexpectedly and there are no words to express all my feelings about this big shock.

Furthermore, I am grateful to Professor Michel Côté for being supportive and always being in physics department to help when no one else is. I will never forget wonderful Christmas parties at his home. I also thank Professor Richard Leonelli director of department for always having a smile, never looking frustrated and being patient and helpful to students. I would like to thank members of the University who have directly contributed to to make my life easier at UdeM. Lynda, Anne, Louis, Tierry, Jacquline, Colin, specially people who have directly contributed to the experimental apparatuses, Robert who built many pieces of custom electronics and Jean-Sebastien who assisted in building many crucial pieces of scientific machinery.

My high school friends have been an invaluable part of my life. I would like to thank

them all for their friendship, encouragement and support. I would like to thank my lovely friend Minoo Eslami and her wonderful family (Farhood and Michael Khaghani) who throughout the years have been my family in Montreal. I would like to acknowledge Alireza Mesgar and Dr. Safa Shoai for being supportive and helpful. Some people come into your life for a season but remain as your friends for a lifetime; thank you Ardalan Armin!

I would like to thank Dr. Mehdi Ghazisaeedi for being a wonderful friend, for being there in my rainy and sunny days, and for his help and support.

I can not begin to thank my wonderful family for all their motivation, encouragement, support, love and much more. I extend my thanks to my lovely brothers Ali and Mehdi Rezasoltani without whom I could not be here, Indeed! I am grateful to have a kind and peaceful sister in law, thank you Atefeh Ghazvini.

Last but not least I am grateful to have a great mom, for her endless support, and love. I dedicate this PhD. thesis to my beloved mom.

CHAPTER 1

INTRODUCTION

Polymeric semiconductors have emerged as a new class of solution processable film-forming semiconductors and been used as active components in a range of optoelectronics devices including light harvesting and emitting systems. The application of polymeric semiconductors are extremely divergent, ranging from organic light-emitting diodes (OLED) to organic photovoltaic cells (OPV), organic field-effect transistors, sensors, quantum optoelectronics and photonics. Polymeric semiconductors have been widely used as insulating materials for a long period of time. Later in the 1970s the conductivity of oxidised polyacetylene was discovered by Heeger et al. [1] and more organic semiconductors based on conjugated molecules and polymers were developed since. The appeal of polymeric semiconductor devices is clear, but technology such as solar cells are limited by relatively low efficiencies of such devices, due to the limitations in electro-optical properties of these materials.

Polymeric semiconductors are disordered systems in which charge carriers experience many trap states and random potential landscape during the transport causing the efficiency of such devices to be affected by structural and energetic disorder. [2] In spite of more than two decades of intensive work, the influence and the mechanism of the disorder, in its broad definition, on different processes such as charge transport, charge transfer, energy transfer, exciton migration, etc. in devices is yet to be fully understood. The disorder is strongly dependent on the microstructure. As the active component of polymeric semiconductor devices are typically made into thin-films, the performance of devices is consequently critically dependent on the morphology through disorder and film structure. Controlling the solid-state microstructure (including crystallite size, chain orientation, π-stacking length, degree of crystallinity, domain size and the thermodynamics of the phase separation in donor/acceptor blends, etc) of this interesting class of materials has been found to be one of the key challenges in the field of organic optoelectronics.

In fact, development of a rigorous understanding of the intimate relationship between microstructure and electronic properties of the active component of polymeric semiconductor devices is a critical first step to further improve organic optoelectronics. Fundamental understanding can be gained by employing a series of optical spectroscopy tools and applying them on model systems with carefully-controlled structures.

1.1 Contribution and objectives of this work

The work presented in this thesis addresses this obvious need through the study of excitonic behaviour in polymeric semiconductors by relating molecular order and conformational arrangements in polymeric semiconductors with optoelectronic characteristics. This knowledge contributes to render device fabrication reproducible and reliable, limiting empirical procedures towards device optimisation.

The aim of this work is to develop an understanding of elementary excitations and dynamics in polymeric semiconductors by adopting steady-state optical spectroscopy. Steady-state optical spectroscopy is a valuable tool to explore the link between electronic structure and solid-state microstructure/phase morphology. This is done through interpreting spectral line-shapes revealing the nature of intra- and intermolecular electronic coupling, the spatially correlated disordered energy landscape, and relate information on exciton spatial coherence lengths, charge generation and recombination. The complex microstructure exists in both neat polymers (e.g. P3HT in amorphous and crystalline phase) and blended polymers (e.g. P3HT: PCBM). More specifically two different systems are investigated; each represents a different approach to optimise materials in terms of microstructure and their ability to order on the molecular level.

The first part of this work investigated the effect of the compositions of heterostructures on their morphology through the focus on the organic photovoltaic cells. The concept of the organic bulk heterostructures photovoltaic cells, where two organic semiconductors are blended to form an interpenetrating network to facilitate exciton dissociation have led to intensive research activities. It is important to note that the donor-acceptor interface in bulk heterostructure determines the kinetics of charge carrier recombination

and how efficiently excited states can be separated into free charge carriers.

Inorganic semiconductors have several advantages compared to organic semiconductors, such as the broader absorption spectrum, energy can be tuned through the quantum confined effect and nanocrystals can be doped to a specific level. Therefore, it is possible to take the advantage of both materials with combining polymeric semiconductors and inorganic semiconductor nanocrystals for photovoltaic applications, while the advantages of a bulk heterostructures can be preserved. In spite of their potential, to date such cells display lower efficiency, especially lower photocurrent, compared to fully organic cells. [3, 4]

The question is that can the efficiency of hybrid photovoltaic cells be improved by using the interface modification procedure?

Therefore, it is our attempt to answer this question in chapter 4. The active component of the organic photovoltaic cells can be either the blend of conjugated polymers or polymer-nanocrystals (will be discussed in chapter 2.3), we investigated the influence of the interface modification on the hybrid photovoltaic cells based on polymer P3HT and ZnO nanocrystals. This part of the work is motivated by Fig. 1.1, as an experimental preview of chapter 4, that shows how the open circuit voltage and short circuit current have changed after interface modification. Hence, it is essential to study the electrical and photovoltaic characterisation of the hybrid photovoltaic cells (shall be discussed later in chapter 4). As demonstrated by the current density-voltage characteristics, both the short-circuit current (J_{sc}), and the open circuit voltage (V_{oc}) are significantly improved through the molecular interface modification by attaching cis-bis(4,4′-dicarboxy-2,2′bipyridine) ruthenium (II) (N3-dye) and α-Sexithiophen-2-yl-phosphonic Acid (6TP) molecules to the interface of ZnO. In order to study the phenomenon that support this improvement, an essential requirement is to understand the response of the polymer to photon absorption and also investigate charge dynamics at the interface of P3HT: ZnO by performing a series of steady-state absorption and photoluminescence measurements. Combination of those measurements and microstructure characterisation enable us to relate the microstructure changes after interface modification to the electronic and optical properties of the bulk heterostructure. That also allows us to understand the

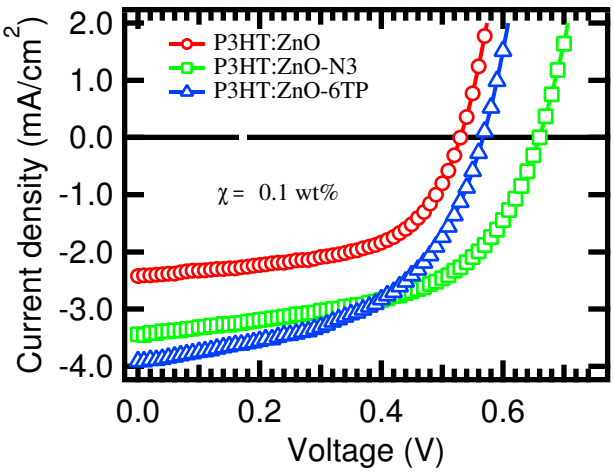

Figure 1.1 – Current density-voltage characteristics of hybrid photovoltaic cells based on P3HT: ZnO, with and without N3 and 6TP interface modifiers under solar illumination intensity of $\sim 100\,\mathrm{mW/cm^2}$.

mechanism of charge generation and recombination (unimolecular and bimolecular) at the interface. Moreover, it enables us to identify the life time of the long-lived polarons and demonstrate that the average lifetime of polarons become longer after the interface modification. We conclude that interface modification reduces the traps and decreases recombination of the charges at the interface and increases the open circuit voltage.

This knowledge, ultimately, leads to the advancement of the power conversion efficiency of organic solar cells and the answer to the first question is yes.

The second part of this work investigated the development of solution-based processing materials for quantum-optoelectronics applications. Controlling the conformational-dependent properties of a conjugated polymer as well as understanding of the interactions between conjugated polymer chains in high-concentration solutions or films are important in optimising deposition and processing techniques of films for conjugated polymer-based quantum-optoelectronic devices such as optically active materials to be used in photonics. Poly(2-methoxy, 5-(2'-ethyl-hexoxy)-p-phenylenevinylene) (MEHP-PV) polymer has shown interesting conformation properties in solution such that proven to be potential candidate for quantum-optoelectronic applications. Given that the solution can not be incorporated in the devices, I have thus processed a potentially alternative

gel-processed MEHPPV in ultrahigh-molecular-weight polystyrene (UHMW PS). The viscosity of the gels was characterised by the rheology tests.

The question is that can the interesting conformational properties of MEHPPV solution be retained in UHMW PS gels?

In order to relate the microstructure of MEH-PPV to the electronic and optical properties to conclude that MEH-PPV polymer shows J-aggregate type behavior we adopted a series of steady-state absorption and temperature-dependent photoluminescence measurements. Figure 1.2, as an experimental preview of chapter 5, represents the PL spectra of MEH-PPV/UHMW PS gels at room temperature versus at 80 K. It is clear that

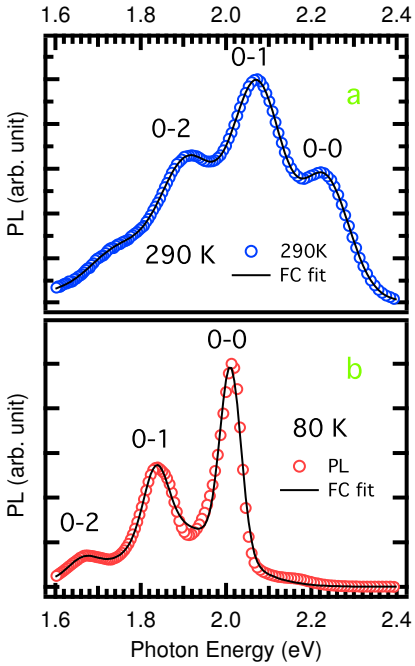

Figure 1.2 – Franck-Condon analysis to the spectra at 290 K (a) and at 80 K (b) for MEH-PPV/UHMW PS gels wt% 3.0 solution containing 5.0×10^{-5} M. The PL spectra (circles), and the solid line shows the Frank-Condon fit. The $0-0$, $0-1$ and the $0-2$ peaks are shown.

the PL spectral shape as well as the ratio of vibronic progressions undergo a change by decreasing temperature. Due to the fact that the excitonic coupling corresponds to the orientation of the electronic dipole moments of the choromophores, it is possible to relate those features to the microstructure of MEH-PPV polymer in the gels. The hybrid "HJ" aggregate model relates the microstructure to the ratio of the vibronic progressions and provide tools to distinguish between the polymer H- and J-aggregation from absorption

and PL spectra. In addition Franck-Condon principle supports the origin of the vibronic progressions. These theories assist us with analysing all theses characteristics and interpret the results of absorption and temperature-dependent PL measurements. Various parameters such as Huang-Rhys parameter, electronic transition peak energy (E_{0-0}), and the Gaussian line width can be excluded via a fit with Franck-Condon model. Moreover, calculation of the exciton coherence length contributes to respond to the second question and the answer is yes.

In this thesis I am going to first present the fundamental notion of the excitation (excitons) in polymeric semiconductors and how the excitonic behaviour is dependent on the microstructure, as well as how it is possible to control this behaviour. In fact, the major part of my study can link material processing to the device fabrication, *i.e.* fundamental study of interrelation between the microstructure and electronic properties of active layers of polymeric semiconductors and/or their blends before being translated into devices. In a big picture, the two sections of my works come together and I conclude that it is possible to control charge generation and recombination dynamics as well as the conformation and aggregations of the active layers of polymeric semiconductors by tailored morphology.

1.2 Organisation of this thesis

Chapter 2 provides the general definition and concepts that represent the theoretical basis of the experimental results discussed in chapters 4 and 5. Chapter 2 is divided into three sections.

1) Polymeric semiconductors: that comprises an overview of the polymeric semiconductors, excitons type and major photoexcitation in polymeric semiconductors.

2) Excitonic behaviour in aggregated polymers: that comprises how the transition dipole moment orientations of chromophores contributes to the formation of H- and J-aggregates and different excitonic couplings and behaviors in polymeric semiconductors. Moreover, the Franck-Condon principle and the concept of polaronic excitons due to the presence of combination electronic and vibrational degrees of freedom is discussed. This part is the basis of the "HJ" hybrid model mainly discussed and used in chapter 5. That enables us to interpret the origin of strong vibronic progressions in the absorption and photoluminescence spectra of polymeric semiconductors with π-conjugation. This knowledge is required to distinguish the H and J-aggregated polymers and relate the microstructure to the electronic properties, specifically in chapter 5 of this thesis.

3) Heterostructures: that comprises the background of polymeric active layers in organic devices. Firstly, the single and bilayer active layers and their problem related to the charge dynamics and separation in organic photovoltaic cells is overviewd. This section also presents the concept of bulk heterostructures as well as the advantages of blended polymers in bulk heterostructures versus the single and bilayer active layers. Moreover, two types of bulk heterostructures; pure organics and organic-inorganic has been discussed. This part has been expanded in chapter 4 through the focus on the interface of the bulk heterostructures with the ultimate goal to modify the interface and improve charge separation in organic photovoltaic cells based on P3HT: ZnO.

Chapter 3, explains the required experimental techniques to characterise the optical and electronic properties of the samples in chapters 4 and 5 of this thesis.

Chapter 4, firstly, introduces the materials which were used during the course of this part of the work. Material processing for hybrid bulk heterostructures is described. Ad-

ditionally, experimental results related to the microstructure characterisation before and after interface modification are explained in this chapter. The working principle of hybrid photovoltaic cells as well as the photovoltaic characteristics of the cell is discussed. The results of electrical characterisation of P3HT:ZnO hybrid photovoltaic cells before and after interface modification is demonstrated. The interrelation between the improvement of power conversion efficiency of the solar cells and the microstructure alteration after interface modification is investigated in this chapter. This study has been conducted through the study of photophysical properties of those materials. Charge generation and recombination processes have been discussed through the rate equation model. This enables us to interpret and analyse the pump modulation frequency dependent measurements as well as pump intensity dependent measurements. The combination of these two experiments and the data analysis assist in investigation of charge dynamics in P3HT: ZnO cells before and after interface modification. The discussion at the end of the chapter provides a response to the question.

Chapter 5, introduces processing protocols for ultra high molecular weight polystyrene gels as well as preparation of MEH-PPV/ ultra high molecular weight polystyrene gels. The "HJ" hybrid model as well as Franck-Condon analysis has been discussed. The results of temperature-dependent PL spectroscopy have been analysed to ultimately relate the excitonic behaviour in the gel to the microstructure changes due to the temperature. At the end it is concluded that interesting red-phase properties of MEH-PPV solution can be retained in the gel.

In chapter 6 the results are summarised. Moreover, an outlook is given.

CHAPTER 2

THEORETICAL FRAME WORK AND BACKGROUND

2.1 Polymeric semiconductors

A conjugated polymer is a long chain of repeating subunit molecules connected by covalent chemical bonds which is mostly composed of carbon, such that the ground state electronic configuration of carbon is $1s^2 2s^2 2p^2$. A particular molecular structure combination of s and p orbitals favours formation of hybrid orbitals which support a different spatial energy orientation compared to non-hybrid orbitals. The bond between carbon atoms can be single, double, or triple depending on the type of hybridization. In sp^2 hybridisation the bond between carbon atoms is double consisting of σ- and π-bonds. The remaining two valence electrons from each carbon atom make σ-bonds with side groups. The σ-bonds lie in the same plane whilst the π-bond is perpendicular to that plane. The σ-bonds are strong and determine the shape of the backbone, whereas π-electrons of $2p_z$-orbitals are loosely bound, delocalised over a number of intrachain carbon atoms, and primarily responsible for the electronic and optical properties of the polymers. Polymeric semiconductors form molecules similar to benzene with filled and vacant molecular orbitals, analogous to valence and conduction bands of inorganic semiconductors.

According to the Pauli exclusion principle, the hybrid bonds are filled up to the highest occupied molecular orbital (HOMO). The next molecular orbital above HOMO is called the lowest unoccupied molecular orbital (LUMO). Therefore the electronic transition occurs where the photon is absorbed between the HOMO and LUMO. The gap between HOMO and LUMO is comparable with the band gap of most of the semiconductors ($\sim 2\,\text{eV}$) [5] which is matched to the photon energy in the visible range of electromagnetic spectrum ($\sim 1.60 - 3.25\,\text{eV}$). Fig. 2.1 shows Ethene as a conjugated π-electron system with σ- and π-bonds along with the energy levels of a π-conjugated molecule. The lowest electronic excitation is between the bonding π-orbital and the anti-

bonding π^*-orbital. The transition between σ and σ^* bonds requires much higher energy than transition between the π and π^* due to the differences in their coupling strengths.

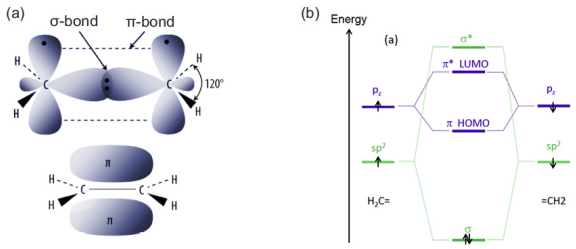

Figure 2.1 – (a) Ethene is the most simple example of a conjugated π-electron system with σ- and π-bonds. (b) The scheme shows the energy levels of a π-conjugated molecule. The lowest electronic excitation is between the bonding π-orbital and the antibonding π^*-orbital.

2.1.1 Absorption in polymeric semiconductors

π-electrons can interact with electromagnetic radiation with incident photon energy higher than the energy bandgap in polymeric semiconductors *i.e.* $\hbar\omega > E_{LUMO} - E_{HOMO}$. The absorption of a photon has the effect of exciting a π-electron of the HOMO band to the LUMO band of a molecule. This interaction refers to the perturbation of the ground state hence it can be evaluated in the framework of the perturbation theory. The electromagnetic perturbation is simply given by

$$H_{dipole} = \vec{\mu}.\vec{E}. \tag{2.1}$$

This Hamiltonian describes the coupling between the electric field of the incident light, $\vec{E} = E_0 cos(\omega t)\hat{k}$, and the electric dipole moment of the molecule, $\vec{\mu} = -e\sum_j \vec{r}_j$. The spatial dependence of the electric field is negligible due to the extended excitation wave length (λ) compared to the intermolecular distance. Based on the Fermis's golden rule, the rate of transition from initial (ground) to final (excited) state is given by

$$T_{i\to f} = \frac{2\pi}{\hbar}\left|\left\langle \psi_f \left| \hat{H}_{dipole} \right| \psi_i \right\rangle\right|^2 \rho_f \delta\left(E_f - E_i - \hbar\omega\right), \tag{2.2}$$

where ψ_i and ψ_f indicate the initial and final states wave functions respectively, ρ_f is density of final state, E_f and E_i the energy of final and initial state respectively, $\hbar\omega$ the energy of incident light. If the symmetry of the initial and final state cause the $\left|\left\langle \psi_f \left| \hat{H}_{dipole} \right| \psi_i \right\rangle\right|^2$ to be zero, thus the electronic transition is forbidden by symmetry.

2.1.2 Excitons in polymeric semiconductors

"An exciton is a quasi-particle that forms when Coulomb-interacting electrons and holes in semiconductors are bound into pair states". [6] Excitons are therefore classified as Frenkel and Wannier-Mott. When an excited electron resides within its molecule or chromophore, the exciton is called a Frenkel exciton. When the excited electron has the ability to range over the molecules surrounding the ionised molecule, it is called a Wannier-Mott exciton. See Fig. 2.2.

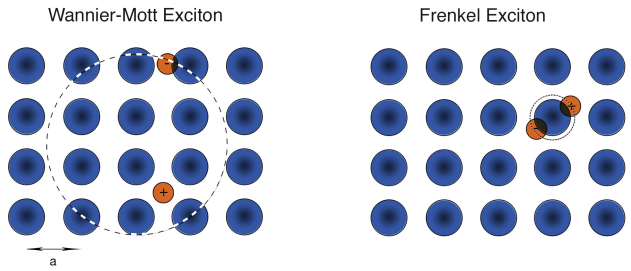

Figure 2.2 – Scheme of the Bohr radius a_0 in Wannier-Mott and Frenkel excitons. a is lattice constant. Wannier-Mott exciton characterises $a_0 \gg a$ while in Frenkel exciton $a_0 \sim a$.

Due to the low dielectric constant in polymeric semiconductors, the Coulomb attraction between electrons and holes is not effectively screened compared to inorganics. This results in a more tightly bound exciton with higher binding energy in polymeric semiconductors, known as Frenkel exciton. Hence, the exciton in polymeric semiconductor is a Frenkel exciton.

2.1.3 General description of Frenkel excitons

To explain the concept of Frenkel exciton in an aggregated molecule, we consider a linear crystal containing N identical molecules such that interactions exist between the nearest neighbours in the linear crystal. Only one molecule is assumed to be electronically excited while all others remain unexcited in the ground state. When the intermolecular interaction is negligible, the wave function of N aggregated molecules within the crystal is the product of the excited state molecule and other $N-1$ molecules residing in the ground state. The identical probability of the excitation of each molecule contributes to a N-fold degenerate band. The electronic state of the system gives rise to

$$|n\rangle = |g\rangle_1 |g\rangle_2 ... |e\rangle_n ... |g\rangle_{N-1} |g\rangle_N , \tag{2.3}$$

where $|n\rangle$ is the state of nth molecule where is in the excited state, whilst the other N-1 molecules are in the ground state, the subscripts indicate molecular sites and g and e are electronic ground and excited states respectively on a single molecule. It is therefore possible to write the total wave function of the system as a linear combination of the states

$$|\psi\rangle = \sum_{n=1}^{N} C_n |n\rangle , \tag{2.4}$$

where C is a complex coefficient such that $\sum_{n=1}^{N} C_n C_n^* = 1$. When the size ($N$) of the chain is large, periodic boundary conditions can be applied. In this case, the eigenstates are expressed as Bloch wave functions with a wave vector k:

$$|\psi_k\rangle = \frac{1}{\sqrt{N}} \sum_n \exp(ikn) |n\rangle , \tag{2.5}$$

where $k = \frac{2\pi}{N} j$, $j = 0, 1, 2, ...N-1$. When the nearest neighbour interactions (excitonic coupling J_0) are activated, the degeneracy between the states will be removed and all the states will form delocalised excitonic states. The interaction Hamiltonian is given by

$$H_{interaction} = \sum_n J_0 \{ |n\rangle \langle n+1| + |n\rangle \langle n-1| \} . \tag{2.6}$$

Therefore, solution to the eigenfunction equation $H\psi_k = E_k\psi_k$ gives rise to

$$E_k = \langle \psi_{k'} | H_{interaction} | \psi_k \rangle = 2J_0 cos(k)\delta_{k,k'}, \tag{2.7}$$

the bandwidth W equals $4J_0$ due to the range of eigenvalues, $-2J_0 < E_k < 2J_0$ that is independent of the aggregates size *i.e.* N as long as $N > 2$. For the dimer $N = 2$, the band width is $W = |2J_0|$ since there is only one nearest neighbour for each molecule. Therefore, exciton coupling, J_0, between the molecules in the crystal raises the energy levels compared to the non-interacting crystal. [7] Fig. 2.3 shows the impact of intermolecular coupling on the energy levels of molecular crystals as well as how the nearest neighbour coupling between molecules shifts the energy levels of the isolated crystal and the band width becomes $4J_0$.

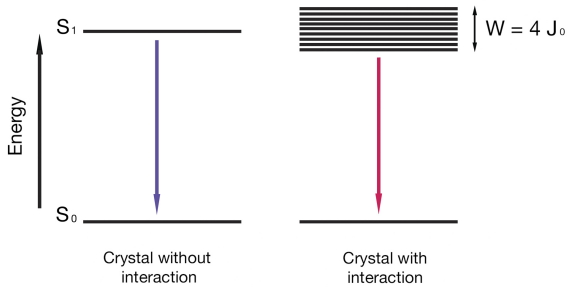

Figure 2.3 – Scheme of the impact of intermolecular coupling on the energy levels of molecular crystal. Nearest neighbour coupling between molecules shifts the energy levels of the isolated crystal and the band width becomes $4J_0$.

2.1.4 Major photoexcitation in polymeric semiconductor

As discussed before understanding of the intimate relationship between morphology and photo-carrier generation mechanisms is the core of this study. Understanding the elementary excitations and dynamics in polymeric semiconductors is therefore essential to advancements in organic photovoltaic. Polymeric semiconductors are highly disordered, incorporating crystalline and amorphous regions. To improve the photo-carrier generation mechanisms, it is necessary to consider exciton motion along and between the

polymer chains and also the complex boundaries established by the multiple numbers of phases (discussed in chapter 2.3.3). Hence, understanding of primary photoexcitation in polymeric semiconductor is significant.

Singlet and triplet excitons: Photoexcitation of an electron to a higher energy level - using above-gap photon energy - in polymeric semiconductors results in the formation of an exciton. The binding of an electron and hole means there are four possible orientations of their spins states. Excitons are classified as singlet and triplet excitons in terms of their spin and optical activity. Of the four possible spin orientations, only one is anti-symmetric with total spin 0 and this is the singlet state. The three remaining orientations all have spin 1 and are called triplet states. Singlet excitons are initial photoexcitation in polymeric semiconductors. Absorption of a single photon promotes the electron from lower energy level to a higher energy level and creates exciton in a spin-less singlet alignment.

Polarons: In the language of chemistry, once the excited electron resides in π^* energy level, the bonds in the benzene rings rearrange to adopt to the new configuration, which changes the molecular geometry. In fact lattice distortion is mainly due to the electron-electron correlation or electron-phonon interaction that exist in polymeric semiconductor, known as low-dielectric constant materials. According to tight binding Hamiltonian, polarons support two energy levels in the middle of the band gap, as shown in Fig. 2.4. Tight binding approximation by only taking the nearest-neighbours

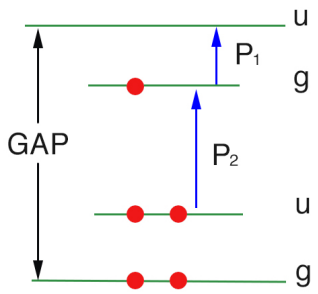

Figure 2.4 – Scheme of the energy levels of polarons, the allowed transition illustrated through blue arrows, g (u) indicate even (odd) parity of the levels, P1 and P2 characterises the low energy and high energy polarons respectively.

interactions straightforwardly explains the electronic properties of conjugated polymer systems. The π-electron wave function can be written as the Bloch wave function, when

considering the polymer as a periodic system [8]

$$\psi_n(x) = \sum_n \exp(ikna)\,\varphi(x-na), \tag{2.8}$$

where a is the lattice constant and is $\varphi(x-na)$ carbon $2p_z$ orbital wave function on the n-th atomic site. The detail calculation can be found in reference [9] as final result as the solution to the Schrödinger equation, at the boundaries is given by

$$E(\pi/2a) = \varepsilon \pm \sqrt{t_1^2 + t_2^2 - 2t_1t_2} = \varepsilon \pm |t_1 - t_2|, \tag{2.9}$$

where $\varepsilon = \langle\varphi_i|H|\varphi_i\rangle$ (we can set $\varepsilon = 0$) and $t_{i,i\pm1} = \langle\varphi_i|H|\varphi_{i\pm1}\rangle$ with the energy gap $E_g = 2|t_1 - t_2| = 2\Delta$. In polyacetylene the dislocated atoms (due to any perturbation like electron-phonon coupling) form the alternating single (longer) and double (shorter) bonds, and lower the symmetry of the system; this process is called dimerisation. Hence, some atoms become closer leading to stronger hopping which creates the gap. As such t_1 and t_2 are the transfer integrals for single and double bond nearest neighbour in polyacetylene. A model introduced by Su, Schrieffer, and Heeger (the SSH model), supports the role of electron-phonon interaction to the Hamiltonian to describe the interactions and primary excitations in polymeric semiconductors, according to this model the polaron has two bound states with a pair of states having energies as

$$E_p = \pm\frac{\Delta}{\sqrt{2}}, \tag{2.10}$$

split off from the continuum and symmetric with respect to the gap center . These two states can be considered as the bonding and antibonding combinations of the two midgap states. As such the lower state is split off from the top of the valence band and the upper state is split off from the bottom of the conduction band, the detail calculation can be found in reference [10]. Fig. 2.4 shows the energy level of the polarons along with allowed transition. Formation of polarons creates two absorption band in the absorption spectrum observed in in mid IR (~ 0.35 eV) and in near IR (~ 1.4 eV). [11] If the conjugated length is large compared to lattice distortion, for example in PPV polymer the

levels are reported to be ~ 0.15 to ~ 0.2 eV. [12]

2.2 Excitonic behaviour in aggregated polymers

2.2.1 Microstructure dependence of excitons

Coherence of excitons inside a molecule or chromophore depends strongly on the microstructure of the polymeric semiconductors. Materials incorporated in optoelectronic devices possess more complex morphologies than simple isolated molecules studied in section 2.1.3. As explained in the Frenkel exciton model, exciton coupling shifts the eigenstates energies of the isolated crystal as well as the oscillator strength redistributions compared to the non-interacting molecules. The origin of the shift is associated with the sign of the Coulombic coupling connecting the two molecules (the excitonic coupling) that was first recognised by Kasha et al.. [13, 14] In a simple dimer consisting of two rigid chromophores, the sign of the coupling is mainly due to the relative orientation of the two chromophores that stems from two types of morphologies. Due to the Coulomb interaction between the chromophores, the excitonic coupling, V_{12}, could be approximated as a point dipole- dipole interaction given by:

$$V_{12} = \frac{1}{4\pi\varepsilon_0} \frac{\vec{\mu}_1.\vec{\mu}_2 - 3\left(\vec{\mu}_1.\vec{r}\right)\left(\vec{\mu}_2.\vec{r}\right)}{R^3}, \tag{2.11}$$

μ_i is the transition dipole moment of the ith chromophore, R and r the distance between the two chromophores and the connecting unit vector respectively. Fig. 2.5 shows two different orientations for two chromophores with given $\mu_1 = \mu_2$. A "side-by-side" configuration [1] of the molecules, classified as a H-aggregate, contributes to a positive coupling whereas a "head-to-tail" configuration [2], classified as a H-aggregate, contributes to a negative coupling. Fig. 2.6 shows the energy level ordering for an H- and J-aggregate dimer. A dimer consists of two-level chromophores, each of them supports a single ground state (g), and a single excited state (e). In the absence of the coupling $V_{12} = 0$ or

1. where $\theta = 90$, $\mu_1 = \mu_2$ that results in $V_{12} = \frac{1}{4\pi\varepsilon_0}\frac{\mu^2}{R^3} > 0$.
2. where $\theta = 0$, $\mu_1 = \mu_2$ that results in $V_{12} = \frac{1}{4\pi\varepsilon_0}\frac{-2\mu^2}{R^3} < 0$.

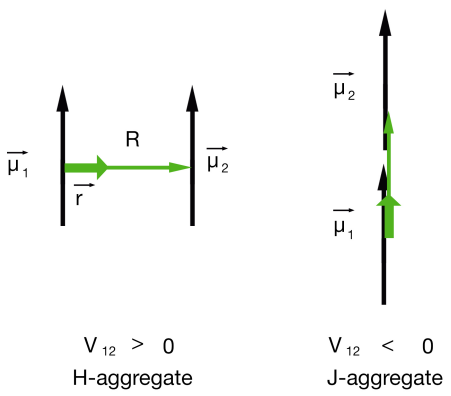

Figure 2.5 – Scheme of transition dipole moment orientations for H- and J-aggregates consisting of two chromophores (a dimer). According to the point dipole-dipole approximation, the side-by-side orientation (left) makes the coupling positive, contributing to the formation of an H-aggregate. The head to tail orientation (right) makes the coupling negative, which contributes to the formation of a J-aggregate.

$J_0 = 0$ the eigenstates corresponding to a single molecular excitation are localised and denoted as $|1\rangle \equiv |e_1 g_2\rangle$ and $|2\rangle \equiv |g_1 e_2\rangle$. In the presence of coupling the symmetric ($+$ state) and anti-symmetric ($-$ state) eigenstates are given by

$$|\psi_{\pm}\rangle = \frac{1}{\sqrt{2}} \{|1\rangle \pm |2\rangle\}. \tag{2.12}$$

In an H-aggregate when $J_0 > 0$ the higher energy state is symmetric and the lower energy state is anti-symmetric whereas it is opposite in a J-aggregate when $J_0 < 0$. The symmetric and anti-symmetric eigenstates result from the behaviour of the state under a symmetry operator (*i.e.* reflection through a plane bisecting the dimer pair) therefore the $k = 0$ state resides at the top of the band in an H-aggregate and at the bottom of the band in a J-aggregate. Note that because the oscillator strength exists in the transition from the ground state $|g_1 g_2\rangle$ to the symmetric state, the absorption spectrum is therefore blue-shifted in the H-aggregate and red-shifted in the J-aggregate relative to the single molecule, as shown in the Fig. 2.6. However, the red or blue shifts in the oscillator strength cannot be the only characteristic of J- or H-aggregation. Spano et al. address the additional spectral signatures caused by influence of vibronic coupling [15], shall be discussed later in this chapter. In short, in an H-aggregate polymer the interchain interaction (through space) is dominant whilst in a J-aggregate polymer the intrachain interaction (through bond) is dominant . Different microstructures contribute to different

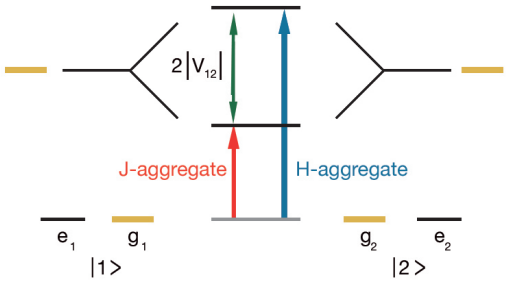

Figure 2.6 – Scheme of energy levels of two chemically identical two-level molecules. When the molecules are isolated (on the left and right sides). Electronic interactions result in an exciton-coupled state, shown in the center. When the (+) state is the top state, it becomes an H-aggregate. When the (+) state is the bottom state, it becomes a J-aggregate. For the H-aggregate, the optical allowed state is higher in energy, making it blue-shifted with respect to the monomer. On the other hand, the J-aggregate has its optically allowed transition at lower energy, making it red-shifted relative to the monomer. Figure adapted from reference [16].

excitonic behaviours.

2.2.2 Franck-Condon principle

Electron-phonon coupling in a conjugated polymer leads to the alteration of the polymer backbone or rotation of repeat units about the axis defined by the backbone. This coupling contributes to a planarisation of the polymer backbone and stiffening of the chemical bonds (Fig. 2.7 shows simulated ground and excited state geometry). [17, 18] An excited molecule forms a new potential compared to its ground state potential, hence the geometry of the excited state and ground state potentials is not the same and there is a non-zero overlap between ground and excited state. Given that the time required for the molecule to adopt to its new equilibrium configuration is long compared to the time required for electronic transition (1 ps compared to 1 fs), therefore any electronic transitions can be considered to occur instantaneously in comparison to the structural rearrangements. Hence the response of nuclei to the change of electronic structure occurs on much longer timescales compared to the electronic transition such that molecule does

not have time to move within the nuclear potentials during the short time of the optical excitation; this is assigned to the Franck-Condon principle. [17, 19, 20]

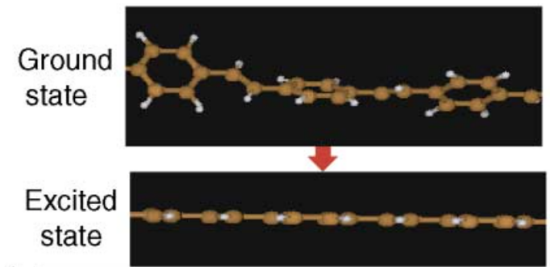

Figure 2.7 – Simulated ground and excited state geometries of poly(p-phenylene-vinylene) oligomers. The evidences of planarization of the chemical bonds is shown in the excited state. Figure adapted from Reference [17].

Fig. 2.8 shows the nuclear potential that is assumed to be harmonic *i.e.* $V_R = 1/2k_f R_0^2$ where k_f is the force constant. The lower potential is the electronic ground state and the upper is electronic excited state displaced by R_0. The vibrational frequency $\omega_0 \sim 1400\,\mathrm{cm}^{-1}$ corresponds to the vinyl stretching mode. Therefore, $\hbar\omega_{0-0}$ is molecular excitation energy. The absorption transitions are shown with blue arrows and the emission transitions are shown with green arrows. An electronically excited molecule quickly reorganises its geometry to establish its minimum energy. The released energy is known as relaxation energy: $V_R = 1/2k_f R_0^2$ ($\sim 0.1 - 0.2\,\mathrm{eV}$ in π-conjugated polymers [5]). Therefore it emits from lower energy state that cause a Stokes shift between the absorption and emission spectra.

Franck-Condon principle permits to separate the wave functions describing the initial (ψ_i) and final states (ψ_f) into electronic and vibronic wave functions such that

$$\psi_i = \psi_{elec,i}\psi_{vibr,i} \qquad \psi_f = \psi_{elec,f}\psi_{vibr,f} \tag{2.13}$$

where $\psi_{elec,i}$ and $\psi_{elec,f}$ describes only the electron motion whereas $\psi_{vibr,i}$ $\psi_{vibr,f}$ describes just the nuclei vibrational motion. Given that the absorption rate (the transition rate) is $\propto \left|\left\langle \psi_f \left| eX \right| \psi_i \right\rangle\right|^2$, where e$X$ is the electric dipole moment (interaction Hamiltonian), within the Franck-Condon approximation, it is possible to write

$$\left\langle \psi_f \left| eX \right| \psi_i \right\rangle \rightarrow \left\langle \psi_{elec,i} \left| eX \right| \psi_{elec,f} \right\rangle \int \Psi^*_{vibr,i}(X)\,\Psi_{vibr,f}(X)\,dX, \tag{2.14}$$

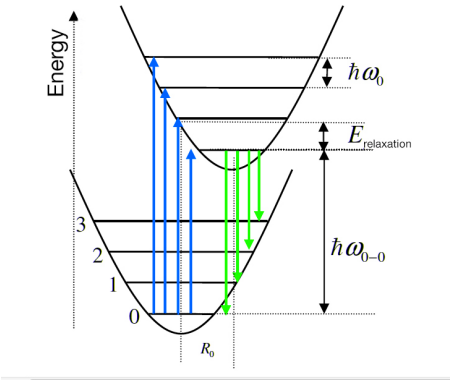

Figure 2.8 – Nuclear potential that is assumed to be harmonic *i.e.* $V_R = 1/2k_f R^2$ where k_f is the force constant. The lower potential is the electronic ground state and the upper is electronic excited state displaced by R_0. The vibrational frequency $\omega_0 \sim 1400\,\mathrm{cm}^{-1}$ corresponds to the vinyl stretching mode. $\hbar\omega_{0-0}$ is molecular excitation energy. The absorption transitions are shown with blue arrows and the emission transitions are shown with green arrows.

where $\langle\, \psi_{elec,i}|eX|\,\psi_{elec,f}\rangle$ is the matrix element between two electronic states *i.e.* $\psi_{elec,i}, \psi_{elec,f}$. $\psi_{vibr,i}, \psi_{vibr,f}$ are vibrational wave functions of the lattice. $\int \psi^*_{vibr,i}(X)\,\psi_{vibr,f}(X)\,dX \equiv \left|\langle \psi_{vib,i}|\psi_{vib,f}\rangle\right|$ is the overlap integral assuming that the electronic dipole moment is independent of the vibrational modes. Following the fast reorganisation, whilst the vibrational level $v = 0$ in the excited state remains occupied, the Franck-Condon factor (that supports the strength of electro-phonon coupling) for a transition from $v = 0$ to $v \neq 0$ is given by [5]

$$\left|\langle \psi_{vib,0}|\psi_{vib,v}\rangle\right|^2 = \frac{\exp\left(-\lambda^2\right)\lambda^{2v}}{v!}, \tag{2.15}$$

where λ^2 is Huang-Rhys factor given by $\lambda^2 = \frac{k_f R^2}{2\hbar\omega_0}$ where v is the number of quanta involved in transition or number of quanta that shifts the excited state potential.

2.2.3 Polaronic excitons

In 2005, Spano studied the photophysics of aggregated polymers theoretically and introduced a model *i.e.* weakly coupled H-aggregate model that takes into account ex-

citonic intermolecular coupling, exciton-phonon coupling and disorder, within a generalised Holstein Hamiltonian. [21] The absorption and photoluminescence spectra of polymeric semiconductor with π-conjugation supports the idea of strong vibronic progressions involving mainly the symmetric vinyl stretching mode with an energy of about $1400\,\mathrm{cm}^{-1}$. Furthermore, in the excited state the vibrational coordinate is slightly elongated along one or more symmetric vibrational coordinates, the coupling between the electronic and nuclear degrees of freedom is local. Combination of electronic and vibrational degrees of freedom for the excited state favours the concept of polaronic excitons for Frenkel excitons in polymeric semiconductors. In 2012, Yamagata and Spano introduced a new model for analysing the absorption and photoluminescence of aggregated polymers *i.e.* "HJ" hybrid model. In the "HJ" hybrid model the authors considered the competition between intrachain (through-bond) coupling, and interchain (through-space) coupling and incorporated local exciton-vibrational coupling into the exciton Hamiltonian by including intra- and intermolecular exciton coupling, electron vibrational coupling and energetic disorder. The authors used a Holstein model Hamiltonian to investigate exciton-phonon coupling in H- and J-aggregates. [15] Excited state comprised of electronic and vibrational degrees of freedom can be viewed as polaronic excitons, where the electron/hole is surrounded by a vibrational distortion field or phonon cloud [22]. In order to account for exciton-vibrational coupling it is assumed that the nuclear potential relative to the ground state S_0 is shifted with respect to the nuclear potential relative to the excited state S_1; the shift is quantified by Huang-Rhys factor. The Holestein Hamiltonian to treat vibronic coupling is given by

$$\begin{aligned} H = \omega_0 \sum_n b_n^\dagger b_n + \omega_0 \lambda \sum_n |n\rangle \langle n| \left(b_n + b_n^\dagger \right) + \sum_n J_0 \left\{ |n\rangle \langle n+1| + |n\rangle \langle n-1| \right\} \\ + \omega_0 \lambda^2 + \omega_{0-0} + D, \end{aligned} \tag{2.16}$$

where $\hbar = 1$, the first term is the vibrational energy, b_n and $b_n^\dagger$ are responsible for creation and annihilation of vibrational excitations on the nth molecule. ω_0 is the vibrational frequency of the high frequency vinyl-stretching mode with a value of $\sim 0.174\,\mathrm{eV}$ ($1400\,\mathrm{cm}^{-1}$). The second term is vibronic coupling and the third term is the excitonic

coupling. J_0 is the nearest neighbour excitonic coupling. $\omega_0\lambda^2$ is the relaxation energy. The last term $\omega_{0-0}+D$ is the molecular excitation transition frequency and the gas-to-crystal shift sourced by non-resonant interactions set to zero. This Hamiltonian, based on multi-particle basis set is developed by Philpott for Frenkel polarons. [23] Within a single-particle basis picture ($|n,\tilde{\nu}\rangle$) there is an electronically excited molecule at nth site with ν vibronic quanta in the excited-state nuclear well (see Fig. 2.9 bottom), whilst all the other molecules are in the electronically and vibrationally ground state. A two-particle state, ($|n,\tilde{\nu};n+s,\nu\rangle$) (see Fig. 2.9 top), has one electronical excited molecule at the nth site with ν vibronic quanta in the excited well, and one vibrational exited molecule at the $(n+s)$th site. All the other molecules remain unexcited in the ground state and s measures the displacement between the vibronic and vibrational excitations. The eigenfunction correspond to the Hamiltonian is given by

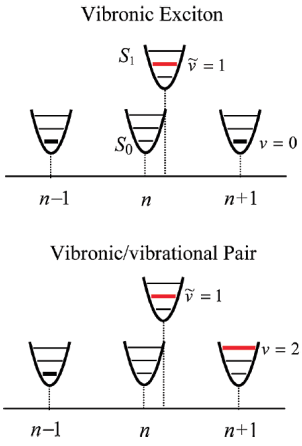

Figure 2.9 – Examples of the fundamental excitations in ordered organic assemblies. The vibronic (single-particle) excitation shown is $|n,\tilde{\nu}=1\rangle$, while the vibronic/vibrational pair (two-particle state) is $|n,\tilde{\nu}=1;+1,\nu=2\rangle$, figure adopted from reference [22].

$$|\psi_\alpha\rangle = \sum_{n,\tilde{\nu}} c^{\alpha}_{n,\tilde{\nu},s,\nu}\,|n,\tilde{\nu};n+s,\nu\rangle\,, \tag{2.17}$$

where the $\alpha = 1,2,...$ indicates eigenstates in increasing order of energy and ($\alpha = 1$) indicates the lowest energy excitonic polaron or exciton. The off-diagonal elements of Hamiltonian are represented by the usual excitonic Hamiltonian

$$H_{ex} = \sum_{m,n} J_{mn}\,|m\rangle\,\langle n|\,, \tag{2.18}$$

where $|m\rangle$ represents a pure S_1 electronic excitation at site n and J_{mn} is the excitonic coupling between the mth and nth molecules. The off-diagonal matrix elements of Hamiltonian connecting one-particle states allow for resonant energy transfer in the conventional Frenkel exciton theory. In the weak coupling regime where $W \tilde{<} \omega_0 \lambda^2$ the exciton band (W) can be viewed as a series of vibronic sub-bands, each identified with the number of quanta v which characterises the one-particle states with the greatest admixture, and with a bandwidth of approximately, $W = e^{-\lambda^2} \lambda^{2\tilde{v}} / \tilde{v}!$. The sum of the sub-band widths is equal to W (Franck-Condon factor of unity). The optical response from the excitons in equation 2.17 derives from the following basic properties: (i) Only one-particle states are optically allowed, these states contribute to the $0-0$ emission from the vibrationless ground state. (ii) Both one- and two-particle states radiatively couple to the electronic ground state with one or more vibrational excitations. Thus, sideband emission involves both one- and two-particle states. (iii) In the absence of disorder only nodeless excitons $k = 0$ can be optically excited from the vibrationless ground state where $v = 0$ consistent with transition selection rule $\Delta K = 0$. [22]

In disorder free aggregates such states are delocalised over the entire π-stacks whereas disorder causes the excitation to be localised. [24] This formalism is required to describe the spatial extent of the vibrational excitons' wave function and a key concept for describing the relationship between optical properties and microstructure of polymeric semiconductors.

2.2.3.1 The "HJ" hybrid model

As discussed in section 2.2.1 different arrangements of chromophores dipole moments contribute to different microstructures in terms of H- and J-aggregation behaviour. Any change in microstructure contributes to different photophysics. The photoluminescence spectrum is more sensitive, with H or J behaviour than the absorption spectrum, hence the absorption spectral line shape can still be well-analysed by the conventional H-aggregate model (by Spano). In fact photoluminescence is more sensitive with the interplay between the intra- inter-chain interactions. Long range intrachain order (or weaker interchain interactions) induces J-aggregate behaviour, whilst short range intra-

chain order (or stronger interchain coupling) induces H-aggregate behaviour. The "HJ" hybrid model enables us to interpret the steady-state absorption and photoluminescence spectra of aggregated polymers and their blends and to relate those signatures to the microstructure. The "HJ" hibryd model describes photophysics of π-conjugated aggregates, such as molecular crystals and polymer thin films. In polymer π-stacks Coulombic interaction between the chains competes with through-bond interactions within the chain that contributes to hybrid HJ-aggregate photophysics. The inter- intrachain interaction occurs between different chromophores in the π-stacks. With "HJ" hybrid model Yamagata and Spano address the additional spectral signatures (an analysis with line strength ratio of the absorption and photoluminescence (PL) spectra) caused by influence of vibronic coupling to distinguish H- vs. J-aggregation. [15] The details of optical properties of aggregated polymers shall be discussed later in chapter 5.5.2.

2.2.3.2 Short-range charge transfer and long-range Coulombic couplings

In 2014, Yamagata et al. has developed the discussion of hybrid coupling by using a Holstein-style Hamiltonian including both Frenkel and charge-transfer (CT) excitons. In the recent discussion the hybrid HJ coupling consists of the long-range interactions, characterised by Frenkel exciton dipole coupling, and short-range interactions, characterised by charge-transfer (CT) interactions. Charge transfer interactions, like dipole-dipole coupling can be classified as either J-type (negative coupling constant) or H-type (positive coupling), see Fig. 2.10. [25, 26]

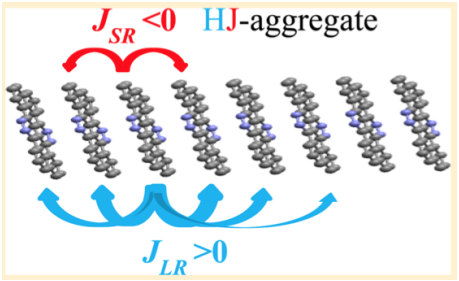

Figure 2.10 – Scheme of long range dipole-dipole coupling (in blue) and short range charge transfer coupling (in red) in polymer π-stacks. Figure adapted from reference [26].

Yamagata et al. considered short-range coupling induced by HOMO/HOMO (and LUMO/LUMO) wavefunction overlap between neighbouring chromophores. [27] Vi-

bronic signatures identical to those caused by Coulombic coupling has been identified. In this classification the J- or H-type aggregate occurs depending on the relative sign between the electron (t_e) and hole transfer integrals which connect adjacent LUMO (HOMO) orbitals. The sign and magnitude of t_e and t_h are sensitive to changes in the intermolecular orientation *i.e.* slip-stacking and sub-Angstrom displacements of neighbouring. The short-range charge transfer coupling is given by

$$J_{CT} = -\frac{2t_e t_h}{E_{CT} - E_F}, \tag{2.19}$$

where E_{CT} and E_F represent the energies of charge transfer state and Frenkel state. The H- J-aggregates photophysical behaviours are identified by $J_{CT} > 0$ and $J_{CT} < 0$ respectively. Therefore, the interference between short and long-range coupling in organic materials can be classified as either H-H, H-J, J-H, or J-J where the first label refers to the sign of the dipole-dipole interaction, and the second refers to the charge transfer coupling.

Moreover, recently (2015) Hestand et al. considered the interference between the two couplings when defining H and J-aggregates based on short- and long-range couplings. The coupling results in "null-aggregates" when both the Coulomb coupling and charge transfer coupling are strong but interfere destructively which spectroscopically resembles uncoupled molecules. [25] Hestand et al. developed the discussion by using Frenkel/charge transfer Holstein Hamiltonian that takes into account both sources of electronic coupling as well as intramolecular vibrations. For integrated Frenkel/charge transfer systems vibronic spectral signatures are manifested by perturbative and resonance regimes. In the perturbative regime, the sign of the lowest exciton band curvature, is related the ratio of the first two vibronic peak intensities and defines J- and H-aggregation. The vibronic ratio also remains useful to evaluate the J or H nature of the system in the resonance regime.

2.2.4 Converting H and J by processing

The solid state microstructure of conjugated polymeric semiconductors can be extremely sensitive to processing conditions. Controlling structure-property relationships of melt- or solution-processed conjugated polymers have strong impact on the intrachain (chain conformation) and interchain (packing) order. An aggregated polymer characterises excitation that supports delocalised π-electrons in both ground and excited states, over several chromophores located on adjacent polymer chains. Providing polymers of different molecular weights, as well as degrees of polydispersity, regioregularity and chemical purity can further affect the structure/property relationship. It has been demonstrated that molecular weight -average length of polymer chains- plays a significant role in controlling the solid-state crystalline packing and microstructure as well as optoelectronic properties of polymers. [28] Moreover, given that the interchain bonding in polymers is relatively weak, fabrication and processing protocols becomes very crucial in determining microstructure and optoelectronic properties. Solid-state parameters including crystallinity and macromolecular orientation is strongly dependent on the fabrication protocols. Macromolecular orientation or crystallinity is caused by inter-chain order while a distinct ordered chain conformation is caused by intra-chain order. Note that the formation of intra-chain-ordered chain segments contributes to supramolecular aggregation/crystallisation. [28]

In a polymer π-stack the photophysical properties is mainly dependent on the competition between intrachain electronic coupling, which favours J-like behaviour, and interchain coupling, which favours H-like behaviour. Processing conditions, mentioned above, can manipulate this interplay between the H- J-aggregations such that either J- or H-aggregation is dominant. Therefore, polymer π-stack is termed as an HJ-aggregate. [29]

Clark et al. showed that spin-cast films of P3HT with low boiling point solvents, such as chloroform, show larger exciton band width (*i.e.* W extracted from the absorption spectra), indicating a shorter conjugation lengths and lower crystalline quality. However spin-cast films of P3HT with high boiling point solvents show lower W with correspond-

ingly longer conjugation lengths and higher crystalline quality. Furthermore, spin-cast films with low boiling point solvents have a lower proportion of crystalline aggregated regions compared to those with high boiling point solvents. They further studied the morphology of the films using atomic force microscopy (AFM) in order to verify that changes in microstructure contribute to different absorption spectrum. It was found that the films spun from high boiling point solvents show rough surfaces while those spun from low boiling point solvents are smoother. The roughness was associated with the formation of microstructures. [30]

Furthermore, Spano et al. showed that spin-cast films of P3HT (with chloroform as the solvent) behave like H-aggregates. This was attributed to the low-boiling-point of the solvent which contributes to a high level of disorder in the film and short conjugation lengths aggregates. [24]

Niles et al. showed that nanofibers of P3HT formed by slowly cooling in toluene behave like J-aggregates. There observation was explained in terms of increased intrachain order that contributes to larger conjugation lengths and stronger intrachain interactions compared to interchain interactions. Dominant $0-0$ intensity of PL and absorption characterises J-aggregate behaviour. [31]

Baghgar et al. showed that cross-linking in P3HT copolymers can be used to control the interchain interactions. Those authors controlled the size of the cross-linking agent relative to alkyl side chain length in nanofibers of P3HT. It was demonstrates that by applying a large linker or using a linker of comparable length to the lamellar spacing, the exciton coupling in nanofibersof P3HT can be controlled, by reducing inter-chain coupling. The great advantage of this cross-linking process used to control the interchain interaction is that cross-linking process removes the need for all structures to be kinetically stable at every step during device fabrication. [32]

Baghgar et al. showed a molecular-weight dependent exciton coupling in isolated P3HT nanofibers. The authors found that intra- and interchain coupling (quasi-two dimensional) reduced to an exclusively intrachain coupling (quasi-one dimensional) as P3HT molecular weight is increased *i.e.* H- to J-type coupling significantly due to the increased planarization of P3HT backbones. [33]

Paquin et al. identified a clear microstructure-dependent interplay of intermolecular and intramolecular exciton spatial coherence in neat regioregular P3HT through a range of molecular weight (12.4-264 kg/mol). It was found that in thin-film structures of high-molecular-weight materials ($M_w > 50$ kg/mol), a balance of intramolecular and intermolecular excitonic coupling results in high exciton coherence lengths along chains (~ 4.5 thiophene units), with interchain coherence limited to ~ 2 chains. However, for thin-film structures of low-Mw P3HT (($M_w < 50$ kg/mol), the interchain exciton coherence becomes dominant. ($\sim 30\%$ higher than in architectures formed by high-molecular-weight materials). [34]

Hellmann, et al. showed that it is possible to tune the $0-0$ absorption transition of (P3HT) in blends with poly(ethylene oxide) (PEO) through the control of the liquid-liquid phase separation process during solution deposition. A significant liquid-liquid phase separation in solution (*i.e.* highly pure domains of P3HT and PEO) was characterised to give a pronounced J-like aggregation behaviour (with a low exciton band width). The authors attributed this optical response of the binaries to conformational changes of the P3HT backbones that occur in the presence of PEO, contributing to an increased delocalisation of the π-electron density along a more planarized backbone, as well as a larger chromophore with larger conjugation length. [35]

Therefore, it appears possible to shift and tune between J- and H-dominated behaviours in polymeric semiconductors by controlling microstructure, like in P3HT as a model system.

It is important to note that knowledge acquired in this section has been expanded to the HJ aggregated model and Frank-Condon model to analyse and interpret the results in chapter 5 and partly in chapter 4 (absorption spectra).

2.3 Heterostructures

As mentioned before in this chapter, the motivation of this work is to gain a fundamental understanding of the elementary excitations and dynamics in polymer photovoltaic cells in order to design, optimise and tune the devices based on conjugated

polymers at molecular level. This chapter has revised the excitonic behaviour in the polymeric semiconductors and how it is related to the morphology. The following section focuses on the excitonic behaviour of bulk heterostructures of polymeric semiconductors.

2.3.1 General context

Photovoltaic cell is recognised as a promissing candidate to harvest energy from the sun. The photovoltaic effect *i.e.* generation of voltage when a device is exposed to light, was first discovered by Becquerel in 1839. [36] The key objective of all photovoltaic cell technologies is to increase conversion efficiency and reduce production costs.

As a general concept for generating electricity we first refer to a pn-junction. A doped semiconductor with a higher electron conductivity is termed n-type whilst a material with a higher hole conductivity is termed p-type. Combination of a p-type and n-type favours the concept of pn-junction such that electrons from the n-type semiconductor flow into the p-type region and recombine with holes flowing into the n-type region. Following the absorption of a photon, separation of charges occurs near the interface, which forms a space charge region. Due to the fact that semiconductor band gap covers the entire solar spectrum ($\sim 0.5 - 4\,\mathrm{eV}$) semiconductors are ideal for the task of generating electricity. Furthermore the conduction properties of the semiconductor can be controlled by the amount of dopant atoms that are added. It is also possible to generate electricity from the polymeric semiconductors because of their delocalised π-bonds as well as their typically large band gap. Therefore, a photovoltaic effect is required to extract the charge carriers generated by incident light. This is achieved by incorporating the polymeric semiconductors between two conducting electrodes. For a device to produce a current, one electrode must collect more electrons and the other more holes, commonly referred to as asymmetric collection. In conventional inorganic photovoltaic cells this asymmetry is provided by fabricating the semiconducting layer such that it acts as a diode; in silicon devices this is done by doping the two sides of the semiconductor differently such that a p-n junction is created. Analogous to effect of dopant in inorganic semiconductors it is possible to manipulate the optical and electronic properties

of polymeric semiconductors through a tailored morphology. This is crucial for device application, including photovoltaic cells and LEDs. In what follows, we briefly discuss different structures of photovoltaic cells.

2.3.1.1 Single layer OPV cell

The simplest configuration of an organic photovoltaic cell incorporates a single layer polymeric semiconductor between two metals with different work functions. As such light is illuminated through a transparent electrode, onto the active layer (polymer) and contributes to creating excitons and charges through the electrodes. Taking advantage of the fact that absorption coefficient in polymeric semiconductors is high, the film thickness can be very thin ($\sim 100\,\text{nm}$). These early devices were commonly in a metal-semiconductor-metal configuration where the driving force for the current generation was provided by the difference in work function between the two metal electrodes. In a single organic semiconductor layer the photons mainly generate excitons and only a tiny proportion (if any at all) separate to form free carriers, due to the increased Coulombic binding between electrons and holes. Thus these devices suffered from extremely low photocurrents and the semiconductors used exhibited low charge mobilities and thus lossy transport. To improve the exciton dissociation a new structure was introduced. Note that the the power conversion efficiency of a single layer photovoltaic cell is $<< 1\%$. [37]

2.3.1.2 Bilayer heterostructure OPV cell

The fabrication of the first OPV devices in a bilayer heterostructure, where two different organic semiconductors were sandwiched together was reported by Tang et al. with copper phthalocyanine: perylene derivative (CuPc:PV) photovoltaic cells. This step forward in device structure saw huge increases in device power conversion efficiencies, mainly by increasing the current generation resulting from an increase in bound electron-hole state separation. The bilayer structure increased the efficiency by creating band offsets that are larger than the exciton binding energy; enabling the dissociation

of the excitons. A bilayer consists of an electron donor (D) semiconductor (an electron provider) and an electron accepting semiconductor known as the acceptor (A). A standard bilayer is polymer:fullerenes in which donor is the main light absorber. Upon absorbing a photon an exciton is created in polymer and migrates towards the interface. The excitons can dissociate more easily compared to the excitons in single layer. When an exciton reaches the interface of heterostructure it is energetically favourable for the electron component to transfer to the lower LUMO level of the other material and if the difference between the conduction band energies is high enough then the bound state will be separated into free charges. The discovery that a difference in energy between materials was enough to separate the bound electron-hole state revolutionised the field of OPV and allowed all further developments to occur. However, the power conversion efficiency is limited by the small area of charge-generating interface between donor and acceptor. Given the small exciton diffusion length (about few nanometer) in polymeric semiconductors only few excitons reach the interface and can be dissociated and excitons created far from the interface recombine without the chance to reach the interface. [38]

2.3.1.3 Bulk heterostructure OPV cell

Whilst bilayer heterostructures provided a huge increase in current output from photovoltaic devices, they were still limited. As exciton transport in the disordered materials is slow relative to the recombination of the bound electron-hole state, excitons have a limited diffusion length which they can travel before being lost to recombination. In organic semiconductors the exciton diffusion length, L_{EX}, is of the order of 10 nm. Thus if an exciton is not generated within L_{EX} of a heterostructure interface it will likely not be separated to form free charges. As such the small interface in bilyares has been a major limiting factor in power conversion efficiency. To overcome this the concept of a bulk heterostructure was introduced by the pioneering work of Yu et al. [39] and Halls. In heterostructure, the donor (polymer) and acceptor (typically fullerenes, PCBM) are blended together such that an interpenetrating network area is achieved through controlling the phase separation between two components, when casting thin films from solution. The first cell incorporating the blended active layer was reported by Hiramoto et al.

in 1991. [40] Such a bulk heterostructure overcomes the limitations of the bilayer by providing an enhanced donor/acceptor interface area through the entire device consequently increasing the active volume within which excitons can be generated and successfully separated. If the domains of donor and acceptor material are on the length scale of the exciton diffusion length then it is possible to separate a high proportion of the excitons. The concept of bulk heterostructure is supported by observation of ultra-fast photo-induced charge separation 45 fs. [41], as well as the fact that some bulk heterostructure OPV cells with the ratio of incident photons to charge extracted as current, approaching 100%. This has been reflected in power conversion efficiency of 10% when using polymer: fullerenes bulk heterostructures with optimised microstructure. [42]

2.3.2 Organic vs. hybrid

The bulk heterostructure architecture in which the polymer and fullerenes are intimately mixed throughout the active laver, has shown promising results. Most importantly the organic photovoltaic cells can be made using solution phase techniques and the high absorption coefficient of polymeric semiconductors allows the use of very thin films. However, poor electron mobilities, high exciton binding energies (due to the low dielectric constant of polymeric semiconductors ~ 3 compared to inorganic materials ~ 10 [43]), small exciton-difiusion length with respect to the thickness of the active layer [44] all limit the efficiency of organic photovoltaic cells. Moreover, given that fullerenes, as the typical acceptor in organic photovoltaic cells, have a low extinction coefficient compared to the majority of polymeric semiconductors, contributes to incomplete absorption over the full range of the solar spectrum.

The field of optoelectronic owes a big part of its success and development to discovery of quantum confined nanomaterials (QCNs). It is therefore possible to employ the quantum confined nanomaterials as an alternative to fullerenes in organic photovoltaic cells that contributes to a new concept of hybrid organic-inorganic cells. Hybrid organic-inorganic is a photovoltaic device where the primary interface for charge generation is at the junction between a polymeric semiconductor and an inorganic material with electronic structure optimised for photovoltaic diode operation. A wide range of

inorganic materials have absorption profiles that cover a broad range of the spectrum and have high extinction coefficients such that complement the absorption of the semiconducting polymer. Quantum confinement effects, allow the band gap of any inorganic material to be tuned, by changing the crystal size. This tuning can modify the energy levels at the interface of the polymer/inorganic interface to improve charge separation as well as maximising the absorption. Moreover, the higher dielectric constant of inorganic materials allows for higher charge separation efficiency. The increased crystallinity also improves charge transport. In short, these devices present the opportunity to integrate and combine favourable optoelectronic, chemical and thermal stability properties of inorganic nanocrystals with solution processability and low-temperature chemical synthesis of polymers. [45–47] In spite of their potential, to date such devices display lower power conversion efficiency, especially low photocurrent, compared to fully organic devices. [3, 4] Recombination of bound pairs at the interface is considered to be a significant reason for the low efficiency [43, 48] that is assigned to a lack of control over the solid-state microstructure in semiconductor-nanocrystals/polymer films, and thus presents a challenge in the development of hybrid photovoltaic cells. [49–51] The main difference between the two design is that in hybrid photovoltaic cells the band offset at interface is due to the difference between the conduction band minimum (the valence band) of inorganic material and the HOMO (LUMO) of the organic material. To develop better hybrid photovoltaic cells, it is important to focus on the donor-acceptor interface and the morphology of the active layer. This shall be discussed further in this thesis (chapter 4).

2.3.3 Organic: Crystal vs. phase-separated (one-phase, 3 or 4 phase, 2 phase)

The intermixing of the donor and the acceptor (both dissolved in a common solvent) in polymer: fullerenes blends is the most common way to deposit the active layer through spin-coating or drop-casting. In the meanwhile the solvent evaporates, resulting in an intermixed donor and acceptor whilst remaining interconnected to either side of the device. [39, 52] However, that provides a large donor/acceptor interface compared to the bilayer, the morphology is not perfect. Fig. 2.11 (left) shows the ideal image

for a bulk heterostructure supporting domain sizes not larger than the exciton diffusion length in addition to a perfect connection to the respective electrodes. Practically this ideal morphology is difficult to achieve. Typical processing methods contributes to the morphology shown in fig. 2.11 (right), in addition to reasonable mixing regions there are still large regions containing either polymer or fullerenes that prevent exciton migration through the interface or charge separation towards electrodes. Fig. 2.12 as a

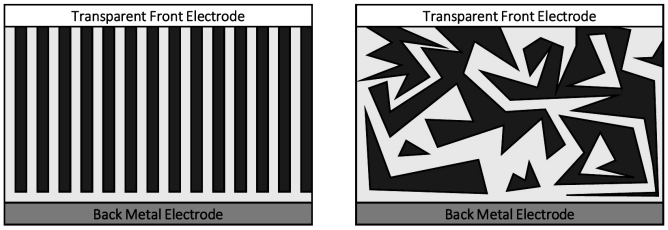

Figure 2.11 – Schematic diagram of an ideal bulk heterostructure (left) and a more random mixture of the donor and acceptor (right).

common image of the bulk heterostructure shows that fullerenes may intercalate between amorphous and crystalline polymer chains that forms an intermixed phase. The microstructure can be associated with different phases: the fully intemixed or intercalated co-crystal phase (one-phase morphology), the pure fullerenes domain and fully intermixed phase (two-phase morphology) or pure fullerenes domain and fully intermixed phase and neat polymer domain (three-phase morphology). [53] While it is hard to achieve the ideal morphology (see Fig. 2.11 left) it is still possible to manipulate morphology (see Fig. 2.11 right), optimise it and change the percolation pathway towards the electrodes as well as time needed for that. This manipulation is possible by using additives, changing the polymer: fullerenes ratio and post-processing techniques such as thermal annealing. [53–55]

Muller et al. investigated the importance of microstructure for charge generation. The authors found that fullerenes aggregates support a high electron affinity compared to the fully intermixed phase; whilst the intermixed phase aids the initial charge separation, the pure phase favours the transport out of the intermixed region by providing a strong driving force to allow charge separation and avoiding geminate recombination. [56]

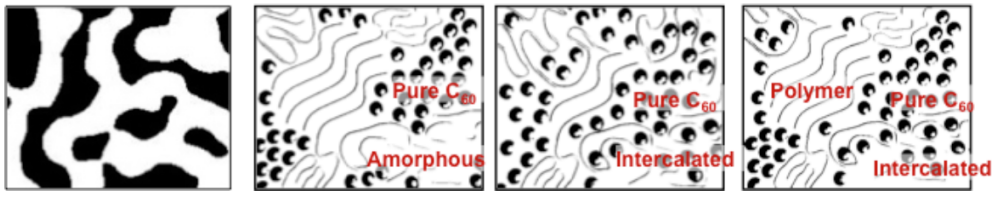

Figure 2.12 – Different phase microstructures in Polymer: fullerenes blends. a) shows a classical picture of a bulk heterostructure b) c) d) show three different morphologies obtain using different polymers, polymer: fullerenes ratio or by optimizing the film processing using additives. Figure adopted from reference [44].

By using (poly(2,5-bis(3-alkyl-thiophene-2-yl)thieno[3,2-b] thiophene) pBTTT polymer that is suitable for microstructure manipulation, Muller et al. found that the 1:1 blend ratio incorporates to only one-phase morphology while 1:4 blend ratio enables neat PCBM and intercalated region to co-exist.

Scarongella et al. manipulated pBTTT: PCBM microstructure during film processing by using fatty acid methyl ester additives of different length (Me7, Me12, Me14) and showed that co-crystal formation can be manipulated from fully intermixed, to a partially intercalated, to a predominantly phase-separated microstructure. [55] The authors concluded that neat PCBM domains are important for free charge generation because in the two-phase morphology (1:4 blend ratio, pBTTT: PCBM intermixed phase and neat PCBM domains) long-lived charges exist; due to the driving energy provided by neat PCBM domains that assist in charge separation. However in the one-phase morphology (1:1 blend ratio, pBTTT: PCBM intermixed phase) the charges recombine in a geminate manner. They further concluded that the use of Me12 in 1:1 blend ratio of pBTTT: PCBM contributes to a two-phase morphology. While with Me7 a three-phase morphology including pBTTT: PCBM intermixed phase and neat PCBM domains and neat polymer domain was achieved. They reported that the total efficiency of the charge separation is reduced. In fact some excitons created in neat polymer recombine before reaching to the interface.

It is important to note that knowledge acquired in this section has been expanded to the interface of P3HT: ZnO hybrid bulk heterostructure in chapter 4.

CHAPTER 3

EXPERIMENTAL TECHNIQUES

In this chapter the experimental techniques that we used to characterise the polymer thin films (chapter 4), solutions and gels (chapter 5), are discussed.

3.1 Steady-state linear absorption

When a polymeric semiconductor absorbs photon through an excitation, a linear process takes place in which electrons become excited from the ground state S_0 to a higher singlet electronic state S_1. In order to measure the absorption of polymeric semiconductors in either thin films or solutions we employ Beer-Lambert law (the intensity of light decreases exponentially with depth in the material) and measure the transmittance; from which we can calculate the absorption while other processes such as reflectance and scattering are negligible. Beer-Lambert equation is given by

$$\ln\left(\frac{I_0}{I}\right) = \sigma n d, \tag{3.1}$$

where I_0 is the intensity of the incident light, I is the intensity of the transmitted light through the sample d is the thickness of the sample and n is density of the species. Transmittance is given by

$$T = \frac{I(\lambda)}{I_0(\lambda)}, \tag{3.2}$$

$$A = -10\log(T). \tag{3.3}$$

The transmission through the sample is measured using standard lock-in techniques. The probe beam was a monochromated 250 W halogen-tungsten lamp modulated at $f_{\text{probe}} = 139$ Hz and monitored with a Si/Pbs dual-band photo-receiver. The sample was held in a closed-cycle, controlled vapour cryostat environment where it could be cooled down to 10K with exchange gas. This was the case for all measurements reported here unless stated otherwise. Fig. 3.1 shows the schematic of the set up; the absorption measurement

were taken through the lamp optical path.

3.2 Steady-state photoluminescence (PL) measurement

Photoluminescence is one of the possible ways to deactivate the excited state through a radiative decay. In this process, the excited state exciton (S_1) relaxes to the ground state (S_0) through the emission of a photon. In this thesis, the PL spectrum of the samples were measured using a standard lock-in technique. Continuous-wave laser modulating at $f_{\text{pump}} = 170\,\text{Hz}$ provided the excitation source at wavelengths of 532 nm (2.33 eV photon energy), 405 nm (3.06 eV photon energy) and 632 nm (2.0 eV photon energy). The signal was monitored with a Si/avalanche photodiode. The signal was then divided in the X and Y channels of the lock-in amplifier and the phase of the lock-in amplifier was set by placing the scattered pump laser light in the X channel upon modulation at f_{pump}. Samples were held in a closed-cycle, sample-in-vapour cryostat with the exchange gas at 10 K during all measurements. This set up is shown in fig. 3.1 and the PL measurement were taken through the continuous wave laser optical path.

3.3 Background-free quasi-steady-state photoinduced absorption (PIA) spectroscopy by dual optical modulation

As mentioned in previous section all the measurements were taken using standard lock-in technique. This technique essentially permits to perform modulation spectroscopy by modulating a continuous wave laser with a mechanical chopper or acousto-optic modulator depending on the desired frequency. It is a powerful technique to analyse the electronic structure of materials by identifying photoinduced species such as polarons and triplet excitons and further investigate the kinetics by analysing the pump frequency dependent measurement. The approach to perform this measurement is double modulation with which the laser excitation beam and the probe beam are modulated at a frequency f_{pump} and f_{probe} respectively. The advantage of double modulation approach over standard photoinduced absorption geometry is that the output signal contains components at the individual frequencies f_{pump}, f_{probe} as well as the sum of frequencies $f_{pump} + f_{probe}$

and the difference frequency $f_{pump} - f_{probe}$. It is shown that with the double modulation approach the results from the ratio of the sum frequencies *i.e.* $\left(\Delta I_{out}^{f_{pump}+f_{probe}} / \Delta I_{out}^{probe}\right)$ is consistent with the results of the conventional single modulation configuration *i.e.* $\left(\Delta I_{out}^{f_{pump}} / \Delta I_{out}^{probe}\right)$. Therefore, the two methods characterise similar spectra. [57] This technique is essentially similar to the pump-probe spectroscopy with the difference that there is no delay between the pump and the probe beam in the PIA measurement.

3.3.1 Quasi-steady-state photoinduced absorption (PIA) signal

When the sample is exposed to the pump the transmission of the probe beam decreases. The difference in transmission *i.e.* ΔT, before excitation $T_{Pump-off}$ and after excitation $T_{Pump-on}$ is given by

$$\Delta T = T_{Pump-on} - T_{Pump-off}, \tag{3.4}$$

given that the change in transmission is related to the change in absorption coefficient α by induced excitation, and considering the Beer-Lambert law [58], one cay deduce that

$$T_{Pump-on} = T_{Pump-off} \exp\left(-n\sigma d\right), \tag{3.5}$$

$$n\sigma d = -\ln\left(1 + \frac{\Delta T}{T_{Pump-off}}\right), \tag{3.6}$$

$$\Delta T \ll T_{Pump-off} \rightarrow n\sigma d \approx -\frac{\Delta T}{T_{Pump-off}}. \tag{3.7}$$

The resulting signal characterises photoinduced absorption (PIA) ($\Delta\alpha > 0$) and photoinduced bleaching ($\Delta\alpha < 0$) where $n\sigma = \Delta\alpha$. In a PIA signal, new states are created whereas the decrease in the ground state optical transition by the pump pulse is called photobleach. In the PIA measurements, the sample is continuously illuminated by a modulated continuous wave laser pump, and the steady-state change in the transmission induced by the pump is monitored. The probe source is a white light, which can probe a broad spectral range.

3.3.2 Photoinduced absorption (PIA) instruments and measurements

Samples were held in a closed-cycle, sample-in-vapour cryostat (Cryo Industries, closed cycle model 350 optical refrigerator cryostat) with the exchange gas at 10 K during all measurements. To provide the excitation source, a semiconductor laser (Newport 532 nm, 200 mW) was modulated by an optical chopper at a frequency of $f_{pump} = 170$ Hz and directed to the sample. The probe beam was a monochromated 250-W halogen-tungsten lamp (Oriel) coupled to a 300-mm focal length monochromator (PI-Acton SP-2300i modulated at $f_{probe} = 139$ Hz. The two identical optical choppers (Terahertz Technologies model C-995) were used to generate references for lock-in amplifiers. The monochromated probe was imaged through the sample where it was overlapped with the pump laser beam, onto the entrance slit of a spectrometer with focal length 300mm. Two identical monochromators were used (PI-Acton SP-2300i). The output signal was monitored by a Si/Pbs dual-band photo-receiver (Electro-Optical Systems S/PBS-025/020-TE2-H). The output of this receiver was then split and sent to the input of two digital lockin ampliers (Stanford Research Systems SR830 and SR810). To provide an external reference for the two lock-in amplifiers, a home-built electronic circuit was employed; taking the TTL output of the two choppers and generates two input sine waveforms, one at 309 Hz (at $f_{pump=170\,Hz} + f_{probe=139\,Hz}$) and another at $f_{probe=139\,\mathrm{Hz}}$. The spectrometers and the cryostat are interfaced to a computer through a home-built labview program. Fig. 3.1 shows the schematic of our set up.

3.3.3 Pump modulation frequency dependent measurement

The advantage of this set up is that it permits one to measure pump modulation frequency dependence in a single modulation mode (without probe modulation), with the pump frequency ranging between 1 Hz to 30 KHz. In this measurement mode, the fractional change in transmission (ΔT) was corrected for sample photoluminescence (PL) recorded with the probe beam blocked $(\Delta T - PL)$, then normalized to the probe beam transmission measured with the pump laser blocked $(\Delta T - PL)/T$. The signal was monitored with a Si-avalanche photodiode.

Fig. 3.1 shows the schematic of our set up.

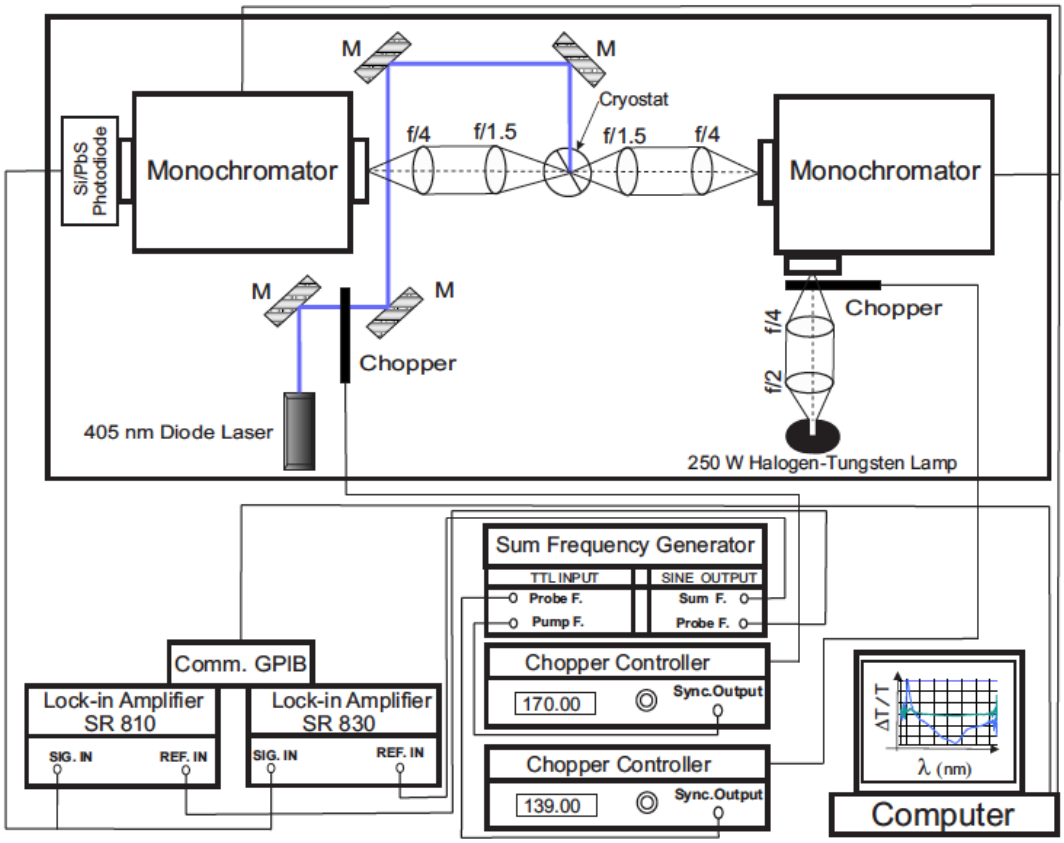

Figure 3.1 – Schematic diagram of the experimental instruments. Absorption measurement through the lamp optical path, PL measurement through the continuous wave laser optical path and the whole set up is used for the PIA measurement. Figure adopted from reference [57].

CHAPTER 4

THE INFLUENCE OF MOLECULAR INTERFACE MODIFICATION ON THE CHARGE DYNAMICS OF POLYMERIC SEMICONDUCTOR: ZNO HETEROSTRUCTURE

4.1 Introduction

This chapter presents the detailed photo-induced absorption (PIA) and pump modulation frequency dependent PIA measurements of hybrid bulk heterostructue of P3HT: ZnO in order to investigate the role of microstructure in charge generation and recombination at the interface of P3HT: ZnO. Certain parts of this chapter has been published in the journal of applied physics. [59] As mentioned in 2.3.2 organic-inorganic photovoltaic cells are an alternative type of donor-acceptor hetero-structures for solar power conversion to purely organic systems. They often incorporate conjugated polymers as donor materials and semiconductor nanocrystals as acceptors, with electronic structure optimised for photovoltaic diode operation. These cells present the opportunity to integrate favorable optoelectronic, chemical and thermal stability properties of inorganic nanocrystals and solution processability and low-temperature chemical synthesis of polymers. [45–47] In particular, zinc oxide (ZnO) due to the large bandgap, large electron mobility, and the high dielectric constant, [43, 51, 60] promises potential in organic-inorganic hybrid solar cells. [50] In spite of their potential, to date such cells display lower efficiency, especially lower photocurrent, compared to fully organic cells. [3, 4] Polymeric semiconductor: ZnO heterostructures were first prepared by Beek et al. and have been widely studied since. [51, 61, 62] Upon photoexcitation of the polymer, excitons dissociate at the organic-inorganic interface, with the positive charge located on the organic material and the electron on the inorganic semiconductor. [48] These charges are highly bound due to their mutual Coulomb interaction [63]. Recombination of bound pairs at the interface is considered to be a significant reason for the low efficiency. [43, 48] Furthermore, ZnO nanocrystals tend to aggregate, both during stor-

age and in use, owing to their surface hydrophilic properties and large surface areas. [51] This results in a lack of control over the solid-state microstructure in semiconductor-nanocrystals/polymer films, and thus presents a challenge in the development of hybrid photovoltaic cells. [49–51]

To develop better hybrid photovoltaic cells, it is important to focus on the donor-acceptor interface and the morphology of the active layer. Since the significant photophysical charge separation and recombination events occur at the polymer-inorganic interface, the efficiency of hybrid photovoltaic cells is highly sensitive to its modification. [64, 65] Moreover, charge transport is highly dependent on microstructure, which is in turn dependent on the nature of surface modification of the inorganic acceptors. [66] To date, several studies have explored the influence of interface modification on the optical absorption spectrum, charge recombination processes, charge separation kinetics, transport, and morphology of the hybrid heterostructure. [61] Shi et al. studied the interface modification of P3HT: ZnO heterostructure via P3HT-*b*-PEO, and found that phase segregation was reduced in this copolymer, which led to an enhancement of the photovoltaic properties. [67] Goh et al. have conducted comprehensive research to study the influence of interface modification on the efficiency of bilayer P3HT:TiO_2 by using a series of *para*-substituted benzene carboxylic acids with varying dipole moment. These authors demonstrated that both the acid-based interaction and the molecular dipole cause a band edge shift in TiO_2, which increases the open circuit volatge (V_{oc}). [68] Lin et al. demonstrated that charge recombination decreases in P3HT:TiO_2 following the attachment of effective ligand molecules consisting of carboxylate groups (-COOH) such as anthracene-9-carboxylic acid (ACA), tetra-carboxy phthalocyanine copper(II) (CuPc-dye) and N3-dye. [69] Vaynzof et al. demonstrated that interface modification of polymer:ZnO cells with a self-assembled monolayer (SAM) of phenyl-C_{61}-butyric acid (PCBA) improves the device efficiency. [48] In a later experiment using ultrafast optical pump-push photocurrent probe, those authors found that PCBA decreases the fraction of bound electron-hole pair states at the interface from 50% to 25%, which improves exciton dissociation yields. [48, 64] They also reported an improved external quantum efficiency (EQE) from 3% to 9%. [64] Shen et al. studied the influence of interface mod-

ification of P3HT: ZnO heterostructures with a dye (SQ36). [61] They found that charge recombination was reduced by locating the dye at the heterojunction interface. Boucle et al. studied the influence of interface modification with an amphiphilic ruthenium-based dye on P3HT:TiO_2 nanorods heterostructure. [70] They found that adding this dye at the interface contributes to better charge separation, although it does not affect the photocurrent due to the poor charge transport in the P3HT:TiO_2 blend films. [70] These studies show that understanding the underlying recombination mechanism and controlling, remains one of the main challenges in the study of organic-inorganic heterostructures. In what follows, we discuss how two dyes, adhered to the surface of the inorganic nanocrystals, increase the efficiency and the photocurrent of hybrid photovoltaic cells based on poly(3-hexylthiophene) (P3HT) and ZnO. We demonstrate that photocurrent is improved through the molecular interface modification. In addition, we study the nature of the photogenerated charges by means of photoinduced absorption (PIA) spectroscopy and determine the average lifetime of the photogenerated species (long-lived polarons) by means of combined pump modulation frequency dependence, and pump intensity dependence measurement of PIA signal. We find that the average lifetime of long-lived polarons becomes longer after interface modification.

4.2 Material processing and microstructure characterisation

This part of the project was performed by our collaborator, Dr. Mingqing Wang at Dalhousie university, physics department, Dr. Ian Hill group. Poly(3-hexylthiophene) (P3HT; BASF Sepiolid P200) was purchased from Rieke.

4.2.1 Synthesis and microstructure characterisation of ZnO nanocrystals

ZnO nanocrystals were synthesised the same method previously reported by Beek et al. [50] In this method ZnO nanoparticles were synthesised by hydrolysis and condensation of zinc acetate dihydrate by potassium hydroxide in methanol using a $Zn^{2+} : OH^{-}$ ratio of 1:1.7. Therefore the same X-ray diffraction is expected as shown in fig 4.1. X-ray diffraction spectrometry analyses the crystallinities of ZnO nanocrystals. The reflections

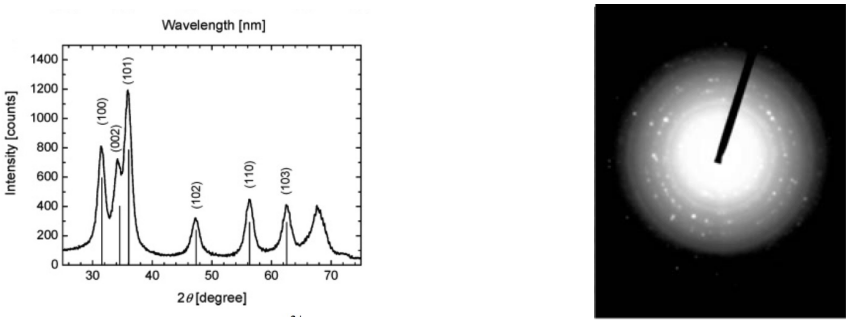

Figure 4.1 – Left: Powder XRD pattern of ZnO nanocrystals. Figure adopted from reference [50]. Right: Electron diffraction patterns of ZnO nanocrystals illustrate that hexagonal crystal structure are well crystallised, measurement taken by Mingqing Wang.

in the X-ray diffraction confirm the formation of a wurtzite-type ZnO crystalline phase. Moreover, the electron diffraction patterns illustrate that the hexagonal crystal structure multi-crystalline ZnO nanocrystals are well crystallised.

Furthermore, high-resolution transmission electron microscopy (HR-TEM) analysis was used to visualise the morphology of ZnO nanocrystals. Fig. 4.2 shows the TEM image of P3HT: ZnO composite films. The dark regions in the images are assigned to

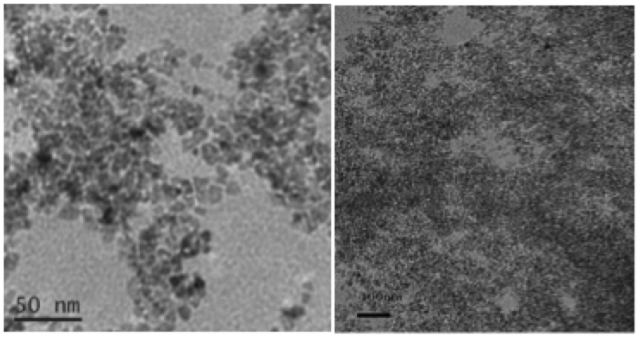

Figure 4.2 – High-resolution transmission electron microscopy (HR-TEM) image of ZnO nanocrystals. The dark regions in the images are assigned to ZnO-rich domains and the bright regions are assigned to P3HT-rich domains based on larger mass density of ZnO nanocrystal than that of P3HT. Measurement taken by Mingqing Wang at university of Dalhousie (Dr. Ian Hill group).

ZnO-rich domains and the bright regions are assigned to P3HT-rich domains based on larger mass density of ZnO nanocrystal than that of P3HT. At high magnification, it can

be seen that the size of the ZnO nanocrystals is around 5 nm. In our study on P3HT: ZnO heterostructure, ZnO nanocrystals with very small size (~ 5 nm) has been synthesised. In order to obtain a large area of the interface based on the fact that the excitons diffusion in P3HT is $2.5 - 8.5$ nm. [71]

4.2.2 Processing and characteristics of the interface modifiers

The materials used as interfacial modifiers on the interface of ZnO nanocrystals are cis-bis(4,4′-dicarboxy-2,2′bipyridine) ruthenium (II) (N3-dye), which has been widely used as sensitiser in dye sensitised solar cells, [72] and α-sexithiophen-2-yl-phosphonic Acid (6TP), synthesised for us by collaborators at Princeton University. [73] Fig. 4.3 shows the chemical structure of N3-dye and 6TP. To prepare ZnO nanocrystals with

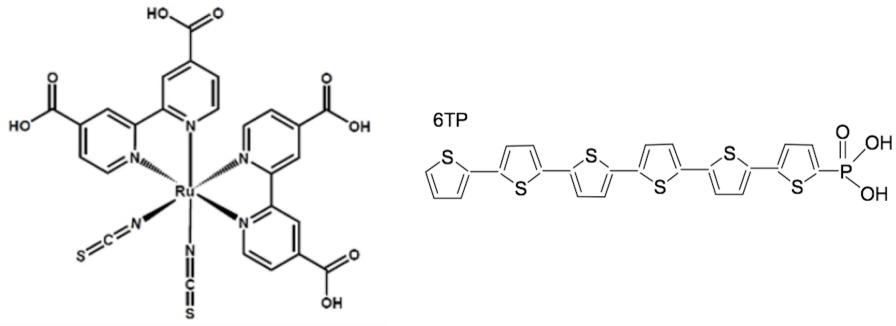

Figure 4.3 – Left: Scheme of chemical structure of cis-bis(4,4′-dicarboxy-2,2′bipyridine) ruthenium (II), right: α-sexithiophen-2-yl-phosphonic Acid.

the N3 dye, the ZnO nanocrystals were purified, centrifuged at 10000 rpm, and then dissolved in a N3/ethanol solution for 24 hours, after which the solution was centrifuged again. The ZnO-N3 nanocrystals thus obtained were rinsed three times with ethanol and then redissolved in chloroform at the concentration of 40 mg/ml. Both pure N3 and 6TP show good solubility in ethanol but extremely poor solubility in chloroform. The carboxyl group from N3 and phosphonic acid group from 6TP can strongly graft to the surface at ZnO. Therefore N3 and 6TP remain bound to the ZnO nanocrystals when re-dissolved in chloroform. The ZnO with 6TP added was prepared using a similar method. Blends of P3HT (10 mg/mL solution) with ZnO-N3 or ZnO-6TP (with ZnO solution

concentration 20 mg/ml) were prepared by spin-coating from solution. Note that the N3 and 6TP were used at different weight fractions with respect to the total weight of the blends (0.01 %, 0.1 %, 0.5 %), see appendix I for the calculation of the surface coverage of dye molecules on the surface of ZnO nanocrystals.

N3-dye grafts to the surface of ZnO via carboxylic acid groups, and contributes to slowing down the recombination kinetics due to its bulky and non-planar nature. [69, 74] 6TP contains two functional groups: phosphonic acid, which strongly attaches to the interface of the ZnO, and oligothiophene, which improves the mutual compatibility between P3HT and ZnO. [73, 75]

Fig. 4.4 shows the AFM images of P3HT: ZnO hybrid nanocomposite thin films with and without interface modification. AFM results show that interface modification of ZnO leads to lower surface roughness and better dispersion of ZnO in P3HT. The lower surface roughness can be assigned to the reduced traps on the surface of ZnO which might lead to decreased charge recombination in the composite.

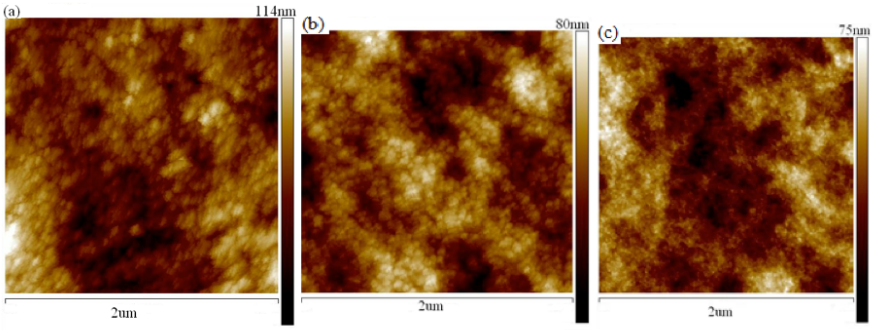

Figure 4.4 – AFM images (2 μm$\times$2 μm) of P3HT/ZnO nanocrystals composite before and after interface modification, note that D_z and rms indicate peak-to-peak height difference and root mean square roughness respectively. a) Pure ZnO/P3HT, D_z = 114 nm, rms roughness = 15.7 nm, b) 0.1 wt% of N3 , D_z = 80 nm, rms roughness = 10.8 nm, c) 0.1 wt% 6TP, D_z = 75 nm, rms roughness = 11.4 nm. Measurement taken by Mingqing Wang at university of Dalhousie (Dr. Ian Hill group).

Contact angle measurement provides qualitative and quantitative information on the chemical nature of the surface and, in particular, on the interfacial bonds between the interface modifiers and the ZnO nanocrystals. [76] ZnO inorganic nanocrystals are hydrophilic, P3HT is hydrophobic. The attaching of dye molecule on the surface of ZnO

can decrease the directly contact and agglomeration of ZnO nanocrystals. The grafting of hydrophobic dye molecule on ZnO surface increase the compatibility between ZnO and P3HT. Contact angle is used to measure the surface energy before and after dye modification of ZnO. In order to avoid the effect of different surface roughness on the contact angle, sputtered ZnO thin film of 50 nm was used as reference. The contact angle of pure ZnO film is 34°. After N3 modification, the contact angle increased to 44.75°. Since water can dissolve N3 molecule, so this might not be the real value. 6TP can attach strongly onto ZnO surface. The contact angle of 6TP modified ZnO film increased to 88.4°. As such it is expected that 6TP will have more impact on the surface modification of ZnO nanocrystals compared to N3, by increasing compatibility between ZnO nanocrystals and P3HT which is very hydrophobic in nature.

Fig. 4.5 shows the diagram of energy level alignment in the P3HT: ZnO-6TP (left) and P3HT: ZnO-N3 (right). The desired energy level alignment of all the components is such that a perfect energy cascade is set up.

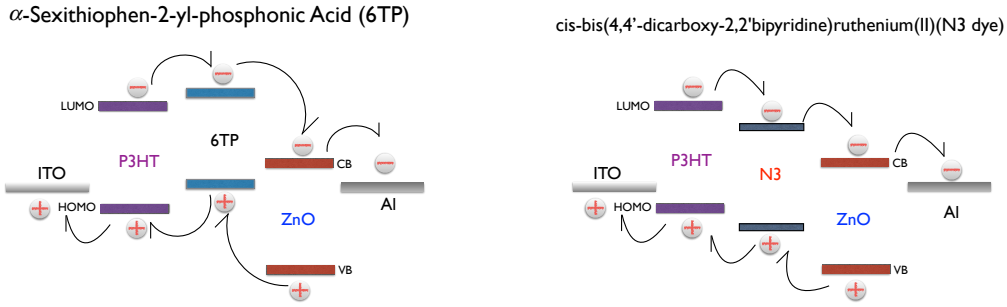

Figure 4.5 – Diagram of the energy level alignment in the left: P3HT: ZnO-6TP right: P3HT: ZnO-N3. All energy levels are not to scale and only intended to illustrate the approximate shape of the energy landscape.

In an inorganic semiconductor the filled molecular orbitals are referred to as the valence band (VB) and the unfilled molecular orbitals as the conduction band (CB). Similar to polymeric semiconductors that electrons can be promoted from HOMO to LUMO, electrons in inorganic semiconductors can be promoted from the valence band

into the conduction band. N3 and 6TP assemble between ZnO and P3HT with HOMO and LUMO aligning between the energy levels of ZnO and P3HT. This introduces an additional energetic step for electron and hole transfer, which supports separated charge carriers away from the interface and slows down recombination. The design of suitable interfacial modifiers, which induce alignment of the hole transporter, is a pathway towards increased efficiencies of hybrid photovoltaic cells. According to this energy diagram, relative to vacuum, (Fig. 4.5) the energy levels of N3 (LUMO and HOMO level of N3) lies between the energy levels of ZnO and P3HT where can form cascade charge transfer between ZnO and P3HT and decrease the charge recombination at P3HT: ZnO interface however in the energy levels of 6TP the perfect energy cascade is not set up. In fact, the conduction band level of ZnO is capable of accepting electrons from the LUMO of 6TP and N3, and the holes on P3HT can be injected into the ITO electrodes, see Fig. 4.5. Note that all energy levels are not to scale and only intended to illustrate the approximate shape of the energy landscape.

4.3 Working principles of organic photovoltaic cells

The basis and types of heterostructures as the active layers of organic photovoltaic cells has been partly discussed in chapter 2.3, in what follows physical working principles of bulk heterostructure organic photovoltaic cells is described as

1) Light absorption and exciton generation in the active layer.

2) Exciton diffusion towards the donor/acceptor interface, in competition with exciton recombination.

3) Exciton dissociation at the donor/acceptor interface and charge separation (CS).

4) Charge transport of electrons and holes towards the acceptor and donor respectively, and charge collection.

Fig. 4.6 is the scheme of working principles of bulk heterostructure organic photovoltaic cells in presence of an internal electric field.

Exciton Diffusion: Describing the exciton diffusion phenomenon is still a subject of debate. Due to the fact that reported exciton diffusion length in the literature is $\sim$

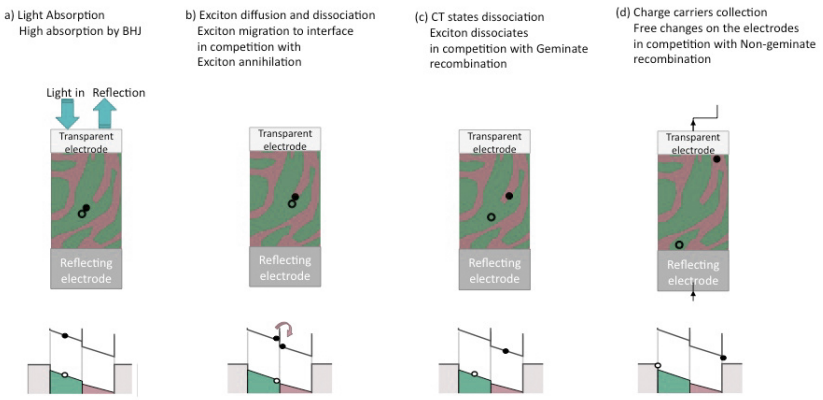

Figure 4.6 – Working principle of bulk heterostructures organic photovoltaic cells in presence of an internal electric field. (a) Light absorption within the active layer (b) Exciton diffusion towards the donor/acceptor interface and charge transfer (c) charge transfer state dissociation to free charges and (d) free charge carrier collection on the electrodes to generate photocurrent.

10 nm, for instance 2.5-8.5 nm in P3HT. [71] In a bulk heterostructure including 10 nm polymer size, the required time for exciton to reach the interface is $\sim 10-100$ ps. On the other hand, the experimental results show that charge generation occurs within 100 fs from the initial absorption therefore, within this time scale excitons can only migrate about 0.1-0.3 nm and cannot reach the interface (within 10 nm). Recently, Scarongella et al. used ultrafast photoluminescence up conversion spectroscopy and observed ultrafast charge generation $<$100 fs as it is commonly observed. Scarongella et al. supposed that the charge separation is an instantaneous phenomenon and occurs at once the exciton is delocalised. Therefore, the charge separation at the donor/acceptor interface area is created directly from delocalised excitons. This topic has been extensively discussed in the literature. [44]

The free charge-generation process: Once an exciton reaches an interface, dissociated exciton at the interface creates a bound electron-hole pair. [77] which is still not free from recombination. In fact, there is an intermediate step between the exciton creation and free charges termed as charge transfer (CT) state. As the electron and

hole sitting on adjacent molecules on either side of the interface are still Coulombically bound and have a binding energy still higher than the thermal energy present at room temperature this geminate charge pair will also recombine after a finite time unless induced to separate by some other process. This will both waste the energy of the exciting photon and reduce the free charge generation and the resulting photocurrent. This loss mechanism is referred to as geminate recombination, as it involves the recombination of two opposite charges generated by the same photon. These processes are described as unimolecular or first order process (although these terminologies shall be discussed later in this chapter) as the rate of recombination depends only upon the density of one species, the excitonic charge transfer state, not upon the concentrations of both electrons and holes. Alternatively, if the charge transfer state is separated via some non-specified mechanism then a free electron and free hole have been generated in respective donor and acceptor materials. Fig. 4.7 shows the scheme of free charge generation, charges in charge transfer state can either undergo geminate recombination (black downward arrows) or become free charges (polarons). Free charge carriers must reach their respective

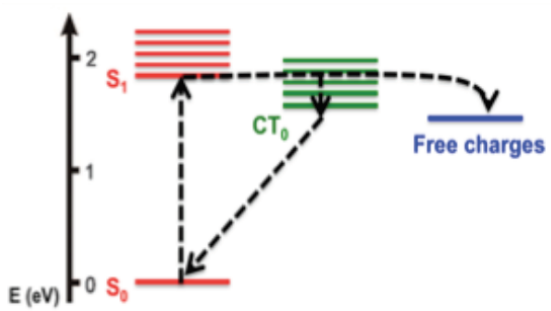

Figure 4.7 – Scheme of free charge generation. The exciton created in S1, can migrate to charge transfer state to either become a free charge or relax to CT_0 and undergo a geminate recombination. Figure adopted from reference [44].

electrodes to contribute to the photocurrent. Holes move towards the high work function electrode, typically Indium Tin Oxide (ITO), and electrons move towards the low work function electrode, typically aluminium. Dissociation creates a concentration of holes in one chemical phase, and a concentration of electrons in the other chemical phase. This spatial segregation of photogenerated charge carriers does not occur in inorganic photo-

voltaic cells and results in a powerful driving force for carrier separation that is unique to organic photovoltaic cells.

4.3.1 The effect of interface modifiers on the working principle of P3HT: ZnO hybrid photovoltaic cell

Fig. 4.8 shows how the dyes adhere to the surface of the inorganic nanocrystals and improves affinity between P3HT and ZnO. The non-workable area (shown in white

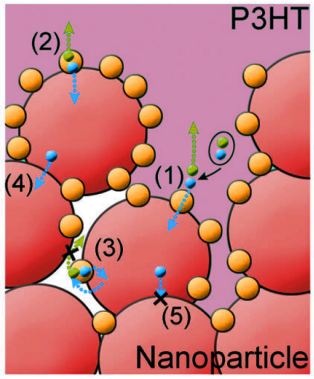

Figure 4.8 – Charge transport mechanism of P3HT: ZnO-dye. The dyes shown in the yellow circles, the electron (hole) pathways are in blue (green) arrows. The non-workable area is in white colour, ZnO nanocrystals in orange and P3HT in pink. (1) exciton diffusion and separation at P3HT: ZnO-dye interface, (2) photogenerated charge carrier of the dye, (3) recombination at the non-workable ZnO/dye/air interface, (4) charge transport along the nanoparticle, (5) trapping or charge recombination at the boundaries of the nanocrystals. Figure adopted from reference [78].

colour) is the ZnO/dye/air interface which needed to be comparable to the exciton diffusion length of P3HT such that photogenerated excitons from P3HT are able to reach the P3HT: ZnO-dye interface for charge separation (process 1). The excitons mainly originates from the light absorption of P3HT together with the light absorption of dye molecules by injecting electrons to conduction band of ZnO and holes to HOMO of P3HT (process 2). The morphology of nanocrystals plays a significant role in P3HT: ZnO-dye interface area such that it may limit these two processes. Moreover, the effective density of state of the ZnO nanocrystals, which is related to the basic crystal size (due to the quantum confined effect), is significant for the electron accepting ability. The

ZnO/dye/air interface causes the imperfect exciton separation and charge recombination instead (process 3). After the exciton separation process, free electrons transfer along the nanocrystals to the electrode (process 4) which is in competition with charge trapping or recombination at the boundaries (process 5) that probably limits the short circuit current. [78]

4.4 Electrical characterisation

Before discussing the $J-V$ curve analysis of our photovoltaic cells, it is necessary to clarify a few fundamental parameters that are used to describe device performance, as well as how a device is measured. The purpose of the solar cell is to deliver power $(V \times I)$. In a $J-V$ curve there is a point where the power reaches its maximum value (P_{max}), J is photocurrent normalized to the area of the cell and V is the voltage.

Open-Circuit Voltage (V_{oc}) : Open-Circuit Voltage is the photo-voltage when the load resistance is infinite or simply when the circuit is open in a photovoltaic cell. In such a case there is no driving voltage in the device to extract the photo-generated carriers and they recombine except for those that charged the electrodes initially.

Short-Circuit Current (J_{sc}) : Short-Circuit Current is the photo-generated current of the photovoltaic cell when the electrodes are connected directly or the only load resistance on the photovoltaic cell in this condition is its own resistance. J_{sc} is strongly dependent on the number of absorbed photons that can be supported by a wide absorption spectrum and incident light intensity.

Fill factor (FF): Fill factor is the ratio of maximum power delivered by the photovoltaic cell represented by rectangular area. To characterise a photovoltaic cell, three parameters are usually considered: the open circuit voltage, the short circuit current and the fill factor, given by

$$FF = \frac{J_{MPP}V_{MPP}}{J_{sc}V_{oc}}, \tag{4.1}$$

where J_{MPP} and V_{MPP} are the current density and voltage at the maximum power point MPP, respectively. MPP is the voltage at which the product $|JV|$ is at its maximum. It

is also possible to define the FF as

$$FF = \frac{(J.V)_{max}}{J_{sc}.V_{oc}}. \tag{4.2}$$

Ideally, fill factor should be unity however due to the recombination and charge transport limitations its value lies between $\sim 0.25 - 0.85$ in organic photovoltaic cells. Fill factor is related to the operational condition of the photovoltaic cell. [79] Fig. 4.9 shows the JV characteristics of a photovoltaic cell.

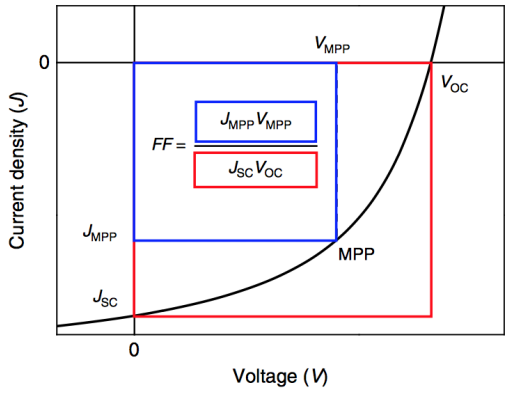

Figure 4.9 – JV characteristic of a photovoltaic cell. Figure adopted from reference [79].

Power conversion efficiency (PCE) : Power conversion efficiency of an organic solar cell is the ratio of the output power of the cell and the input light power and is given by

$$PCE = \frac{J_{SC}V_{OC}}{P_{in}} FF \times 100\%, \tag{4.3}$$

where P_{in} is the input light power. As equation 4.3 shows it is possible calculate PCE from $J-V$ characteristics. In short, PCE. reflects how efficient the light energy is converted to electricity in an organic solar cell.

4.4.1 $J-V$ curve analysis

To examine the photocurrent response of the hybrid photovoltaic cells with P3HT: ZnO-N3 and P3HT: ZnO-6TP, and to compare them with P3HT: ZnO, we fabricated

device structures consisting of a glass/ITO/ PEDOT:PSS/ P3HT: ZnO/ Al. Here, we address the influence of molecular-interface modification in hybrid P3HT: ZnO based photovoltaic cells by measuring the current density as a function of voltage. The measurements were taken in air at room temperature using a Keithley 236 source measurement unit under the intensity of $\sim 100\,\mathrm{mW/cm^2}$, with white light illuminated by a Newport/Oriel 150W solar simulator equipped with an AM1.5G filter. The performance observed depended on the weight fractions of the interface modifiers (N3 and 6TP), which demonstrates the influence of these interface modifiers. We present the current density as a function of voltage for an additive weight fraction of 0.1%, corresponding to the best performance. The current density-voltage plots of the cells with P3HT: ZnO, P3HT: ZnO-N3 and P3HT: ZnO-6TP are shown in Fig. 4.10 and characteristics are summerised in table 4.I. As demonstrated by the current density-voltage characteristics, both the short-circuit current (J_{sc}), and the open circuit voltage (V_{oc}) are significantly improved through the molecular interface modification by attaching the N3 and 6TP molecules to the interface of ZnO. In addition, the obtained value for the V_{oc} of P3HT: ZnO, *i.e.* 0.54 V, is very similar to the reported V_{oc} in the literature. [80] Moreover, with the use of these interface modifiers, we could improve the efficiency of the hybrid photovoltaic cells based on P3HT: ZnO as shown in table 4.I. The increase of J_{sc}, in particular in P3HT: ZnO-6TP, can be attributed to two factors: the increase of the interfacial area between the donor and the acceptor and the decrease of ZnO interface traps.

Table 4.I – Short current density (J_{sc}), open circuit voltage (V_{oc}), power conversion efficiency (η), and fill factor (FF) of P3HT: ZnO, P3HT: ZnO-N3, and P3HT: ZnO-6TP hybrid photovoltaic cells under 100-mW/cm^2 illumination.

Electron acceptor	J_{sc} (mA/cm^2)	V_{oc} (V)	η (%)	FF
ZnO	2.42	0.54	0.74	0.57
ZnO-N3	3.44	0.66	1.24	0.55
ZnO-6TP	3.91	0.57	1.14	0.52

The increase in V_{oc} is due to a shift in the band offset at the P3HT: ZnO interface since it is limited by the difference between the energy at the conduction band minimum of ZnO and that of the highest occupied molecular orbital of P3HT. [81, 82] That shift

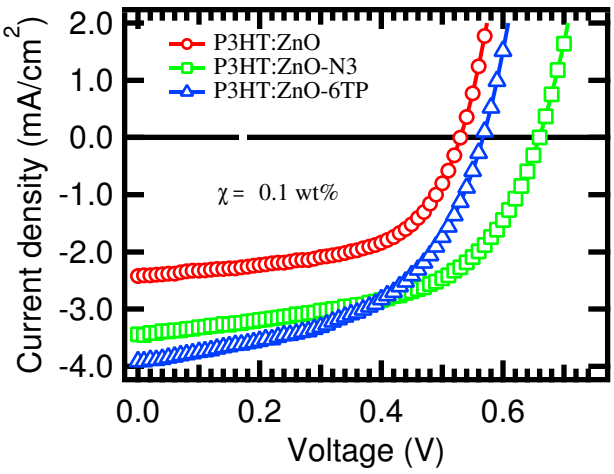

Figure 4.10 – Current density-voltage characteristics of hybrid photovoltaic cells based on P3HT: ZnO, with and without N3 and 6TP interface modifiers under solar illumination intensity of $\sim 100\,\mathrm{mW/cm^2}$.

is caused by the generation of interfacial dipole moments pointed outward the ZnO interface. Fig. 4.10 shows that V_{oc} is very sensitive to molecular interface modification. Therefore the increase in the V_{oc} accounts for the decrease in both energy loss across the heterojunction and carrier recombination yield. We conclude that the interface modification of a hybrid P3HT: ZnO device with N3 and 6TP significantly improves the performance of these cells. [59] This section has been widely discussed in section 4.7.1.

4.5 Photophysical properties of P3HT: ZnO hybrid photovoltaic cell

The question that motivates this part of the work is to relate the increase in the V_{oc} and J_{sc} to the changes in the microstructure that can be done through the spectroscopic tools. In what follows, we have shown how the photophysical responses of P3HT: ZnO active layers (by using the steady-state techniques explained in chapter 3) permits us to obtain the average lifetime of long-lived species (polarons) and relate it to the microstructure of P3HT: ZnO, to conclude about the influence of the interface modification on the efficiency of those active layers.

4.5.1 Linear absorption spectra

Fig. 4.11 (left) shows the UV-VIS absorption spectra of ZnO, ZnO-N3 and ZnO-6TP nanocrystals in ethanol solution. The absorption of ZnO is within the range of 270-350 nm. The absorption spectra measured after interface modification of ZnO nanocrystals are similar to that of correspond to ZnO nanocrystals however there is also a weak peak between 400-550 nm for ZnO-N3 and ZnO-6TP nanocrystals which is assigned to the absorption of dye molecules. Since the amount of grafted dye is not high, the absorption peak of dyes is not very strong. Fig. 4.11 (right) shows the linear absorption spectra were obtained using standard lock-in techniques detailed in chapter 3.1, technical limitation prevented us from measuring wavelengths lower than 400 nm. The absorption spec-

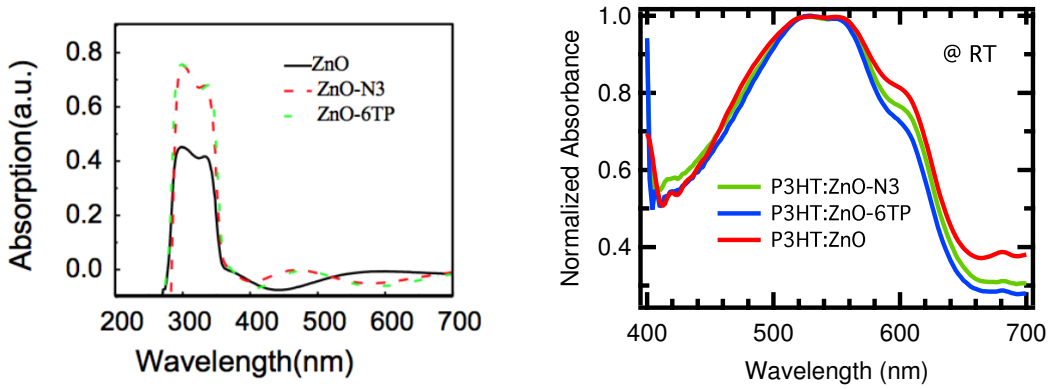

Figure 4.11 – Left: UV-VIS absorption spectra of ZnO, ZnO-N3 and ZnO-6TP, taken at Dalhousie university. right: Normalized absorption spectra of P3HT: ZnO-6TP, P3HT: ZnO-N3 at 290 K.

tra of P3HT: ZnO before and after interface modification of ZnO nanocrystals are similar to that of correspond to neat P3HT as reported in the literature. [34] Furthermore, the absorption of P3HT: ZnO before and after interface modification show vibronic replicas centred at $A_{0-0} = 604$ nm and $A_{0-1} = 552$ nm that is consistent with the values reported in the literature for P3HT. [83] The ratio of the vibronic progression is given by [30]

$$\frac{A_{0-0}}{A_{0-1}} \approx \left(\frac{1 - 0.24W/\hbar\omega_0}{1 + 0.073W/\hbar\omega_0} \right)^2, \tag{4.4}$$

where $\hbar\omega_0$=170-180 meV is the effective energy of the main intramolecular vibrational mode coupled to the electronic transition, (the origins of the vibronic progression were discussed in chapter 2.2.2). According to the weakly coupled H-aggregate model by Spano [21] (discussed in 2.2.3) a decrease in the ratio leads to an increase in the exciton bandwidth and coupling between the chains and torsional disorder within the chains. [34, 84] Our optical absorption data presented in Fig. 4.11 (right) shows that the $0-0$ to $0-1$ drops after interface modification thus suggests that W increases, *i.e.* interchain coupling increases. We associate this variation in W between the thin films before and after interface modification to conformational changes and torsional disorder resulting from different average chain lengths associated with these films. It is concluded that the interface modifiers increase the coupling between the π-stacks in P3HT, and change the microstructure of P3HT.

Paquin et al. previously demonstrated that by increasing the molecular weight of P3HT the exciton bandwidth decreases and it reduces the torsional disorder in the polymer backbone. [34] Consequently, the vibronic progressions in the absorption spectrum offer information about the microstructure.

4.5.2 Photo-induced absorption spectra

As mentioned in chapter 2.1.4, it is possible to identify the different absorption peaks through the photo-induced absorption (PIA) technique. Quasi-steady state photoinduced absorption (PIA) spectra were obtained using standard lock-in techniques detailed in chapter 3.3. To account for the enhancement of device performance, and to further investigate the charge dynamics of P3HT: ZnO based heterostructures, we carried out photoinduced absorption measurements (PIA) at 10 K on thin films of P3HT: ZnO, P3HT: ZnO-N3, and P3HT: ZnO-6TP.

The PIA spectra of the three active layers in Fig. 4.12 reveal two principal features: a broad band peaked at 1.3 eV and a weaker peak in the near infrared centered at 0.62 eV. Those peaks are associated with high- and low-energy sub-gap polaronic absorption in P3HT. [85] Note that the transition in the PIA spectrum of P3HT: ZnO, peaked at 1.3 eV, is identical to that reported previously by Oosterhout et al. [86] This peak is consid-

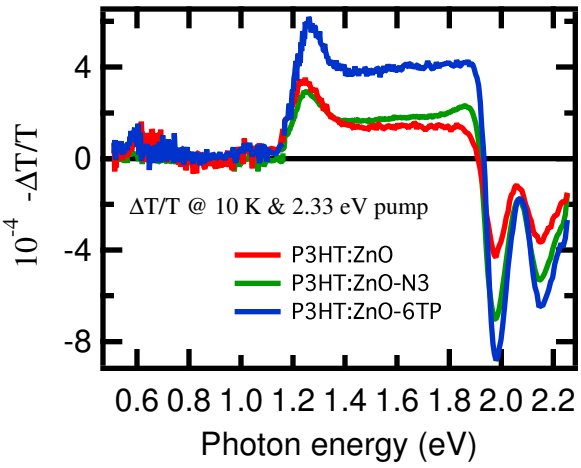

Figure 4.12 – The PIA spectra of P3HT: ZnO (in red circles), P3HT: ZnO-N3 (in green squares) and P3HT: ZnO-6TP (in blue triangles). The spectra show a high-energy polaron centered at 1.3 eV and low energy polaron at 0.62 eV. The measurements were acquired at 10 K with excitation at 170-Hz modulation frequency by a continuous-wave 532-nm laser.

ered as a result of photoinduced charge generation. [87] The infrared peak is also very similar to that of reported value. [86] The high-energy peak is assigned to be a characteristic of polarons generated on the polymer (P3HT) chain. [88, 89] The spectral line shape is similar before and after molecular interface modification, and the magnitude of the photo-induced absorption signal is higher in P3HT: ZnO-6TP than P3HT: ZnO and P3HT: ZnO-N3; which is possibly dependent on the active layers thickness or the optical density of these active layers. The goal is to study the decay dynamics of polaron band at 1.3 eV.

4.6 Charge dynamics in bulk heterostructures

As discussed previously (chapter 2.3.3) the donor acceptor interface in organic bulk heterostructures is complicated due to the formation of the different phases therefore identifying the recombination process is not straightforward. Photoexcitation process creates exciton whereas recombination process annihilates either the bound electron hole pair at the interface (where electron resides in the LOMO and the hole resides in the

HUMO) or annihilates free charges.

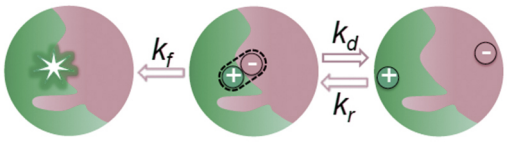

Figure 4.13 – Scheme of the donor acceptor interface in a bulk heterostructure. k_d: dissociation rate in competition with k_r: recombination rate to form bound polaron pair which can decay with the rate k_f.

4.6.1 Recombination dynamics

Geminate (unimolecular) recombination is associated with recombination of polarons originated from the same exciton (bound electron hole pairs at the interface) whereas non-geminate (bimolecular) recombination is associated with recombination of polarons which are not originated from the same exciton (dissociated free charges). In order to understand the recombination dynamics in organic or hybrid bulk heterostructures, we can simply use the rate equation given by

$$\frac{dn}{dt} = G(t) - R(n), \tag{4.5}$$

$\frac{dn}{dt}$ is the change in the carrier density per unit time, G is the carrier generation rate and R is the carrier recombination rate. In the steady-state condition (continuous wave pump) equation 4.5 gives

$$\frac{dn}{dt} = G - R = 0, \tag{4.6}$$

G=R. $G(t)$ as the pump photomodulation function with angular frequency ω can be approximated to a periodic wave *i.e.* $\kappa\rho I\cos(\omega t+1)$, where I is the pump intensity, κ is the number of species generated per absorbed photon, ρ is the rate of photon absorption per unit volume.

Unimolecular recombination is a first-order kinetic, the rate equation is given by

$$\frac{dn}{dt} = \kappa\rho G(t) - \gamma n, \tag{4.7}$$

where γ is the unimolecular decay rate constant. In the steady-state condition (if $\omega\tau < 1$) the exact solution to the equation 4.7 is given by

$$n(t) = \kappa\rho I\tau\left[\frac{1}{\sqrt{1+\omega^2\tau^2}}\cos(\omega t - \phi) + 1\right], \qquad \tan\phi = \omega\tau, \tag{4.8}$$

where ϕ is the phase of the emitting radiation and τ is the average lifetime of the photogenerated carriers. The steady-state carrier intensity n_{ss} extracted from equation 4.8 is

$$n_{ss} = \frac{\kappa\rho I\tau}{\sqrt{1+\omega^2\tau^2}}. \tag{4.9}$$

Note that n_{ss} is linearly dependent on pump intensity I whilst the lifetime is independent of pump intensity during the relaxation process.

Bimolecular recombination is a second-order kinetic, rate equation is given by

$$\frac{dn}{dt} = \kappa\rho G(t) - \beta n^2, \tag{4.10}$$

where β is the bimolecular decay rate constant. However equation 4.10 cannot be exactly solved because it is not possible to associate a lifetime independent of the light intensity to the relaxation process. The approximate solution to equation 4.10 is given by

$$n_{ss} = \frac{N\alpha\tanh(\alpha)}{\alpha + \tanh(\alpha)}, \tag{4.11}$$

where $N = \sqrt{\kappa\rho I/\beta}$, $\alpha = \frac{\pi}{\omega\tau_s}$. $\tau_s = \frac{1}{\sqrt{gI\beta}}$ is a certain lifetime under the steady-state condition. [90]

Based on $N = \sqrt{\kappa\rho I/\beta}$, n_{ss} suggests a sublinear power law dependence with pump intensity I with an exponent of 0.5. Therefore, bimolecular recombination is manifested by a square-root dependence on pump intensity. Fig. 4.14 shows simulated intensity dependence of the decay dynamics which is constant in the first-order decay, also independent of the initial carrier density n_0, whereas second-order decay dynamic is carrier density dependent and it is half at twice the n_0. Therefore, carrier density dependence of decay time and of pump intensity characterise the nature of recombination dynamics

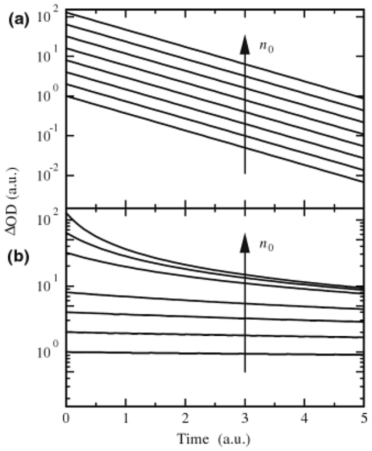

Figure 4.14 – Intensity dependence of the simulated transient absorption decays for a: the unimolecular and b: the bimolecular recombination. In the first-order kinetic the life time is independent of the initial carrier density n_0, whereas in the second-order kinetic the life time is dependent of the initial carrier density n_0. Figure adopted from reference. [91]

thus provide tool to distinguish whether the electron-hole pairs are bound at the interface or dissociated as free charges.

4.6.2 Results and analysis

As shown above, the carrier intensity (n_{ss}) is dependent on the the pump intensity (I) (equations 4.9 and 4.11). It is possible to determine the recombination processes of photo-generated species and to further investigate the contribution of monomolecular and bimolecular recombinations by the pump intensity dependence of the PIA signal. [92, 93] Fig. 4.15 shows the dependence of the PIA signal on the pump intensity, probed at 1.3 eV for all three active layers studied in this work. For all three samples, fits to a polynomial function $ax+bx^c$ show that the data depends linearly on pump intensity at low intensities, and turns to a sub-linear dependence at higher pump intensities. Fits to the data produce a, b and c as reported in the table 4.II

Table 4.II – Fits to a polynomial function $ax+bx^c$

Materials	a	b	c
P3HT: ZnO	$a=(9.10\pm0.01)\times10^{-8}$	$b=(1.40\pm0.01)\times10^{-5}$	$c=0.40\pm0.04$
P3HT: ZnO-N3	$a=(2.08\pm0.01)\times10^{-10}$	$b=(8.14\pm0.09)\times10^{-6}$	$c=0.50\pm0.06$
P3HT: ZnO-6TP	$a=(7.06\pm0.02)\times10^{-7}$	$b=(1.01\pm0.04)\times10^{-5}$	$c=0.66\pm0.03$

As such, we consider the rate model for the photoexcitation generation and decay kinetics (discussed in 4.6.1) in the presence of the unimolecular and the bimolecular

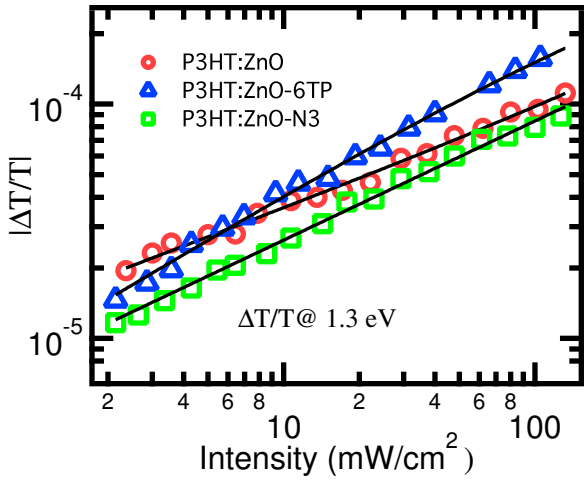

Figure 4.15 – Log-log plot of the pump intensity dependent PIA signal, for all three active layers studied in this work, at 10 K, exciting at 2.3 eV, and probing at 1.3 eV. The experimental data are represented by symbols and the solid lines represent fits to a polynomial function $ax + bx^c$.

recombinations [93] which is given by

$$\frac{dn}{dt} = G(t) - \gamma n - \beta n^2, \tag{4.12}$$

and the solution to the rate equation, when $G(t) \equiv \kappa\rho I \cos(\omega t + 1)$, is

$$n_{ss} = \frac{\kappa\rho \tanh\left(\frac{\gamma\pi}{2\omega}\right)\tanh\left(\frac{P\pi}{\omega}\right)}{\frac{\gamma}{2}\tanh\left(\frac{P\pi}{\omega}\right) + P\tanh\left(\frac{\gamma\pi}{2\omega}\right)}, \tag{4.13}$$

in which

$$P = \sqrt{\kappa\rho\beta + \frac{\gamma^2}{4}}. \tag{4.14}$$

Based on this model it is essential to plot n_{ss} as a function of ρ. The carrier density n is related to the PIA signal via the Beer-Lambert law such that

$$n = -\frac{1}{\sigma d}\ln\left(1 + \frac{\Delta T}{T}\right), \tag{4.15}$$

where σ (cm^2) is the polaron absorption cross section, d is the film thickness (cm) and $\frac{\Delta T}{T}$ is the pump-intensity dependent PIA signal.

As shown in Fig. 4.16, the deviation from linearity at higher pump intensity is a manifestation of the bimolecular recombination kinetics. Fitting these data to equation 4.13 allows extraction of γ and β, which are reported in table 4.III. The continuous curves represent fits to equation 4.13. Note that ω is the pump frequency at which the power-dependent data has been taken, *i.e.* ω=170 Hz, and the absorption cross section (σ) is $\sim 10^{16}$ cm^2. [94]

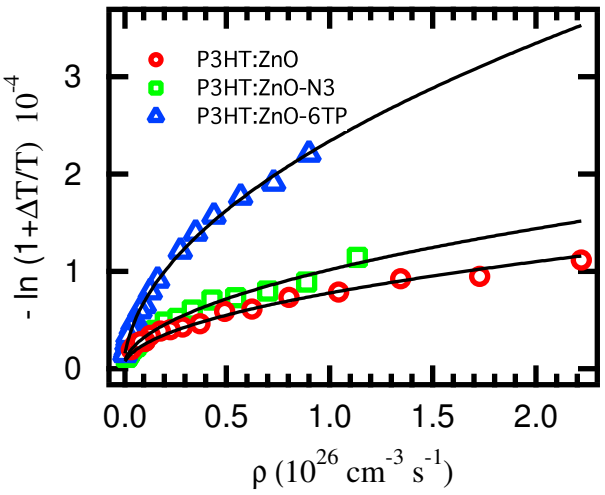

Figure 4.16 – PIA signal as a function of the rate of photon absorbed per unit volume, in which the ordinate axis is proportional to population density n_{ss}. In this case $n_{ss} \sim 10^{14}$ cm^{-3} assuming the absorption cross section (σ) of $\sim 10^{16}$ cm^2. [94] The continuous curves represent fits to equation 4.13.

Table 4.III – Summary of unimolecular (γ), bimolecular (β) at 10 K with fitting equation 4.13 to the data points on Fig. 4.16.

Materials	$\gamma(10^3 s^{-1})$	β (10^{-14} s^{-1} cm^3)
P3HT: ZnO	2±0.07	3.95±0.31
P3HT: ZnO-N3	1.3±0.05	0.16±0.04
P3HT: ZnO-6TP	1±0.1	0.66±0.03

4.6.3 Frequency domain lifetime measurement

As mentioned above, it is possible to determine the mechanism of the long-lived photoexcitation including recombination dynamics, in the time domain, by photoinduced absorption (PIA) measurement. Given τ is an average life time associated with the carrier density then, if $\omega\tau < 1$, τ is short compared to the pump modulation period, the photo-excitation density does not exhibit significant changes with ω as the population is close to a steady state. On the other hand, for $\omega\tau \approx 1$, τ is long compared to the pump modulation period and the photoexcitation density cannot fully decay within that period, which results in the intensity of the photo-induced absorption signal decreasing with frequency. [92, 93, 95, 96] That relaxation behaviour is a characteristic for all semiconductor polymers. Investigation of the pump modulation frequency dependence of the PIA signal provides insight on the kinetics of long-lived polarons (the techniques detailed in chapter 3.3.3 and 4.6.3). We measured such frequency dependence of all three active layers at 10 K, monitored at a fixed probe energy of 1.3 eV, with a fixed pump intensity of 250 mW/cm^2, excited at 2.33 eV. As shown in Fig. 4.17 the decay behaviour of the 1.3-eV band of P3HT: ZnO is significantly different than that of P3HT: ZnO-N3 and P3HT: ZnO-6TP. After interface modification, the intensity of the PIA signal turns over from steady state to off-steady state at lower frequency, which is characteristic of longer-lived polarons. [97, 98]

Following the extraction of the unimolecular (γ) and bimolecular (β) recombination coefficients from the power dependence data using the rate model, it is possible to find the average lifetime of polarons as $\tau^{-1} = \gamma + n_{ss}\beta$, with n_{ss} determined by the Beer-Lambert law as discussed in section 4.6.3, *i.e.* $n = -\frac{1}{\sigma d}\ln\left(1+\frac{\Delta T}{T}\right)$, in this case $\frac{\Delta T}{T}$ is extracted from frequency-dependent data. In addition, equation 4.13, with the unimolecular and bimolecular recombination rate constants extracted from the pump intensity-dependent data, can also be used to fit the frequency-dependent data. The continuous lines through the data in Fig. 4.17 represent fits to equation 4.13 using γ and β reported in Table 4.IV. The reported range of τ in table 4.IV corresponds to n_{ss} throughout the range of values of ρ used in Fig. 4.16. We note that the average lifetime becomes longer

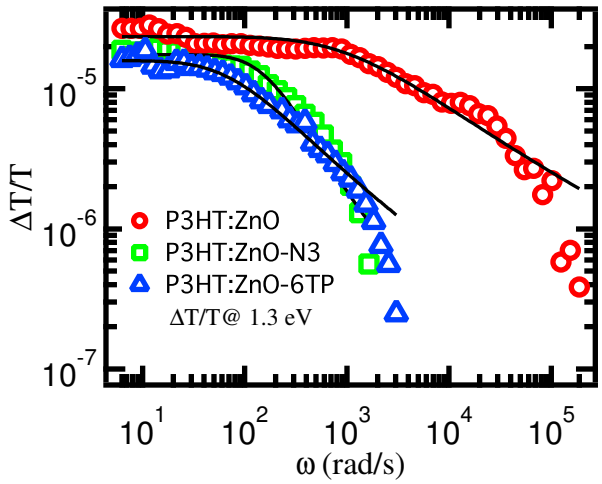

Figure 4.17 – The pump modulation frequency-dependent PIA signal, for all three active layers studied in this work. The data were measured at a probe energy of 1.3 eV and at 10 K. The experimental data are represented by symbols: P3HT: ZnO (in red circles), P3HT: ZnO-N3 (in green squares) and P3HT: ZnO-6TP (in blue triangles). Solid lines represent fits to equation 4.13. The angular frequency dependence of PIA signals clearly demonstrate a sharper decrease with frequency in hybrid active layers with either of the surface modifier molecules compared to P3HT: ZnO.

Table 4.IV – The total lifetime ($\tau^{-1} = \gamma + n_{ss}\beta$) at 10 K with fitting equation 4.13 to the data points on Fig. 4.16.

Materials	τ (ms) [1]
P3HT: ZnO	0.19-0.44
P3HT: ZnO-N3	0.76-1.03
P3HT: ZnO-6TP	0.87-0.99

in P3HT: ZnO-N3, and P3HT: ZnO-6TP by over a factor of two compared to P3HT: ZnO, consistent with a slowing down of recombination and more stable charge separation in the cells with interface modifiers. [98]

We note that according to equation 4.13, we ideally expect a falloff of the PIA signal with frequency as ω^{-1}. In fact, we observe that the signal falls as $\omega^{-0.66}$ for P3HT: ZnO-6TP, $\omega^{-0.60}$ for P3HT: ZnO-N3, and $\omega^{-0.35}$ for P3HT: ZnO. Due to the fact that ω^{-1} dependence is expected for one rate constant however our frequency-dependent results shows distribution of rate constants, hence it presents a power-law behaviour.

That highlights the dispersive nature of charge recombination due to a distribution of lifetimes, rather than a narrow recombination rate, as discussed in section 4.6.3. Due to the fact that the PIA signal decays slowly at high modulation frequency, it is not possible to introduce a specific lifetime that is independent of light intensity therefore we limited the case to the average lifetime under the steady-state condition. [92]

4.6.3.1 Discussion on the frequency dependence decay

In the presence of unimolecular and bimolecular recombinations, from equation 4.13 for $\omega\tau \ll 1$ (steady state regime)

$$n_{ss} = \frac{\gamma}{2\beta}\left[\sqrt{1+4\beta\kappa\rho I\gamma^{-2}}-1\right], \tag{4.16}$$

become independent of ω and with I increasing with changeover from I to $\sqrt{I}$ dependence when bimolecular regime becomes dominant. While for $\omega\tau \sim 1$ (off steady state regime) ω^{-1} law is predicted.

In the most general case, a photoluminescence decay can be written in the following form [99]

$$N(t) = \int_{-\infty}^{t} G\left(t'\right) I\left(t-t'\right) dt', \tag{4.17}$$

where $N(t)$ is the response to an excitation source, $G(t)$ can be regarded as a distribution of rate constants, as the non-monotonic signal decreases with time or frequency, for a square wave generation (continuous-wave spectroscopy) $G(t)$ is given by

$$G(t) = \frac{1}{2} + \frac{2}{\pi}\sum_{k=1,3,5}^{\infty}\frac{1}{k}\sin\left(k\omega t\right), \tag{4.18}$$

the detailed calculation can be found in reference [99], provided that $N(t)$ can be expressed as a Fourier series, the inverse Laplace transform contributes to the coefficients as

$$X(\omega) = \frac{2}{\pi}\frac{1}{k}\int_{0}^{\infty}\cos\left(k\omega\tau\right) I(\tau)\, d(\tau), \tag{4.19}$$

$$Y(\omega) = -\frac{2}{\pi}\frac{1}{k}\int_0^\infty \sin(k\omega\tau)\, I(\tau)\, d(\tau), \tag{4.20}$$

when the population decays as $I(t) \sim t^{-\mu}$, if $0 < \mu < 1$, equations 4.19 and 4.20 suggest that the frequency dependence (decay at high frequencies) should be as $\omega^{\mu-1}$.

The rate equation 4.13 used for modeling PIA experiments never really fits the high frequency behaviour. The reason can be the fact that at high frequencies the signal decreases with frequency and calculations are unstable as the integrand is oscillating too much. Hence, It seems reasonable that in the frequency domain we rarely observe an ω^{-1} decay. Like in the time-domain where we have a power-law decay rather than an exponential decay but usually something slower. The data in Fig. 4.18 (by Silva et al. [93]) shows the frequency dependence of the magnitude of the continuous PIA signal (R) in Polyindenofluorene (PIF) with n-octyl (PIFTO) at 290 K. [93] Fit to equation 4.13 as a continuous curve through the data shows that PIA signal turns over from steady state to off-steady state at lower frequency like $\omega^{-0.3}$. Note that the Fourier coefficients

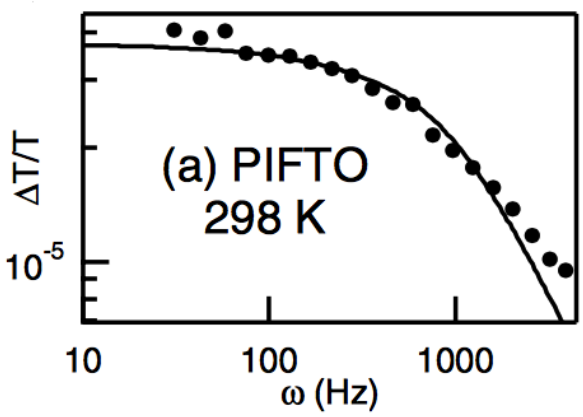

Figure 4.18 – Frequency dependence of the magnitude of the continuous PIA signal (R), with a fit to equation 4.13 [90] as a continuous curve through the data. Figure adopted from reference [93].

can be measured with a Lock-in amplifier. $X(\omega)$ is the signal in phase with the source whereas and $Y(\omega)$ is the signal out of phase (in-quadrature) with the source. The total PIA signal ($\frac{\Delta T}{T}$) is given by $R = \sqrt{X^2 + Y^2}/T$, ω is chopper modulation frequency.

4.7 Discussion/conclusion

Our results demonstrate the significant effects of ZnO-nanocrystals interface modification on the photovoltaic properties of hybrid photovoltaic cells composed of P3HT: ZnO heterostructures. We have reported photoinduced absorption measurements that were carried out at 10 K, a temperature in which charge transport is suppressed. Thus, under these conditions, we consider that the main effects on the observed quasi-steady-state charge kinetics involve geminate-charge recombination, which are predominantly local to the polymer:ZnO interface. We argue that these effects are relevant in the device, explaining the enhancement of photovoltaic properties upon interface modification. It is also possible, and indeed likely, that the solid-state microstructure of the film is altered by interface modification, such that charge transport processes can also play a role in explaining the device behaviour reported in this work. Nevertheless, the photoinduced absorption data at low temperature demonstrates substantial effects on average polaron lifetimes upon surface modification, and we base our discussion of our results on donor:acceptor interfacial consequences of surface modification with the interface modifiers used in this work.

4.7.1 Open circuit voltage and short circuit current

In this section we discuss how V_{oc} and J_{sc} play a significant role in the performance of hybrid P3HT: ZnO heterostructures. Introducing the dyes at the interface may contribute to the enhancement of the V_{oc} and photocurrent, as demonstrated here, and reported previously in the literature. [65, 67, 100] To explore how such enhancements would occur, we first focus on the alignment of the electronic energy levels in polymers and ZnO nanocrystals. Introducing the dye at the interface induces a dipole sheet between the donor and the acceptor which corresponds to a potential offset. [82] Therefore, the band-edge potential of ZnO shifts up or down depending on the dipoles orientation. Dipoles directed toward the acceptor (ZnO) shift the band-edge potential of ZnO away from the vacuum level of the donor (P3HT), resulting in reduction in both the effective bandgap between the conduction band minimum and HOMO, and V_{oc}. On

the other hand, dipoles pointing away from ZnO bring the band-edge potential of ZnO closer to the vacuum level of P3HT which increases both the interface bandgap and V_{oc}. We found that the V_{oc} of the device containing N3 additive increased by 0.12 V, whereas it is only increased by 0.03 eV in the 6TP-containing device. Hence, molecular interface modification contributes to reducing the defect density and traps at the ZnO surface. [80] As mentioned above, Goh et al. investigated the interface modification of bilayer P3HT:TiO_2 by using a series of *para*-substituted benzene carboxylic acids with varying dipole moments. [68] They found that the interface-modified cells only increased V_{oc} by at most $\sim$0.03–0.05 eV, with N3-added device displaying the lowest V_{oc}. [68] In our study, V_{oc} of the N3-containing device increased by $\sim$120 mV relative to the unmodified device. This might be due to differences in the nature of interactions between the carboxylic group and ZnO compared to TiO_2. In addition, we found that the V_{oc} of 6TP-added device is increased by $\sim$30 mV. Goh et al. concluded that the small increment in V_{oc} is possibly due to the opposite dipole contribution from protonation effects of carboxylic acid groups. [68] Since 6TP interacts with the ZnO surface via phosphonic acid and oligothiophene, the smaller increase in V_{oc} in the 6TP-containing device compared to the N3-containing device might be due to the opposite orientation of the dipole moment resulting from protonation. The smaller bandgap (CBM-HOMO) results in faster charge recombination, because it corresponds to the higher concentration of the electron in ZnO and hole in P3HT at a given voltage. [68] Therefore, slowing down of charge recombination is the significant result of increased V_{oc}. In addition, the obtained V_{oc} (0.54 eV) lies within the exciton binding energy of P3HT (0.4–0.7 eV), [80, 101–106] thus the increased V_{oc} affects exciton dissociation at the interface. N3 molecules posses a suitable LUMO level ($\sim$3.84 eV) that sits between the LUMO of P3HT ($\sim$3.0 eV) and conduction band minimum of ZnO ($\sim$4.40 eV) providing a possible energy cascade route for charge separation, while the LUMO level of 6TP ($\sim$3.84 eV) sits above the LUMO of P3HT. We therefore expect faster electron transfer through N3 to ZnO, which contributes to higher photocurrent. The 6TP-containing active layer showed the highest photocurrent, possibly suggesting a relatively small dye surface coverage on ZnO, with limited interference of electron transfer processes between P3HT and ZnO. In addition,

the larger electron affinity, and stronger electron-withdrawing of 6TP can account for the highest photocurrent. [68]

4.7.2 Polaron steady-state lifetime

Continuous-wave laser excitation reveals the generation of long-lived polarons. Sirringhaus et al. presented direct evidence of the polaronic nature of the charge carriers in P3HT by means of charge modulation spectroscopy in field-effect transistor architectures. [85] The photoinduced absorption spectra presented in Fig. 4.12 have the same lineshape as in the P3HT: ZnO film without additive, indicating that the electronic nature of polarons at steady state are not affected by the interface modifiers. This points to the role of surface dipole moments governing generation/recombination kinetics of polarons. Combination of pump modulation frequency dependent and pump intensity dependent PIA signal provides a way to determine an average lifetime for long-lived polarons. As compared to the previous measurements, Noone et al. studied the kinetics of nine donor-acceptor blends and found in general that polaron lifetimes are longer in polymers with inorganic acceptors as compared to when fullerene derivatives are used as acceptors. [98] This is rationalized by higher dielectric constants in environments containing inorganic acceptors, which contributes to screening of long-range Coulombic attractions between carriers. In addition, those author reported average lifetime of 2 ms for P3HT: ZnO. Our measurement of the polaron lifetime for P3HT: ZnO is significantly shorter than the 2 ms reported by Noone et al. [98] Noone et al. fitted the frequency dependent data to dispersive recombination model, in which the contributions of the unimolecular and bimolecular recombinations are indistinguishable. [98] We used a rate model in which the frequency dependent and power dependent data were treated via a global fitting, using single unimolecular and bimolecular recombination rate constants. We underline that it is not possible to introduce a specific lifetime that is independent of light intensity due to the fact that the PIA signal decays slowly at high modulation frequency ($\omega^{-\alpha}$ ($\alpha < 1$)). Therefore we limited the case to the average lifetime under the steady-state condition. [92] However, we note that the lifetime is dependent on the intensity because of bimolecular recombination.

CHAPTER 5

FORMATION OF A HIGHLY ORDERED RED PHASE IN A MEH-PPV : POLYSTYRENE GELS

5.1 Introduction

The main goal of this chapter is to identify a promising candidate (polymer) and the development of solution-based processing methods for opto-electronic applications. The application of quantum opto-electronic devices in both everyday life and advanced science would be widespread. However, the development of high-throughput quantum optoelectronics technologies has proven problematic, due to the absence of easily-scalable methods to process materials of the desired optical and morphological characteristics. In the present work, we address that problem by adopting a highly successful approach that will be employed in opto-electronics. That contributes to the explosion of a new scientific field, new technologies, and new products. Specifically, we propose to produce a step change for quantum optoelectronics applications through the employment of the gel-processed materials. For this purpose we processed ultra high molecular weight polystyrene (UHMW PS) gels, moreover by adopting steady-state spectroscopy tools such as absorption, photoluminescence and performing temperature-dependent photoluminescence measurements a promising candidate for opto-electronic applications has been identified.

The concept of present work was developed by the discovery of "Room-temperature Bose-Einstein condensation of cavity exciton-polaritons in a polymer". In 2014, Rainer F. Mahrt et al. successfully coupled the excitonic transition of a thin polymer film to the confined photon mode of a planar dielectric Fabry-Perot microcavity that led to the first demonstration of Bose-Einstein condensation at room temperature in organic materials [1] . [107]

The application of organic structures as optically active materials in microcavities

1. Bose-Einstein condensation can occur when the density of particles with integer spin is sufficiently high to allow for spatially overlapping wave functions of the individual particles. [107]

is interesting. Organic structures are classified as Frenkel excitons (discussed in chapter 2.1.2) due to their high binding energies [2] ($\sim$1 eV) compared to the thermal energy K_bT at room temperature, making these excitons highly stable at room temperature. Moreover, the large oscillator strength of the organic materials makes the use of organic microcavities more attractive. The strong coupling between the Frenkel excitons in organic materials and the cavity photons results in a Rabi splitting which is easily an order of magnitude greater than that of inorganic microcavities. [108]

In the work by Marht et al., the ladder-type conjugated polymer, called MeLPPP which features a relatively rigid backbone due to the methylene bridge between the phenyl rings is implemented in the cavity. Due to the associated low disorder of MeLPPP compared with other conjugated polymers, it exhibits a narrow, weak Stokes shift, inhomogeneously broadened exciton line widths -of the order of 60 meV- with spectrally resolved vibronic replicas even at room temperature that contributes to the strong coupling. That is the most fascinating aspect of polymers for opto-electronic applications. Fig. 5.1 illustrates the distributed bragg reflector (DBR) which contains the spin-cast polymer layer in the central anti-node of the optical field.

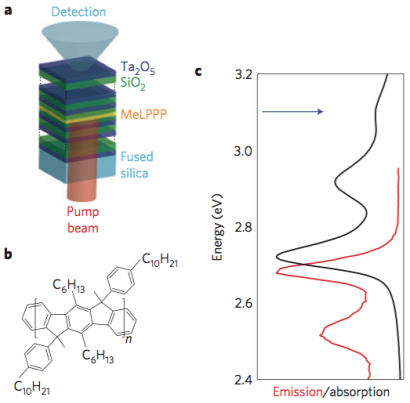

Figure 5.1 – (a) Illustration of the distributed Bragg reflector microcavity, (b) Chemical structure of the MeLPPP polymer and (c) Absorption (black line) and emission (red line) spectra of an MeLPPP film. The arrow indicates the excitation wavelength. Figure adopted from reference [107].

In short, conjugated polymers have proven to be potential candidates for opto-electronic applications however a promising candidate has still not been identified. This is primarily due to the intrinsic amorphous and disordered nature of spin-coated film.

2. The binding energy is the energy required to ionize the exciton into a free electron and hole.

Whereas MeLPPP is not easy to process especially at high molecular weight. Hence, this work aims at identifying a readily processable material for opto-electronic applications.

5.2 Characteristics of a promising candidate

As discussed in chapter 2.2.4 polymers with high molecular weight can undergo H- to J-type transformation. The hybrid (HJ) behaviour is dependent on variety of factors - such as different processing conditions, solvent additives, etc. just to name a few - that give rise to different morphologies. Fig. 5.2 shows the absorption and PL spectra of a P3HT film cast from chloroform and that of nanofibers grown in toluene.

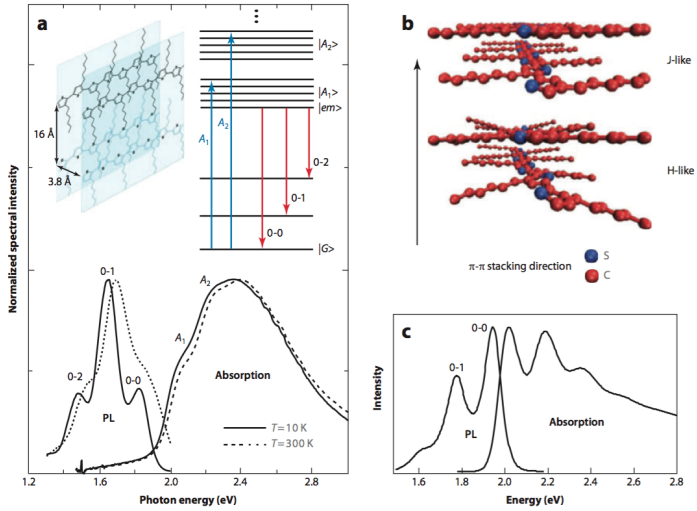

Figure 5.2 – (a) Absorption and photoluminescence (PL) spectra of a P3HT film cast from chloroform. (Insets) P3HT π-stack and Jablonski diagram corresponding to a weakly coupled H-aggregate model. (b) Graphical depiction of J- and H-aggregates of P3HT. (c) Absorption and PL spectra of P3HT nanofibers grown in toluene.Figure adopted from references [24, 29, 31].

The vibronic progression in the absorption spectra of P3HT nanofibers at room temperature is more pronounced than that of the spin-coated P3HT at low temperatures. P3HT nanofibers which self assemble in a slowly cooled toluene solution, show that the ratio of the $0-0$ to $0-1$ PL peaks can be greater than one at room temperature, which is

higher than that predicted from the H-aggregate model (less than one). [109] Therefore the nanofibers display J-like emission behaviour in contrast to the H-like behaviour of thin films. In fact conjugated polymer films exhibit morphology-dependent J- or H-like properties that is associated with a delicate interplay of intra- and intermolecular interactions. [110] Due to the very high oscillator strength and consequent optical properties a J-aggregated polymer serves as a good candidate for room temperature-strong coupling applications. Based on the similarities between the PL spectrum of P3HT nanofibers and that of MeLPPP, it is concluded that the polymer of our interest for use in quantum optoelectronics devices should be a J-aggregated polymer.

5.3 MEH-PPV: poly [2-methoxy, 5-(2'-ethyl-hexoxy)-1,4-phenylene vinylene]

The derivatives of Poly (para-phenylenevinylene) (PPV) such as MEH-PPV, and its oligomers are of interest for applications in electronic devices such as photovoltaics, transistors, and organic light-emitting diodes (OLEDs) as well as quantum optoelectronic application. A type of morphological phenomenon in conjugated polymers of PPV family is known as polychromism, that has strong impact on the performance of devices such as transistors, photovoltaic cells or light-emitting diodes based on these materials. [111] "Polychromism is of scientific interest as it indicates changes in the underlying electronic structure, and it has strong potential for commercial applications". For example, the temperature-dependence of absorption and emission in derivatives of polydiacetylene is being considered for sensor applications. [111] Depending on the solvent, concentration and temperature, photoluminescence occurs either from a high energy state (the blue phase) or from a lower energy state (the red phase) that differs in the extent of delocalisation of the π-bond electrons. köhler et al. show the evidence of two morphologically distinct species in their recent work that when MEH-PPV chains dissolved in a polar solvent (methyltetrahydrofuran (Me-THF)) undergo a conformation transition from coil- to chain-extended-conformation at about 200 K. This conformation transition is assigned to the blue to red phase transition respectively. [111, 112] Fig. 5.3 shows the absorption and emission spectra of MEH-PPV in MeTHF (5×10^{-6} mol/l)

within a temperature range of $290 - 110$ K. The PL spectrum consists of emission from the blue phase with a $0 - 0$ PL peak intensity at about 2.20 eV and a red phase with a $0 - 0$ PL peak intensity at about 2.07 eV. Upon cooling, the intensity of the emission from the blue phase reduces while that of the red phase grows. Moreover, the PL spectrum at

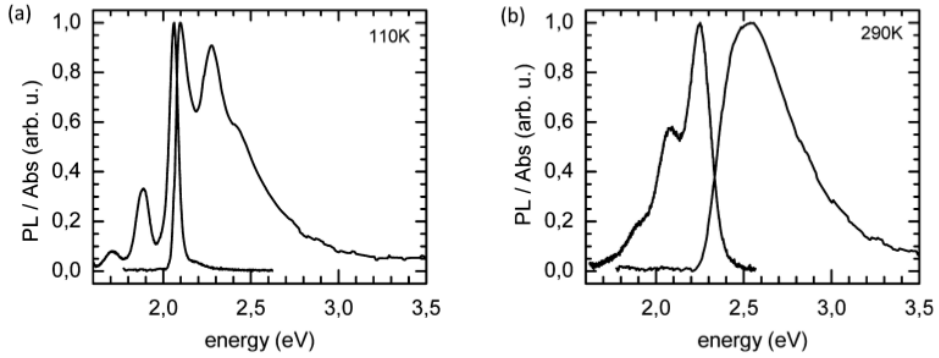

Figure 5.3 – The absorption and emission spectra of MEH-PPV obtained in 5×10^{-6} M MeTHF (a) at 110 K, where the red phase dominates, and (b) at 290 K, where the blue phase dominates. Figure adopted from reference [112].

110 K, demonstrates a significant enhancement of the vibronic progression that is due to the enhanced intrachain order at low temperature and the characteristic of a J-aggregated polymer. [16] The $0 - 0$ PL peak intensity in the absorption spectrum is also enhanced with respect to the first side band at low temperature.

Whilst the conformation transition occurs in the solution, the flow and evaporation of liquids result in seals being dissolved and broken. In addition, the red-phase of MEH-PPV has only been observed in the solution and there has not been any successful effort to obtain this super-interesting behaviour in thin film of MEH-PPV. This indicates that the degree of aggregation in solution does not necessarily translate into the film. This limits the extend of usage of MEH-PPV polymer in devices. As such, understanding the nature of the optically excited states of the films is vital to the development of devices. This work is concerned with addressing the question of whether our understanding of fundamental (solution) photophysics can be extended to the function of such materials in solid matrix. This issue is of particular importance for the development of quantum optoelectronics devices, which will typically incorporate a thin film of the polymer rather

than a solution. The significance of this work is to create solid-like materials to involve MEH-PPV into a polymeric host matrix, which serves as a mechanical support for the chromophores. It has been found that material with a low glass-transition temperature is desirable for use as a solid-like host matrix. [113] What is desirable is a material that is "microscopically liquid whilst macroscopically solid", termed as gel [113] such that it takes advantage of both phases in the relevant spatial domains, and that the macroscopic viscosity of the gel does not cause any photochemical reaction . Here we show that efficiencies indistinguishable from the solution phase can be obtained in a gel as a liquid trapped through numerous microscopic interconnected domains. A gel is a macroscopically highly viscous substance that will retain its shape and fail to flow when inverted. The structure of a physical gel is ideal because it is a macroscopically solid material with a high volume fraction of interstitial space occupied by the solvent, permitting unimpeded diffusion of the active materials between the entanglements. [113]

In order to process the red-phase gel to emulate the film and introduce red-phase of MEH-PPV, we process a gelation agent with ultra high molecular weight polystyrene polymer that is transparent to the visible light, hence indistinguishable in the photophysical measurements from the liquid sample.

In what follows, we explain our processing protocols. I have partly worked on this project in Prof. Natalie Stingelin group (department of materials, Imperial College London) where I spent four months to learn about material processing and processing protocols of polystyrene gel with Dr. Jaime Martin. I further explored the project by supplementary spectroscopic measurements in our group.

5.4 Processing protocols for MEH-PPV / ultra high molecular weight polystyrene gels

Polymers are long chain molecules that comprise covalently connected moieties that interact through relatively weak intermolecular forces. Increasing polymer chain length (molecular weight) gives rise to increasing the (melt) viscosity due to sterical hindrance and reduced mobility of the longer chain molecules. Ultra-high molecular

weight (UHMW) polymers refers to macromolecules with molecular weights that exceed 10^6 g/mol. [114] Polystyrene (PS) is a rigid, transparent thermoplastic, which exists in solid or glassy state at room temperature and belongs to the family of Vinyl Polymers. The structural units of PS is shown in Fig. 5.4. In order to produce the gel which

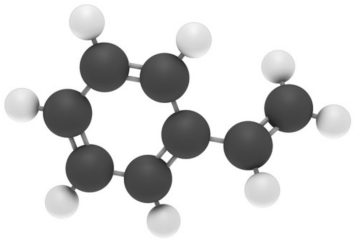

Figure 5.4 – The structural units of polystyrene, Carbon in black and Hydrogen in white. Figure adopted from reference [114].

consists of ultra high molecular weight polystyrene (UHMWPS) as the organogelator, 2-Methyltetrahydrofuran (Me-THF) as the solvent, and MEH-PPV as the active material, the following procedures were used.

5.4.1 Preparation of ultra high molecular weight polystyrene solution

In this work, the ultra high molecular weight polystyrene (30×10^6 g/mol) with molecular weight per repeat unit ($M_{r.u.}$) of 104.1 g/mol (purchased from Polyscience Inc.), has been used as the organogelator for MEH-PPV polymer.

The first goal was to find the minimum concentration at which the polystyrene solution undergoes a transition from liquid to gel. To achieve this goal, first 10, 15, 30, 50, and 100 mg of polystyrene powder were weighted in separate vials, dissolved in 900 μl of Me-THF solvent and stirred for 5-10 minutes on a hot plate at a temperature of 80 °C, using a heating block for well-defined dissolution temperature. After which the solutions were heated at a temperature of 58 °C (below the boiling point of MeTHF *i.e.* 80 °C) for up to one hour - depending on the polystyrene weight fraction - until the solutions were homogenous. The heat was subsequently turned off and the solutions were cooled to room temperature. Upon cooling the solutions to room temperature, the solution undergoes a thermo-reversible transition from liquid to gel. Using liquid nitrogen (N2), the gels were then rapidly cooled to $\sim$ 70 K. This process was repeated several times. Note that the solution which contained minimum solute (10 mg of polystyrene), did not ap-

pear to form a gel. Hence, the lowest concentration of this polystyrene required for the transition from a liquid to a gel is estimated to be 15 mg/ml. As such the polystyrene gel at different weight fractions (wt%1.5, 3.0, 5.0, and 10.0) of polystyrene with respect to the total weight of the gels were ready. The gelation mechanism relies on the nucleation and crystallization of the UHMW PS within the blend. This crystallization process forms high aspect-ratio nano- and microscopic features of UHMW PS that entangle, producing interactions that cooperatively inhibit macroscopic rotation/translation and result in the formation of a physical gel. [113] Alternatively it is also possible to sonicate the solute after heating it to 58 °C, followed by the same procedure as above. The first gels were prepared using this method. The mole percent of these solutions is shown in table 5.I

Polystyrene / Me-THF		
Concentration(mg/ml)	wt.%	(mole percent%)$\times 10^{-3}$
15	1.5	0.15
30	3	0.3
50	5	0.50
100	10	1.03

Table 5.I – Weight and mole percent of the Polystyrene solution.

5.4.2 Preparation of MEH-PPV solution

Similarly, in order to make the MEH-PPV solution of 5.0×10^{-3} M, first 3 mg of MEH-PPV powder was weighted in a vial and then dissolved in 2 ml of Me-THF solvent which was stirred for 5-10 minutes on a hot plate at 120 °C using the heating block for well-defined dissolution temperature. After which the solution was diluted to 5.0×10^{-4} M, by adding 900 μl of Me-THF to the 100 μl of the solution. Table 5.II. tabulates the mole percent of the MEH-PPV with respect to the total mole of the solution.

MEH-PPV / Me-THF		
Molarity (M)	wt.%	mole percent%
5.0×10^{-5} M	1.61×10^{-4}	0.62×10^{-5}
5.0×10^{-4} M	1.61×10^{-3}	0.62×10^{-4}

Table 5.II – Molarity of MEH-PPV solution.

5.4.3 Ultra high molecular weight polystyrene / MEH-PPV gels

MEH-PPV / UHMW PS gels at two different molarities of MEH-PPV solution were prepared, by introducing 100 μl of 5.0×10^{-3} M and 5.0×10^{-4} M MEH-PPV solution into the polystyrene gel. The MEH-PPV/UHMW PS gels were heated at 50 °C until the MEH-PPV solutions were thoroughly mixed to obtain the desired homogenous gels. Characteristics of different gels are summarised in table 5.III. Note that the mole percent of the MEH-PPV solution (for instance 3.5×10^{-3}%) in the total gel is insignificant compared to the mole percent of the Polystyrene solution in the total gel (99.9965%).

Polystyrene	MEH-PPV	MEH-PPV / Polystyrene gels
Concentration(mg/ml)	Molarity (M)	(mole percent%)$\times 10^{-3}$
15 mg/ml	5.0×10^{-5} M	3.5
30 mg/ml	5.0×10^{-5} M	1.7
50 mg/ml	5.0×10^{-5} M	1.04
50 mg/ml	5.0×10^{-4} M	1.04
100 mg/ml	5.0×10^{-5} M	0.52

Table 5.III – Characteristics of different gels.

Fig.5.5 illustrates photographs of the MEH-PPV/UHMW PS gels for three different concentrations of PS solution (1.5, 3.0, and 5.0 wt.%) with 5.0×10^{-6} M MEH-PPV solution that were subject to a fast cooling rate. Because the MEH-PPV solution is too

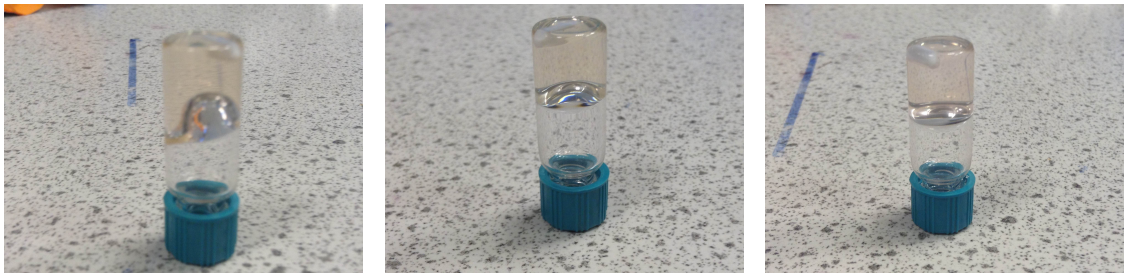

Figure 5.5 – 15 mg/ml, 30 mg/ml, 50 mg/ml UHMW PS solution containing 5.0×10^{-6} M MEH-PPV.

dilute the colour of the gel is pale. The pictures were taken 5 minutes after the vials were held upside down and the gels did not flow downwards. The gels were sent to Spain, Institute of polymer science and technology of CSIC, for rheology tests.

5.4.4 Rheology tests on the UHMW PS gels

In this section the basis of the rheology tests is discussed shortly. Fluid materials, by definition, are systems which flow when subject to stress. [115] The rheological test defines how the fluids respond to an input stress. Structured fluids often will not flow unless they have reached a critical stress level, known as the yield stress, below which a material is "fully" elastic and above it the structure of the material breaks and flows. The yield stress is the stress at which the viscosity is maximum. The rheological properties of a viscoelastic material are independent of strain up to a critical strain level. Beyond this critical strain level, the material's behaviour is non-linear and the storage modulus declines. So, measuring the strain amplitude dependence of the storage and loss moduli [3] (G', G'') is a good first step for characterisation of visco-elastic behaviour. G'>G'', indicates that the material is highly structured. Increasing the strain above the critical strain disrupts the network structure. After the fluid's linear viscoelastic region has been defined by a strain sweep, its structure can be further characterised using a frequency sweep at a strain below the critical strain. In a frequency sweep, measurements are made over a range of oscillation frequencies at a constant oscillation amplitude and temperature. Below the critical strain, the elastic modulus $G'$is often nearly independent of frequency, as would be expected from a structured or a solid-like material. The more frequency dependent the elastic modulus is, the more fluid-like is the material.

The MEH-PPV/ UHMW PS gels were sent to Institute of polymer science and technology of Spanish National Research Council [4] for rheology tests. Fig. 5.6 shows frequency sweep carried out by a rheometer AR-G2 with parallel plates of 40 mm diameter, at a constant temperature of 10 °C and using a deformation of 10%. The storage G' modulus (in red - left axis) and the loss modulus G'' (in blue - right axis) are plotted as a function of frequency, with open and filled circles corresponding to wt% 6.0 and wt% 3.0 respectively. According to the frequency sweep done in the two samples, it is clear

3. The storage modulus measures the stored energy which represents the elastic portion, loss modulus in viscoelastic materials measures the energy which is dissipated as heat, representing the viscous portion. [115]

4. Consejo Superior de Investigaciones Científicas

that G'>G'' in both samples, as expected for a solid-like material. Moreover, the results demonstrates that the elastic modulus G'' is nearly independent of frequency, and G' is frequency dependent. This behaviour is more evident for the sample which has lower polystyrene concentration, because it shows a terminal region at low frequencies where G' and G'' decrease with frequency. As such it is concluded that the samples are highly viscous liquids.

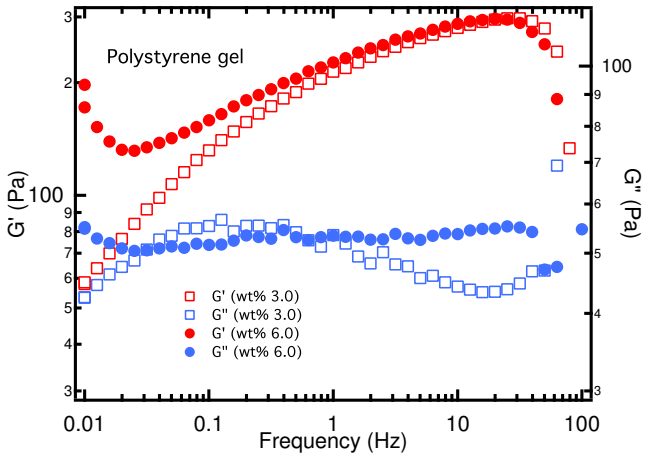

Figure 5.6 – Frequency sweep on the UHMW PS solution (wt% 3.0 and 6.0). The log-log plot of elastic moduli G' in red (left axis) and G'' in blue (right axis) as a function of frequency, open squares corresponded to wt% 3.0 and filled circles corresponded to wt% 6.0 respectively. Measurements taken at Institute of polymer science and technology of CSIC.

5.5 Theoretical models for data analysis

5.5.1 Franck-Condon analysis of PL spectra

In the prior work by Yamagata et al. on red-phase MEH-PPV solution, the authors applied the concept of HJ-aggregates, due to the fact that the $0-0/0-1$ PL line-strength ratio is substantially larger at low temperatures, exactly opposite to what is found in spin-cast P3HT aggregates, and defying the predictions of the simple H-aggregate model discussed in chapter 2.2.3. [112]

On closer investigation, we explore the dependence of steady-state PL peak intensity with temperature based on what performed by Yamagata et al. [112] For analysis of the PL spectrum, the ratio between the intensity of the $0-0$ and $0-1$ peaks in the PL spectrum needs to be known precisely. Further information can be obtained from the corresponding PL spectra. In order to examine these trends more quantitatively we analysed the PL spectra of MEH-PPV/UHMW PS gels in a range of temperatures to extract the $0-0/0-1$ PL line-strength ratio, Huang-Rhys parameter, electronic transition peak energy (E_{0-0}), and the Gaussian line width via a fit with Franck-Condon model in which the PL spectrum is modelled as $\bar{S}(\hbar\omega)$

$$\bar{S}(\hbar\omega) = n^3 (\hbar\omega)^3 \sum_{m_i} \prod_i I_{0\to m_i} \times \Gamma \left[\hbar\omega - \left(\hbar\omega_{0-0} - \sum_i m_i \hbar\omega_i \right) \right], \tag{5.1}$$

where n is the refractive index of the material at the optical frequency ω, ω_i is the frequency of the ith mode, m_i= 0,1,2,. . . is the number of vibrational quanta in the ith mode, and the set of integers m_i identifies a particular combination peak. $\hbar\omega_{0-0}$ is the $0-0$ peak energy. Γ is a Gaussian line shape function with constant standard deviation σ that represents the inhomogeneously broadened spectral line of the vibronic replica in the progression. $\hbar\omega_i$ is the energy of the effective oscillator coupled to the electronic transition (the most strongly coupled mode (or cluster of modes) corresponds to the high frequency vinyl-stretching mode), $\sim 0.174\,\mathrm{eV}$ for most of the polymeric semiconductors. [34, 112] Hence, according to the Franck-Condon principle, the intensities of the vibronic peaks are expressed with a Poisson distribution given by

$$I_{0-m_i} = e^{-\lambda_i^2} \lambda_i^{2m_i} / m_i!. \tag{5.2}$$

The Huang-Rhys factor can be determined experimentally by taking the ratio between the intensities of the vibronic progression *i.e.* $0-2$ and $0-1$ of the PL spectrum [34] given by

$$\lambda^2 = 2 \frac{I_{PL}^{0-2}}{I_{PL}^{0-1}}. \tag{5.3}$$

5.5.2 Optical properties of "HJ" hybrid aggregates

The "HJ" hybrid model developed by Yamagata and Spano (chapter 2.2.3.1) that takes in to account the competition between the intra- inter-chain interactions can assist in interpreting the absorption and PL spectra of aggregated polymers. [15] Based on this model, in the conformation with a cofacial arrangement, the exciton is delocalised not only along the chain but also in the direction of the stacks. Fig. 5.7 clearly shows the excitonic dispersion of J- and H-aggregate (a,b) versus HJ-aggregate (c). The black dot indicates the exciton in ground state ($|G\rangle$) while the red dot indicates the optically allowed $k = 0$ exciton to the excited state. The energies of the one- and two-phonon states within the electronic ground state are also indicated.

Section 2.2.1 discussed that in a J-aggregate ($J_0 < 0$) the symmetric band is the bottom band whilst in an H-aggregate ($J_0 > 0$) the symmetric band is the top band. Photoluminescence (PL) is mainly caused by band bottom excitons [5], as shown in Fig. 5.7 a and b, the band bottom exciton in a J-aggregate is $k = 0$ whereas in an H-aggregate it is $k = \pi$, hence we expect to observe differences between the PL spectra of H- and J-aggregates. When temperature is zero ($T = 0\,\mathrm{K}$) also in the absence of disorder, in a J-aggregate the $0-0$ PL peak intensity is enhanced because $0-0$ is the only state that makes transition from the excited state to the vibrationless ground state. On the other hand, in an H-aggregatethe the $0-0$ PL peak intensity is attenuated because the excitation band bottom is $k = \pi$ therefore, a transition from $k = \pi$ to $k = 0$ (ground state) breaks conservation of momentum and is forbidden by symmetry. When temperature increases, thermal effect populates other excited states than ($k = 0$), thus $k = 0$ state is no longer the only state that makes transition in a J-aggregate and becomes less probable. Moreover, disorder is not negligible and it mixes different states such that k is no longer well-defined. It is concluded that increasing the temperature and presence of disorder, reduce the $0-0$ PL peak intensity in a J-aggregate. Conversely, in the H-aggregate, as temperature elevates the $k = 0$ state at the top of the exciton band is thermally populated such that the $0-0$ peak grows with increasing temperature.

5. After photo-excitation occurs, a rapid through-bond reorganization causes the chromophore to lose its excess energy and reach the bottom of the excitation band (Kasha's rule [116])

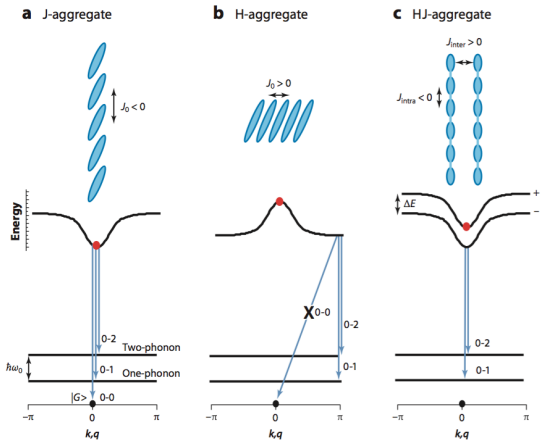

Figure 5.7 – (a,b) Molecular orientations within conventional J- and H-aggregates. The sign of the nearest-neighbor coupling $J_0 < 0$ is associated with a head-to-tail orientations (J-aggregation), whereas $J_0 > 0$ is associated with side-by-side orientations (H-aggregation). (c) In polymer HJ-aggregates, Coulombic interchain coupling is positive ($J_{inter} > 0$), whereas the effective intrachain coupling between adjacent repeat units is negative ($J_{intra} < 0$) due to the through-bond interactions in 1D direct band-gap semiconductors. The black dot indicates exciton in ground state ($|G\rangle$) while the red dot illustrates the optically allowed $k = 0$ exciton in the excited state. The energies of the one- and two-phonon states within the electronic ground state are also indicated. Intramolecular vibrations contributes to the dispersionless (Einstein) phonons of wave vector q and frequency ω_0. In the HJ-dimer, the J-like intrachain band in each polymer is split into symmetric (+) and antisymmetric (-) bands by interchain interactions. Selection rules, allows only the $k = 0$ symmetric state to be coupled to $|G\rangle$. Hence, in HJ-aggregates, as well as H-aggregates, $0-0$ emission is thermally activated. Note that Arrows indicate emission pathways at low temperatures and higher bands in $E(k)$ are omitted for clarity. Figure adopted from reference [29].

Fig. 5.7 c shows the "HJ" excitonic dispersion where the symmetric band (the top) and the anti-symmetric band (the bottom) are split by interchain coupling (ΔE_{inter}). According to the "HJ" hybrid model a conjugated polymer dimer cannot generally be described as an H- or J-aggregate. The $0-0$ PL peak intensity of a hybrid "HJ" in the presence of the temperature is different than that of in either a J- or an H-aggregate. When temperature increases the $0-0$ PL peak intensity initially increases and turns over where k_bT is approximately equal to the interchain splitting $= \Delta E_{inter}$. As shown in Fig. 5.7 c, in a dimer the lowest energy exciton is anti-symmetric, there is thus no $0-0$

component at $T = 0\,\mathrm{K}$. Given that the only states which can provide $0-0$ emission are symmetric bands, thermal activation is required to populate the symmetric band (the top band in Fig.5.7 c). [16] Hence, the photophysics of such materials is strongly dependent on the interplay between the intrachain (through bond) and interchain (through space) interaction that allows the exciton motion along the backbone of the molecule (through bond) and between the cofacial arrangement (through space).

5.5.3 Exciton coherence

When an exciton is delocalised coherently over a length L_C within its aggregate, the exciton wave function is conserved over L_C. As such development of a large coherence length is highly desired since lack of coherence is mainly caused by disorder. [16] The coherence length for the band bottom (emitting) exciton is calculated from the exciton coherence function given by [24]

$$C^{em}(s) \equiv \sum_{n} \left\langle \psi^{em} \left| B_n^{\dagger} B_{n+s} \right| \psi^{em} \right\rangle \qquad s = 0 \pm 1, \pm 2..., N/2, \tag{5.4}$$

where $B_n^{\dagger} \equiv |n;vac\rangle \langle g;vac|$ and the *vac* stands for vibration-less electronic ground state (vacuum state). $T = 0\,\mathrm{K}$ and *s*=0 cause the coherence function to be entirely delocalised over both H- and J-aggregates. The amplitude $\langle C^{em}(s=0)\rangle_c$ contains information about the extent of the nuclear relaxation at the site of the vibronic excitation. [24] In the weak coupling regime where $W \ll \lambda^2\omega_0$ $\langle C^{em}(0)\rangle_c$ reduces to $\exp\left(-\lambda^2\right)$ and is independent of disorder. However, it should be noted that presence of disorder can enhance the vibronic relaxation of the emitting exciton. An important relationship between the coherence function and the $0-0$ line strength is given by

$$N_{coh} \equiv \frac{1}{\langle C^{em}(s=0)\rangle_{T,c}} \sum_{s} \left| \langle C^{em}(s)\rangle_{T,c} \right|. \tag{5.5}$$

In a linear aggregate the coherence length is given by,

$$L_c = (N_{coh} - 1)\, d, \tag{5.6}$$

where d is the distance between nearest-neighbour chromophores. The coherence number at $T = 0\,\mathrm{K}$ in aggregates with no disorder is $N_{coh} = N$ which corresponds to $L_c = (N_{coh} - 1)\,d$. As temperature rises (and/or disorder increases) the exciton becomes more localised until it becomes completely localised at $N_{coh} = 1$, or $L_c = 0$. This behaviour is therefore similar to the PL intensity ratio, $0-0/0-1$, in J-aggregates such that the ratio decreases as the temperature rises (and/or disorder increases) which is different from the H-aggregates in which the $0-0/0-1$ increases with increasing temperature (and/or disorder increases). [16] Therefor the coherence length in a J-aggregate, not covered by the details of calculation, is simply given by

$$\frac{I_{0-0}}{I_{0-1}} = \kappa \frac{N_{coh}}{\lambda^2}, \tag{5.7}$$

where κ is a prefactor close to unity. [16]

5.6 Is the MEH-PPV red-phase retained in the UHMW PS matrix?

In what follows, we investigate the red-phase of MEH-PPV in our processed UHMW PS matrix through the investigation of photophysics properties of MEH-PPV/UHMW PS gels by means of linear absorption and temperature-dependent PL spectroscopy. First we go over the previous works on MEH-PPV, that show different results.

Zeng et al. measured the PL and Raman spectra of thin film of PPV using dichloro-p-xylene and tetranhydronthionphene in the temperature range from 83 K to 293 K. The authors observed no significant shift in the Raman band frequency nor in the PL and they measured the emission energy shift for the $0-0$ electronic transition to be only 6 meV. The authors also found that the conjugated length is elongated by 2.2 repeat units from 294 to 83 K and assigned it to the reduced disorder at low temperatures. [117]

Wantz et al. measured electroluminescence of thin film of PPV derivative (BDMO-PPV) in the temperature range of 80-350 K. The authors found that energy separation (between pure electronic transition $0-0$ and first vibronic transition $0-1$) was temperature independent. The authors also carried out temperature dependent PL measurement of MEH-PPV and found that $0-0$ pure electronic transition blue-shifted about 60 meV

(as temperature increased). Moreover, the Huang-Rhys factor was found to be temperature independent hence Wantz et al. could not assign the blue-shift in the $0-0$ PL peak to a reduced conjugation length in the thin film of PPV derivative. [118]

In the work of Silva et al. temperature-dependent PL spectra of thin film MEH-PPV deposited by spin coating on a copper substrate was studied. The authors showed that $0-0$ pure electronic transition blueshifted about 60 meV between 13-297 K. Moreover, Silva et al. found that I_{0-1}/I_{0-0} increased as temperature increased and attributed that to the decrease of conjugation length. [119]

Following the work by Köhler et al. that demonstrated a conformation transition of MEH-PPV in MeTHF, [111] Yamagata et al. reported a very comprehensive experimental work along with numerical calculation on the MEH-PPV in MeTHF. Yamagata et al. proposed that the "HJ" hybrid model contributes greatly to the understanding of the basic photophysical features observed for red-phase MEH-PPV. Yamagata et al. concluded that J-like behaviour is favored by a relatively large intrachain exciton bandwidth- roughly an order of magnitude greater than the interchain bandwidth- and the presence of disorder. [112] Here we discuss the red-phase of the MEH-PPV/UHMW PS gels by weakly coupled HJ-aggregates in which the interchain splitting, ΔE_{inter}, is roughly an order of magnitude smaller than the $0-0$ intrachain exciton bandwidth, ΔE_{intra}. [15, 112]

5.6.1 The red-phase MEH-PPV in MeTHF solution

We begin with a brief discussion of the PL spectrum of MEH-PPV solution along with its absorption. Absorption and PL spectra were taken from MEH-PPV (M_W=60 KD) in MeTHF at a concentration of 5×10^{-5} mol/l (using the home-built setup explained in chapter 3.2). A fused silica cuvette with 1 mm optical path length was used for solution measurements; the excitation wavelength was 405 nm ($\sim$ 3.0 eV) for PL measurements. Fig. 5.8 shows the absorption and emission spectra for MEH-PPV in MeTHF at 290 K, in disordered phase where the polymer chain is coiled, and at 80 K, in ordered phase where the extended chain dominates. At 80 K one can clearly see features corresponding to the J-aggregate in the PL spectrum that will be precisely analysed later. The $0-1$ peak in PL spectrum centered on 1.85 eV is much lower in intensity than the corresponding peak

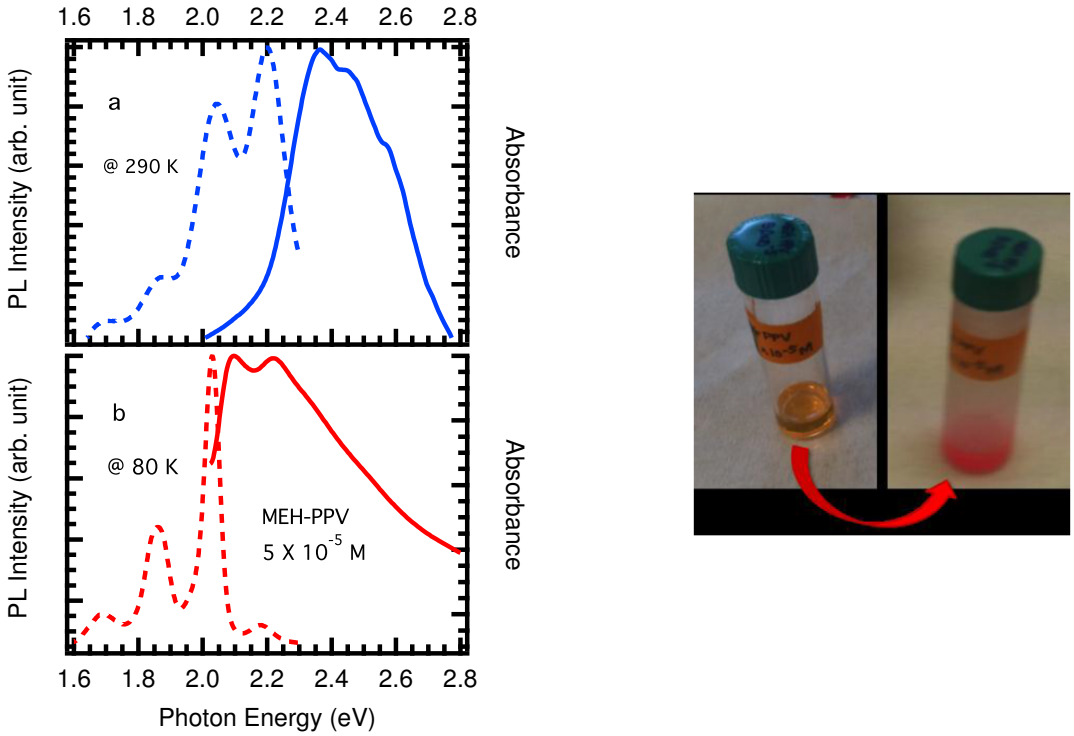

Figure 5.8 – Left: comparison of the absorption and emission spectra of MEH-PPV obtained in 5.0×10^{-5} M MeTHF solution (a) at 290 K, where the blue phase dominates, and (b) at 80 K, where the red phase dominates. Right: The solution before and after PL measurements.

at about 2.15 eV. Note that at 290 K, the shapes are more comparable in the absorption and PL spectra. Upon cooling, the blue phase with the $0-0$ peak at about 2.20 eV turns to a red phase with a $0-0$ peak at about 2.06 eV. Here we showed that the result is consistent with Köhler results for MEH-PPV in MeTHF solution, however, the molarity is one order of magnitude higher than the reference. [111] Moreover, the polychromism is clearly shown in Fig. 5.8 (right) which corresponds to different electronic structure.

5.6.2 The red-phase MEH-PPV/ UHMW PS gels

The goal of this section is to demonstrate the highly red-phase of MEH-PPV/ UHMWPS gels as an interesting feature with introducing it into our gel. So far we have demonstrated how the gels were processed and reproduced the red-phase of MEH-PPV

in MeTHF solution and how the temperature plays a significant role in the formation of chain-extended MEH-PPV in MeTHF solution. Now we report on the photophysical properties of the MEH-PPV/ UHMW PS gels as a function of temperature, covering a temperature ranging from 290 K down to 80 K. Absorption and PL spectra were taken from MEH-PPV/ UHMW PS gels. MEH-PPV in MeTHF solution at a concentration of 5×10^{-5} mol/l (M_W=60 KD) and PS in MeTHF solution at a concentration of 30 mg/ml (wt% 3.0 & M_W=30000 KD).

A: absorption versus PL spectra of MEH-PPV/ UHMW PS gels: In Fig. 5.9 the absorption spectra at 80 K and 290 K show that the spectrum is red-shifted from 2.42 eV to 2.1 eV with narrower bandwidth going from 80K to 290 K. In addition the

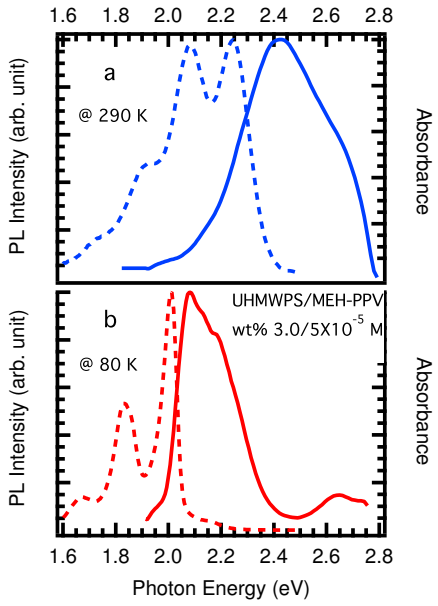

Figure 5.9 – Comparison of the absorption and emission spectra of MEH-PPV/ UHMW PS gels obtained in PS wt% 3.0 solution containing 5.0×10^{-5} M (a) at 290 K, where the blue phase dominates, and (b) at 80 K, where the red phase dominates.

$0-0$ (2.1 eV) peak is dominant over the $0-1$ (2.2 eV). The PL spectra shows narrower line width with enhanced $0-0$ peak width at 80 K compared to 290 K. The absorption spectrum consists of a dominant $0-0$ peak at 2.1 eV and its first side band $0-1$ peak at 2.2 eV. The ratio of the oscillator strengths of the $0-0$ and $0-1$ peaks, R_{abs} $\equiv I_{0-0}/I_{0-1}$, is 1.25, consistent with R_{abs} of MEH-PPV solution reported by Yamagata et al. [112]. When the gel is cooled the Stokes shift between the PL and the absorp-

tion shrinks (~ 67 meV) compared to that of at 290 K. When the absorption and the PL originate roughly from the same energy band, they undergo a small Stokes shift and characterises J-aggregate behaviour. Given the fact that in a J-aggregate, upon the absorption of a photon excitons reside at the bottom of the band ($\kappa = 0$ state) therefore it emit from $\kappa = 0$ state hence a small Stokes shift is expected. In the PL spectra of the gel shown in Fig. 5.9 the $0-0$ PL peak intensity corresponds to pure electronic transition as well as the first $(0-1)$ and second $(0-2)$ vibronic progression bands are clear at low temperature.

B: PL spectra in the cooling and heating half-cycles: Fig. 5.10 a and b show the cooling half-cycle versus heating half-cycle of PL measurements respectively. The

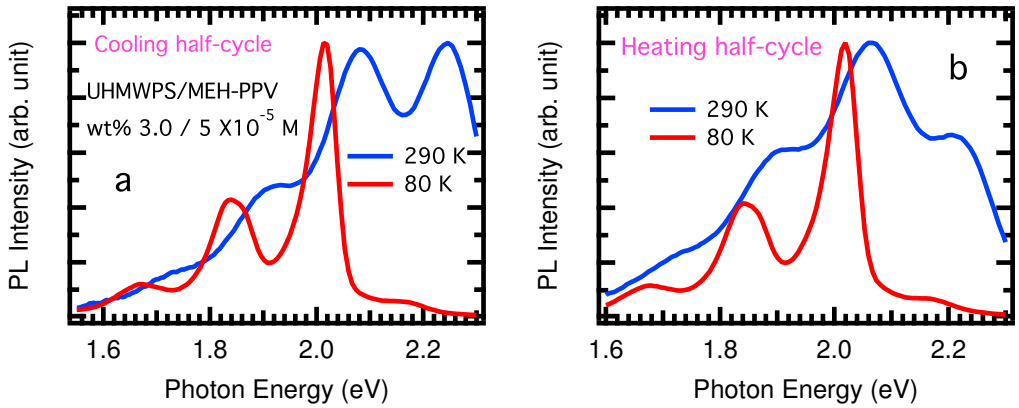

Figure 5.10 – a: PL spectra at 290 K where the blue phase dominates and at 80 K where the red phase dominates in the cooling half-cycle, b: PL spectra at 290 K where the blue phase dominates and at 80 K where the red phase dominates in the heating half-cycle.

feature of PL spectrum at 290 K in the cooling half-cycle demonstrates that the intensity of $0-0$ band is nearly equal to that of $0-1$ peak. This favours an isolated molecule with identical $0-0$ and $0-1$ line strengths. [16] The single-molecule-like behaviour of the spectrum in Fig. 5.10 results from an enhanced like-lihood that the offset difference between neighbouring molecules is much larger than the excitonic coupling, J_0. [29] In marked contrast, at low temperature the $0-0$ peak is enhanced compared to the $0-1$, with the $0-0/0-1$ PL line-strength ratio greater than unity; this is the signature of J-aggregate-like behaviour. On the other hand, the heating half-cycle shows that by

increasing the temperature to 290 K the spectrum demonstrates the evidence of a H-aggregate-like behaviour due to the suppressed $0-0/0-1$ PL line strength ratio to less than unity.

In the red-phase spectrum there is evidence of a small peak at 2.2 eV, this peak can be assigned to some polymer segments remaining in the non-extended phase. That could be expected since some parts of the MEH-PPV chains must be entailed with the UHMW PS. Therefore, the MEHPPV chains must be bended in those entanglements and thus the red phase segments cannot form at these points. It is important to note that by replicating the cooling half-cycle the red-phase and the J-like spectrum is retrieved.

Fig. 5.11 shows the shift of the PL spectrum towards the lower energy states known as red-phase transition; the left and the right panels correspond to the cooling and heating of the sample respectively. It is therefor possible to give a closer look at the tempera-

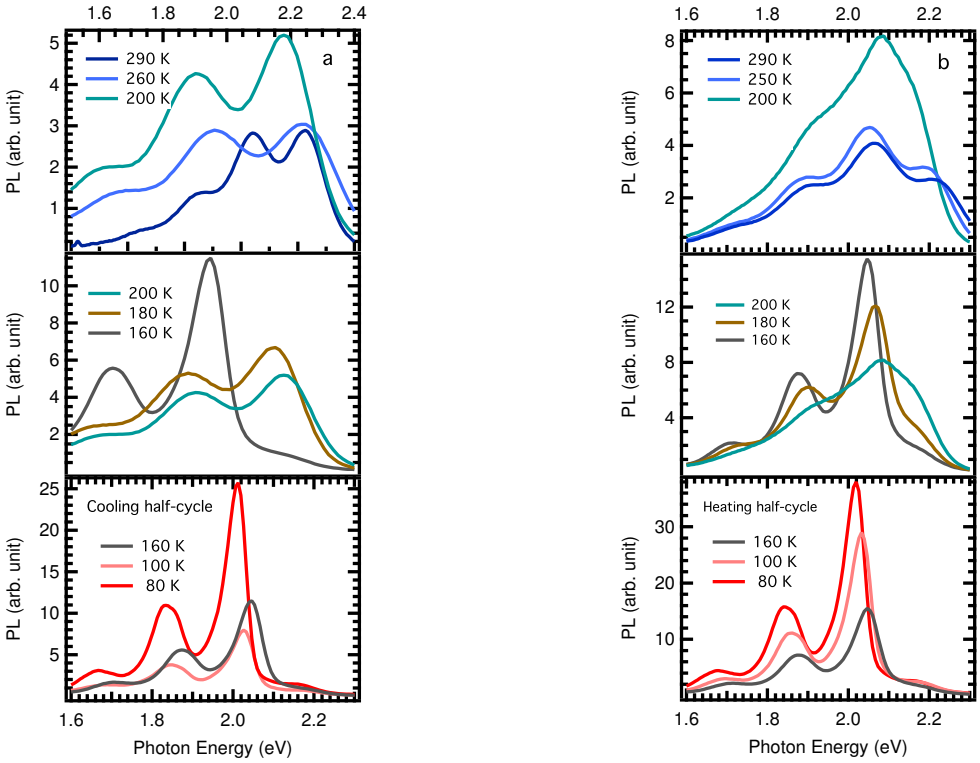

Figure 5.11 – The optical transitions of MEH-PPV/UHMW PS gels as a function of temperature, taken for PL a: cooling half-cycle and b: heating half-cycle.

ture at which the MEH-PPV/UHMW PS gels undergo the red-phase transition. The main difference between the two cycles is that the red-phase does not occur at exactly same temperature in the heating and cooling cycles. The critical temperature is about 160-170 K at different measurements when cooling the sample whereas this temperature raises to approximately 170-180 K in the heating cycle. In other words, the sample undergoes different conformation transition during the cooling half-cycle compared to the heating half-cycle (that shall be discussed later in section 5.7.1).

In Fig. 5.12 we display the PL spectra of the MEH-PPV/UHMW PS gels (wt% 3.0 solution containing 5.0×10^{-5} M) (a) at 290 K and (b) at 80 K along with the Franck-Condon fit using equation 5.1. Note that the PL spectra have been corrected for the cubic dependence of the radiative decay rate on photon frequency (ω^3). We observe a $0-0$

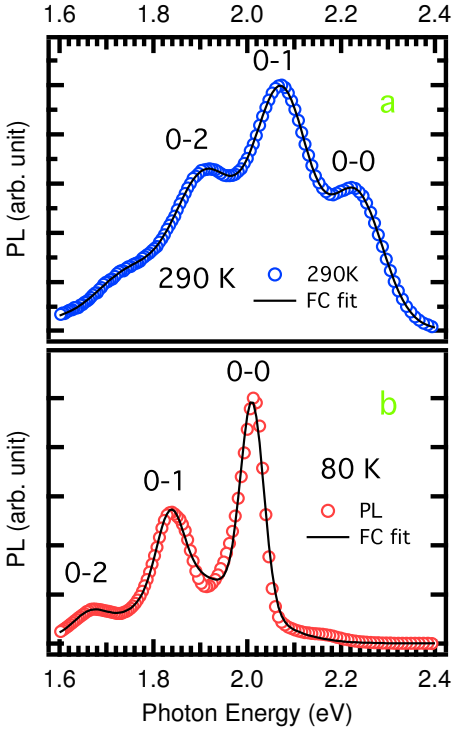

Figure 5.12 – Franck-Condon analysis to the spectra at 290 K (a) and at 80 K (b) for MEH-PPV/UHMW PS gels wt% 3.0 solution containing 5.0×10^{-5} M. The PL spectra (circles), and the solid line shows the Frank-Condon fit. The $0-0$, $0-1$ and the $0-2$ peaks are shown. The PL spectra have been corrected for the cubic dependence of the radiative decay rate on photon frequency (ω^3).

(2.01 eV)/$0-1$ (1.83 eV) PL line-strength ratio that is significantly larger in the MEH-PPV/UHMW PS gels at low temperature compare to a $0-0$ (2.22 eV)/$0-1$ (2.07 eV) ratio at 290 K; we discuss this trend in more detail later in this chapter.

A: The Gaussian line width of the $0-0$ transition ($S_0 \rightarrow S_1$): The Gaussian line width *i.e.* the standard deviation σ of the Gaussian function is extracted by fitting the PL data to equation 5.1. At lower temperatures, σ is 30 meV, which is approximately

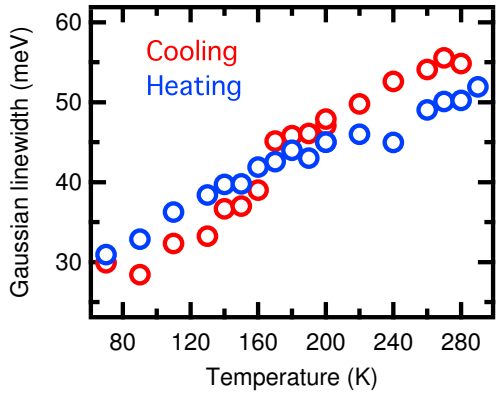

Figure 5.13 – The standard deviation σ of the Gaussian line width for the $0-0$ $S_0 \rightarrow S_1$ in UHMW PS/MEH-PPV gels (wt%3.0 solution containing 5.0×10^{-5} M).

half of that at high temperatures (*i.e.* 54 meV in the cooling half-cycle and 51 meV in the heating half-cycle). Change in σ is possibly a consequence of inhomogeneous line widths and disordered distributions at different temperatures.

B: The $0-0/0-1$ PL line-strength ratio: The evolution of the $0-0/0-1$ PL line-

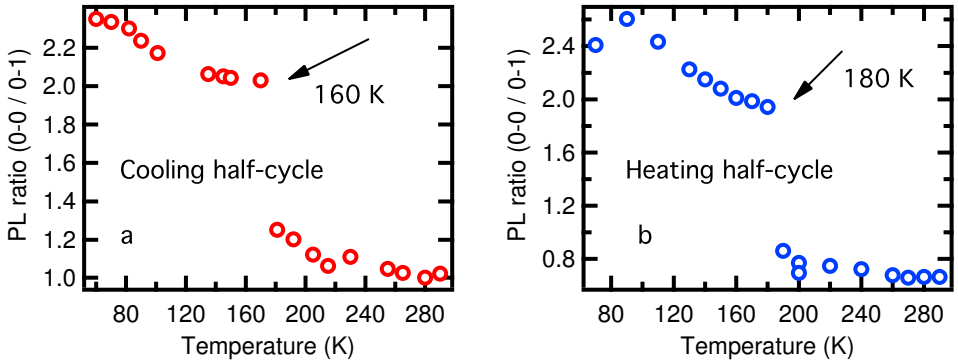

Figure 5.14 – The $(0-0/0-1)$ PL line strength ratio as a function of temperature extracted from Franck-Condon analysis (a) cooling half-cycle (b) heating half-cycle. The $0-0/0-1$ ratio decreases as the temperature grows, that is the characteristic of a J-aggregate polymer.

strength ratio as a function of temperature via a fit with Franck-Condon model (equation

5.1) for the cooling-heating cycle is shown in Fig. 5.14. The $0-0/0-1$ PL line-strength ratio is roughly 2-3 at low temperatures and decreases with increasing temperature. Furthermore, figures 5.14 a and b show that the temperature dependence of $0-0/0-1$ PL line-strength ratio is not linear and turns over at approximately 170 K and 180 K in the cooling and heating half-cycle respectively. The ratio greater than one, also decreasing with increasing temperature characterise a dominant intra-chain (J-like) behaviour as discussed in chapter 5.5.2.

C: Huang-Rhys factors ($0-2/0-1$ **PL line-strength ratio):** It is also possible to extract Huang-Rhys factors via fit with Franck-Condon model by simply taking $0-1$, $0-2$ from measured PL intensity ranging from 80 K to 290 K, see Fig. 5.15.

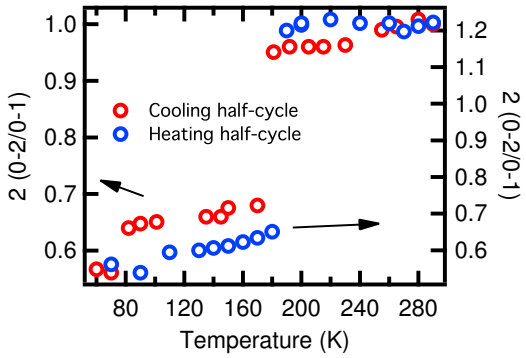

Figure 5.15 – $(2\times0-2/0-1)$ as a function of temperature extracted from Franck-Condon fitting, cooling half-cycle in red and heating half-cycle in blue. the Huang-Rhys parameter increases as temperature increases, that is the characteristic of a J-aggregate polymer.

We deduced values between $\sim 0.6-1$ in the cooling half-cycle and values between $\sim 0.6-1.2$ in the heating half-cycle. Huang-Rhys factors are constant over the entire temperature range investigated for the red phase *i.e.* 80 K to 160-180 K. This results is in a good agreement with the results shown by Yamagata et al. for MEH-PPV solution (80 K to 150 K). [112] Moreover, Huang-Rhys factors are constant over the entire temperature range investigated for the blue phase $\sim 160-290$ K. As shown in Fig. 5.15, the values found for Huang-Rhys factors changes suddenly at the temperature where the red-blue transition occurs from smaller values at low temperatures ~ 0.6 compared

to $\sim 1-1.2$ at higher temperature. That can be possibly a consequence of different conformation behaviour in the polymer chains.

D: The pure electronic transition peak energy (E_{0-0}): Fig. 5.16 shows the temperature dependence of the pure electronic transition peak energy during the cooling-heating cycle. The redshift of the PL peak energy with decreasing temperature could

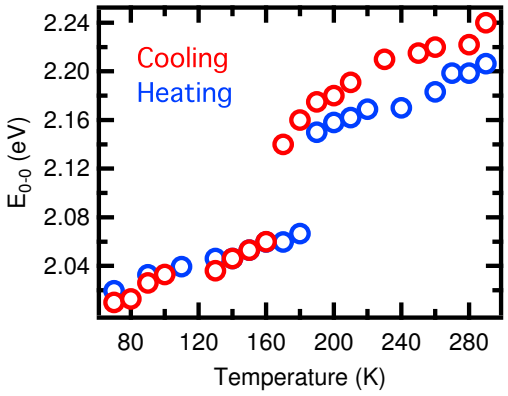

Figure 5.16 – The positions of the $0-0$ peaks for PL spectra from the Franck-Condon fits, cooling half-cycle in red and heating half-cycle in blue.

be associated to the reduction of thermal disorder and planar conformation. This redshift in the PL peak energy with decreasing temperature could be associated to the chain elongation that increases the effective conjugation length. [119, 120] Furthermore the peak energy positions, in cooling and heating, reflect a consistent PL shift up to approximately 160 K above which we can clearly see features corresponding to a hysteresis behaviour. This indicates different conformation behaviour in the MEH-PPV polymer,

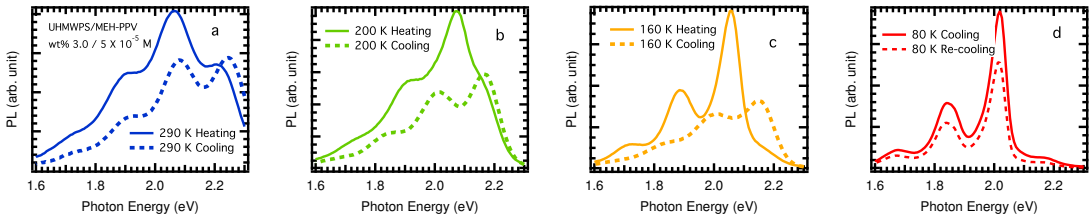

Figure 5.17 – Comparison of the PL spectrum in the cooling-heating cycle at three different critical temperatures a: 290 K b: 200 K c: 160 K d: as well as regaining the red phase at 80 K, for UHMW PS/MEH-PPV (wt%3.0 solution containing 5.0×10^{-5} mol/l).

as seen in Fig. 5.10 and shown in Fig. 5.17 with more emphasis on the spectrum dissimilarity. At some temperatures the spectrum significantly changes due to the conformation transition. Fig. 5.17 d shows how the red phase is retained.

E: Exciton coherence: In what follows, we found the exciton coherence length in MEH-PPV/ UHMW PS, based on section 5.5.3. It was discussed that $0-0/0-1$ PL ratio is a direct measure of the coherence length, N_{coh}, in a J-aggregate (equation 5.7, $I_{0-0}/I_{0-1} = \kappa N_{coh}/\lambda^2$). κ accounts for the impact of vibronic coupling on charge separated states and close to unity however it deviates from unity when excitons are delocalised through bond as well as within the π-stacks. [112] Yamagata et al. found $\kappa = 0.62$ through the numerical calculation for MEH-PPV.

By adopting $\kappa = 0.62$, $0-0/0-1$ (same as in Fig. 5.14) and approximate value of unity for λ^2 from our results shown in figure 5.15 and according to $L_{||} = (N_{coh}-1)d$, we found $N_{coh} \sim 6$. Fig. 5.18 shows the number of coherently connected chromophore as a function of temperature in the cooling-heating cycle. It is clearly shown that the exciton coherence decreases as the temperature increases, however the exciton becomes even more localised in the heating half-cycle. Note that d is the distance between the nearest neighbours chromophors within the chain.

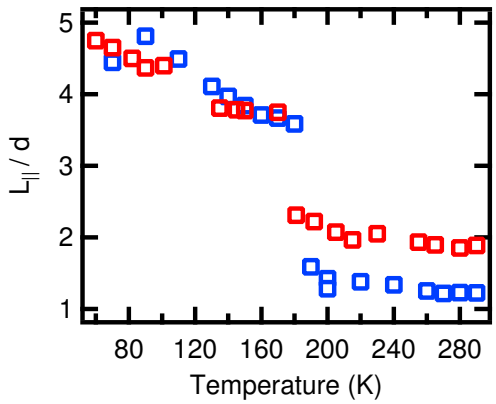

Figure 5.18 – Exciton coherent length in the cooling-heating cycle for disordered MEH-PPV/UHMW PS gels (wt%3.0 solution containing 5.0×10^{-5} M). $N_{coh} \sim 6$.

5.7 Discussion/Conclusion

Our results demonstrate a gel-processed matrix of ultra high molecular weight polystyrene for poly [2-methoxy, 5-(2'-ethyl-hexoxy)-1,4-phenylene vinylene], MEH-PPV conjugated polymer guest. MEH-PPV in a polar solvent environment MeTHF solution in the polymeric host matrix shows a conformation transition from coil transition referred to as a blue phase and chain-extended conformation referred to as a red phase.

The objective of this work was to achieve solution-processable materials also ensure that the red-phase MEH-PPV maintains in the gel similar to the solution. With the aids of photophysics features (by temperature-dependent PL measurement), we demonstrated identical conformation transition in the MEH-PPV/UHMW PS gels to the corresponding MEH-PPV solution, consistent with the previous works. [111, 112] In addition to the previous works on the MEH-PPV solution, we demonstrated how the conformation changed through a heating half-cycle.

5.7.1 Polar solvent environment

The effects of solvent and environment on PL spectra can be due to several factors in addition to solvent polarity. However since in a particular measurement more than one effect can affect the chromophore, it is challenging to know which effect is dominant.

Given that chromophores dipole moment (μ_E) is larger in the excited state than that of in the ground state (μ_G), following excitation, the polar solvent dipoles will reorient around (μ_E), which lowers the energy of the excited state. As the solvent polarity is increased, this effect becomes larger, resulting in emission at lower energies or longer wavelengths [see Fig. 5.19]. [20] Moreover, a poor solvent may cause aggregation in the polymer, as the polymer tends to minimise the interaction with poor solvent. [121]

Collison et al. showed the PL decays for MEH-PPV solutions, of equal concentration but varying solvent quality. The decay of good solvent solutions are almost mono-exponential, the decay time increases with decreasing the solvent quality. Collison et al. hypothesized that this long-lived PL is associated with the singlet state following back-transfer from non-emissive interchain excited states to intrachain excited states.

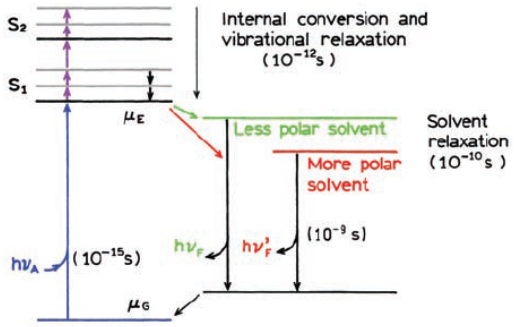

Figure 5.19 – Jablonski diagram for chromophres with solvent relaxation. Figure adopted from reference [20].

Given that it is likely that a poor solvent causes the torsional motion along the backbone, to be suppressed by the presence of adjacent chains, so that to avoid polymer-solvent interactions. Solvent-induced packing thus contributes to ordering the chains. [121] Furthermore, Collison et al. explained the room-temperature PL spectral line shape of MEH-PPV dissolved in a mixture of toluene-hexane solvent via a two-emitter model and concluded that the spectral line shapes are consistent with single chain however, the red-phase corresponds to aggregates.[112, 121] In short, the poor solvent can also be a cause for aggregation of MEH-PPV in the gel.

5.7.2 Different conformation transition in the cooling and heating cycles

Here, we can discuss the different conformation transition in the heating and cooling half cycles. This difference has something to do with difference in the physical aggregation of molecules. In the cooling half-cycle we start from a very well dissolved polymer chains, because we have dissolved the polymer at high temperature. Therefore, the polymer chains are well separated ones from the others, as corresponding to a diluted solution of polymers. However, as decreasing the temperature, at some point the solubility of the polymer decreases and the polymer chains tend to aggregate (specially in poor solvent environment). Note that this aggregation might happen once the red phase has been already formed, hence it might not affect the amount of the red phase, meaning that the already planarised molecules might aggregate. Then, as heating the sample up this

molecular aggregates might be insoluble, which is why MEH-PPV chains do not show anymore the behavior of an isolated molecule. Note that in order to dissolve the MEH-PPV at the beginning (*i.e.* separate the molecules) , we need to increase the temperature a lot (120 °C).

5.7.3 Temperature dependence of absorption and PL spectra

Here we discuss the red-phase of the MEH-PPV/UHMW PS gels by weakly coupled HJ-aggregates in which the interchain splitting, ΔE_{inter}, is roughly an order of magnitude smaller than the $0-0$ intrachain exciton bandwidth, ΔE_{intra}. [15, 112]

The origin of the PL is the lowest energy exciton, [122] the lowest vibronic peak $(0-0)$ in the absorption spectrum overlaps the highest vibronic peak of the PL that is consistent with J-aggregate behaviour. Moreover, there is no feature of mirror image symmetry in the absorption and PL spectra, since Holstein-based Hamiltonians shows that it is not possible to describe the vibronic progressions in absorption and PL with the same HR factor. Aggregation in the molecules cause the absorption and PL line shapes to change; these changes are reflected in energy (spectral) shifts and a redistribution of vibronic peak intensities. [29] Upon cooling the gel the PL spectra is dramatically (~ 230 meV) red-shifted compared to previous works. [117–119] PL is redshifted from 2.24 eV $(0-0)$ at 290 K to 2.08 eV $(0-0)$ at 80 K and a reversible blue-shift towards 2.20 eV at 290 K when the gel is warmed up (see Fig. 5.10). Yamagata et al. also reported a dramatic redshift (~ 180 K) in the pure $0-0$ transition of PL spectra from 300 to 80 K. However Köhler et al. reported a redshifted PL peak approximately by 130 meV from 300 to 80 K. [111]

Assessment of PL vibrational peak intensities using Franck-Condon analysis clearly shows that PL I_{0-0}/I_{0-1} ratio diminishes as temperature rises (see Fig. 5.14) that is assigned to a J-behaviour based on our discussion in 5.5.2. Moreover, given that the I_{0-0} is enhanced compared to the I_{0-1} in a J-aggregate, a ratio of greater than 1 is expected which is opposite in a H-aggregate case. I_{0-0}/I_{0-1} increases from 1.02 at 290 K to 2.38 at 80 K in the red-phase during the cooling, however dropping from 2.38 at 80 K to 0.66 at 290 K during heating half-cycle. It is concluded that the MEH-PPV/UHMW PS gels

remains H-aggregated at the end of the cycle. There is also a broadening of the linewidth, ~ 30 meV to ~ 55 meV in good agreement with measured values in MEH-PPV solution as reported by Yamagata et al., 24 meV at 80 K and 55 meV at 300 K. [15] Note that disorder adds a red-shift to the PL spectrum that creates a Stokes shift which is even smaller for the J-aggregate. [29] In short, there are evidences of J-aggregation in the red-phase and H-aggregation in the blue-phase, which is consistent with the chain extended conformation to coil conformation mentioned by Köhler et al.. [111] As mentioned before, Huang-Rhys factor defines the strength of electron-phonon or exciton-phonon coupling, Huang-Rhys factor of zero contributes to only a $0-0$ peak and increases with temperature. Here we point out that the photophysics of MEH-PPV results mainly from intrachain π-electron coupling. Enhanced I_{0-0}/I_{0-1} at low temperature is also due to the reduced interchain coupling that can be assigned to the reduced torsional disorder and a higher fraction of intramolecular interactions that contributes to the emission. In addition, thermal disorder reduces as temperature decreases hence the spatial extent of the electronic wave function increases such that excitons are more delocalised. Temperature dependence of PL cause variation in the relative intensity of vibrational modes and linewidth such that at higher temperatures, probability of electron scattering by vibrational modes of the molecules are higher. Thus the Huang-Rhys factor is higher. We conclude that the smaller value of Huang-Rhys factor at low temperature is associated with longer conjugation length and coherence length within the chains. The chain is extended at low temperatures compared to high temperatures. The results of MEH-PPV/U-HMW PS gels are consistent with previous works on the solution of MEH-PPV reported by Köhler et al. and Yamagata et al.. [111, 112] and the red-phase of the solution was successfully reproduced in a host matrix.

Comparison of a linear J-aggregate: polydiacetylene (PDA) with a very disordered J-aggregate MEH-PPV/UHMW PS gels

Here we compare the J-aggregation in PDA versus the J-aggregation in MEH-PPV/U-HMW PS gels. Photophysics of the red-form of isolated PDA chains polymerised from the diacetylene monomer crystal shows that PDA chains are highly emissive. As such, the PL spectrum characterises ultra-narrow lines that peaks at 2.28 eV. Side bands due

to the stretching modes are approximately 0.174 eV and 0.25 eV below the $0-0$ peak. The ultra-narrow line of the vibronic progression ($\sim 20-30\,\mathrm{cm}^{-1}$) reflects a near-free disorder situation. The $0-0$ absorption peak intensity is also dominant, and is about a factor of ten larger than the vibronic side band. Hence, there is no mirror-image symmetry between the absorption and PL line shapes, which is often expected in single-chromophore systems. Within a single PDA wire, exciton is delocalised over a range of 1-10 μm. Furthermore the $0-0/0-1$ PL intensity ratio extracted from the PL spectrum is approximately 60 at T = 10 K. When temperature increases to room temperature, the $0-0/0-1$ PL intensity ratio decreases to approximately 10. Hence, compare to the characterisation of PDA PL spectrum, we can conclude that MEH-PPV/UHMW PS gel is a very disorder J-aggregate.

5.7.4 Short-range charge transfer and long-range Coulombic couplings

As we discussed in chapter 2.2.3.2, Yamagata et al. has developed the discussion of hybrid coupling by using a Holstein-style Hamiltonian including both Frenkel and charge-transfer (CT) excitons. [25, 26] In late 2015, Hestand et al. considered the interference between the two couplings when defining H and J-aggregates based on short- and long-range couplings. [25] It was also discussed that the short range coupling is given by $J_{CT} = -\frac{2t_e t_h}{E_{CT}-E_F}$ and the H- J-aggregates photophysical behaviours are identified by $J_{CT} > 0$ and $J_{CT} < 0$ respectively.

In what follows, we also briefly discuss the blue versus the red phase in MEH-PPV/ UHMW PS gels based on this recent theory. However, in order to precisely interpret our results and molecule aggregation in MEH-PPV/UHMW PS gels based on this theory, the overlap integrals and coupling strength should be precisely calculated. Fig. 5.21 shows the PL spectra; solid-blue line in the beginning of the cooling cycle at 290 K, red line at 80 K and the blue-dashed line at the end of the heating cycle at 290 K. According to the developed theory as the strength of the charge transfer and Coulombic couplings are the same, those couplings interfere destructively and create a "null aggregate" which spectroscopically resembles uncoupled molecules. As such, it is possible to attribute the same $0-0$ and $0-1$ ratio in the solid-blue line PL spectrum to the "null aggregate" and

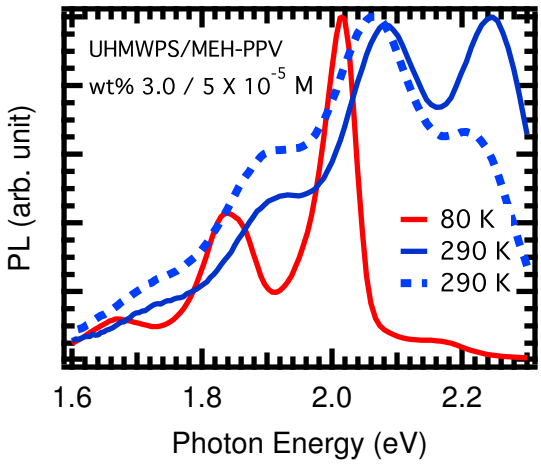

Figure 5.20 – PL spectra of MEH-PPV/UHMW PS gels at 290 K where the blue phase dominates and at 80 K where the red phase dominates in the cooling-heating cycle.

$J_{CT} + J_{Coul} = 0$. Based on this theory the cooling half cycle can be interpreted such that assuming a constant value for J_{CT} (e.g. $J_{CT} = 0.2$, this value has been taken from the calculated value for J_{CT} for perylene-based π-stacks from reference [25]). Note that, for instance in Jj-aggregate the first letter indicates that $J_{Coul} < 0$ and the second letter indicates that $J_{CT} < 0$. The lower case further indicates that $|J_{Coul}| \gg |J_{CT}|$. [25]

Calculated absorption spectra (black) for π-stacks containing $N = 10$ chromophores based on the Frenkel/Holstein Hamiltonian by Hestand et al. is shown in Fig 5.21. It is possible to interpret the results shown in Fig. 5.21 based on this theory. For instance, the dashed-blue line can resemble a CT-H aggregate that is slightly red-shifted with respect to the "null aggregate", and based on this theory our red-phase J-aggregate (red line) at 80 K looks like a Jh as the $J_{Coul} < 0$ and $J_{CT} > 0$, in case of $|J_{Coul}| \gg |J_{CT}|$, one can neglect the second letter, giving the conventional "J-aggregate" notation.

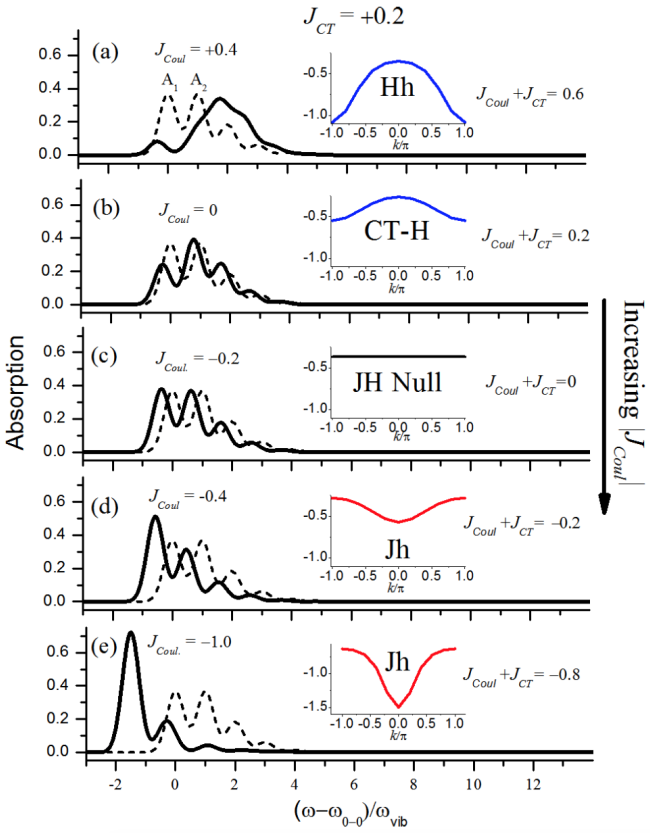

Figure 5.21 – Calculated absorption spectra (black) for π-stacks containing N=10 chromophores in based on the Frenkel/Holstein Hamiltonian. Figure adopted from reference [25]

In short, this wok demonstrates that the morphology of MEH-PPV polymer can be manipulated through altering the critical temperature through which the conformation transition occurs; above the critical temperature the polymer exists in a disordered coil morphology, whilst upon cooing the gel, through the transition temperature, the polymer assembles into aggregates. The chain-extended conformation or elongated chain in the red phase causes the absorption and the PL spectra to be red-shifted.

CHAPTER 6

CONCLUSION

The present research contributed to the fundamental understanding of hybrid photovoltaic heterostructures and devices made thereof. The research also had a strong footing in development of readily solution-processable materials along with the study of their morphology through the study of photophysics properties. This research further addressed the obvious need to relate molecular order and conformational arrangements in polymeric semiconductors with electronic and optical phenomena in order to ultimately improve the OPV and optoelectronic devices performance. To take a step forward in this regard, in chapter 4 we focused on the interface modification of the hybrid bulk heterostructures by incorporating interface modifiers at the donor acceptor interface.

Interface can be modified and controlled by using selective materials for structural engineering. Interface modifiers can significantly assist in enhancement of exciton diffusion and eventually charge separation without compromising absorption or charge collection. The OPV cell of our interest comprised of polymer P3HT and nanocrystals ZnO. Introducing the N3 dye and 6TP at the interface creates a potential offset by inducing dipole sheet between the donor and the acceptor where the band-edge potential of ZnO shifts up or down depending on the dipoles orientation. Dipoles directed toward the acceptor (ZnO) shift the band-edge potential of ZnO away from the vacuum level of the donor (P3HT), resulting in reduction in both the effective bandgap between the conduction band minimum and HOMO, and V_{oc}. On the other hand, dipoles pointing away from ZnO bring the band-edge potential of ZnO closer to the vacuum level of P3HT which increases both the interface bandgap and V_{oc}.

Moreover, interface modifiers adhere to the surface where the non-workable area such as traps and defect density can be filled. That phenomenon can reduce the density of carriers which trapped and do not reach the interface area to become free charges towards respective electrodes. Interface modifiers also reduce recombination and facilitate charge separation by increasing the area between the donor and the acceptor that contribute to

an increased V_{oc}.

The analysis we did in chapter 4 demonstrate that hybrid photovoltaic cells consisting of P3HT: ZnO active layers are more efficient with N3 and 6TP interface modifiers. We determine the increased efficiency by measuring the current density as a function of voltage, as well as identifying the formation of long-lived polarons via quasi-steady state photoinduced absorption (PIA) spectroscopy measured at low temperature. We investigate the kinetics of those polarons by measuring the dependence of the PIA signal on the pump-laser modulation frequency.

We find that a change in the conduction band minimum of ZnO nanocrystals and the HOMO level of P3HT polymer results in an increase in the V_{oc}. The loss due to the recombination of carriers is lessened, causing the photocurrent to be enhanced. Moreover, the long-lived polarons formation is confirmed not only in P3HT: ZnO, but also in P3HT: ZnO-N3 and P3HT: ZnO-6TP. Furthermore, the kinetics of the long-lived polarons reveal the influence of the molecular interface modification on the average lifetime of polarons. Considering these features, we conclude that modifying the P3HT: ZnO interface with N3 and 6TP improves the performance of hybrid photovoltaic cells based on P3HT: ZnO.

In the research discussed in chapter 5 we focused on the processing of a polymeric host matrix material for optoelectronic applications. The polymeric host matrix is a processed material "microscopically liquid whilst macroscopically solid", [113] such that it takes advantage of both phases in the relevant spatial domains, with which we contributed to new knowledge of next generation material system, with processing means with the goal to facilitate large-area processing. The polymeric host matrix, UHMW PS enables trapping and protecting conjugated-polymeric solution of our interest, *i.e.* red-phase MEH-PPV, to eventually be used for optoelectronic applications. We also introduced MEH-PPV in the UHMW PS gel after which a homogeneous solution was prepared. To ensure that MEH-PPV red-phase at low temperatures maintains in the UHMW PS gel similar to the red-phase in the solution we adopted spectroscopic tools. Taking the advantage of interrelations between the microstructure and electronic processes made it possible to realize about the red-phase MEH-PPV/UHMWPS gel through

the photophysical properties.

We studied the photophysics of red-MEH-PPV/UHMWPS gel by means of temperature-dependent PL through a heating-cooling cycle. We measured PL of red-MEH-PPV/UHMW PS gel between the temperatures range from 290 K down to 80 K within the cooling half-cycle, the temperature then was increased to 290 K within the heating half-cycle. The PL spectrum characterises a J-like spectra at 80 K where the cooling half-cycle was ceased whereas it characterises an H-like spectrum at the end of the heating half-cycle. This phenomena occur approximately around $\sim 160 - 180$ K through the temperature-dependent cycle.

The analysis we did in chapter 5 based on HJ hybrid model that incorporates exciton coupling, the coupling between the electronic transition and intramolecular vibrations, and disorder demonstrates a J-aggregate behaviour of MEH-PPV/UHMWPS gel. [15, 112] In addition to the intrinsic properties of the aggregates, the spectral red/blue shift, our interpretation relies on the PL peaks ratio analysis. That has recently been known as a powerful tool to obtain additional spectral features with which to distinguish H- vs. J-aggregation. [15, 112]

Both $0-0$ to $0-1$ absorption and PL ratio are greater than unity. The PL ratio increases with decreasing the temperature. It is shown that increase PL ratio is consistent with increased exciton coherence length where is spread over approximately 6 repeat units. These properties characterise the red-MEH-PPV/UHMW PS gel as J-aggregate molecule. The J-like behaviour is significantly due to the dominance of intra- versus inter-chain exciton bandwidth. [112] In terms of chain conformation, increased torsional disorder at high temperatures reduces the intrachain exciton bandwidth and shorten the exciton coherence length. J-aggregation is associated with chain elongation and alignment of the unit cell transition dipole moments within the coherence length (through bond) and disorder cause transition dipole moments to be randomly aligned. [112] Moreover, given that the PL spectra at high temperatures with the $0-0$ to $0-1$ reduced to less than unity, it is therefore possible to conclude that the transition dipole moments are also aligned between the chains (through space). The high-temperature characteristics are referred as to blue-phase whereas the the low-temperature characteristics are referred

as to red-phase. [111] Hence, we conclude that in the coiled blue-phase the transition dipole moments are randomly oriented within the smaller number of the repeat unit compared to the chain-extended red-phase (as results show). In fact we demonstrated that the gelated UHMW PS using a polar organic solvent with MEH-PPV can lead to a solid-like red-phase of MEH-PPV. It is important to note that the poor solvent *i.e.* polar MeTHF, may also cause aggregation in the polymer, as the polymer tends to minimise the interaction with poor solvent. [121] Finally, we point out that $0-0$ to $0-1$ PL peak ratio undergoes a the substantial increase when the blue-phase is converted to red-phase MEH-PPV (coiled confirmation to chain extended-conformation) is due to an enhanced coherence length along the chain ($N_{coh} \sim 6$ repeat units) that is associated with chain elongation. Red-phase MEH-PPV/UHMW PS gel is thus assigned to a disordered J-aggregate compared to the linear J-aggregate PDA discussed in chapter 5.7.3 in which the $0-0$ transition manifests itself by an ultra-narrow line width in the PL spectrum.

Future works

Interface modification of P3HT:ZnO hybrid photovoltaic cell

We will complete our study on the charge generation mechanism of hybrid photovoltaic cells by performing two-dimensional photocurrent spectroscopy. We will investigate charge generation mechanism on < 100 fs timescales that is yet to be unravelled.

The red-phase MEH-PPV/UHMW gel

We will accomplished our study on the red-phase MEH-PPV/UHMW gel by implementing the two-dimensional coherent photoluminescence spectroscopy which allows us to directly observe the effects of conformation-dependent exciton coupling between the chromophores and to investigate the correlation between the excited states. Investigation of processing protocols with the goal to achieve the red-phase MEH-PPV/UHMW gel at room temperature by applying knowledge gain from study on electronics structure.

BIBLIOGRAPHY

[1] C. K. Chiang, C. R. Fincher, Y. W. Park, A. J. Heeger, H. Shirakawa, E. J. Louis, S. C. Gau, and A. G. MacDiarmid, *Electrical Conductivity in Doped Polyacetylene*, Phys. Rev. Lett. **39**, 1098.

[2] E. Collini and G. D. Scholes, *Coherent Intrachain Energy Migration in a Conjugated Polymer at Room Temperature*, **323**, 369 (2009).

[3] D. C. Olson, J. Piris, R. T. Collins, S. E. Shaheen, and D. S. Ginley, *Hybrid photovoltaic devices of polymer and ZnO nanofiber composites*, Thin Solid Films **496**, 26 (2006).

[4] T. Nagata, S. Oh, Y. Yamashita, H. Yoshikawa, N. Ikeno, K. Kobayashi, T. Chikyow, and Y. Wakayama, *Photoelectron spectroscopic study of band alignment of polymer/ZnO photovoltaic device structure*, Applied Physics Letters **102**, 043302 (2013).

[5] M. Pope and C. E. Swenberg, *Electronic Processes in Organic Crystals and Polymers* (Oxford University Press, 2nd eddition, 1999).

[6] S. W. Koch, M. Kira, G. Khitrova, and H. M. Gibbs, *Semiconductor excitons in new light*, Nature Materials **5** (2006).

[7] K. Jasper, *Modeling the optical properties of excitons in linear and tubular J-aggregates*, International Journal of Photoenergy (2006).

[8] W. P. Su, J. R. Schrieffer, and A. J. Heeger, *Soliton excitations in polyacetylene*, Phys. Rev. B **22**, 2099.

[9] R. E. Peierls., *Quantum Theory of Solids* (Oxford: At the Clarendon Press, 1995).

[10] A. J. Heeger, S. Kivelson, J. R. Schrieffer, and W. P. Su, *Solitons in conducting polymers*, Rev. Mod. Phys. **60**, 781 (1988).

[11] X. Wei, Z. V. Vardeny, N. S. Sariciftci, and A. J. Heeger, *Absorption-detected magnetic-resonance studies of photoexcitations in conjugated-polymer/C_{60} composites*, Phys. Rev. B **53**, 2187 (1996).

[12] R. Farchioni and G. Grosso, *Organic Electronic Materials, Conjugated Polymers and Low Molecular Weight Organic Solids* (Springer, 2001).

[13] E. G. McRae and M. Kasha, *Enhancement of Phosphorescence Ability upon Aggregation of Dye Molecules*, The Journal of Chemical Physics **28**, 721 (1958).

[14] M. Kasha, *Energy Transfer Mechanisms and the Molecular Exciton Model for Molecular Aggregates*, Radiation Research **20**, 55 (1963).

[15] H. Yamagata and F. C. Spano, *Interplay between intrachain and interchain interactions in semiconducting polymer assemblies: The HJ-aggregate model*, The Journal of Chemical Physics **136**, 184901 (2012).

[16] Y. Hajime, *The effects of vibronic coupling on the photophysics of π-conjugated oligomers and polymers*, PhD thesis, Temple University, 2013.

[17] S. Tretiak, A. Saxena, R. L. Martin, and A. R. Bishop, *Conformational Dynamics of Photoexcited Conjugated Molecules*, Phys. Rev. Lett. **89**, 097402 (2002).

[18] S. Karabunarliev, M. Baumgarten, E. R. Bittner, and K. Müllen, *Rigorous Franck-Condon absorption and emission spectra of conjugated oligomers from quantum chemistry*, The Journal of Chemical Physics **113**, 11372 (2000).

[19] R. E. Di Paolo, d. M. J. Seixas, J. Pina, H. D. Burrows, J. Morgado, and A. L. Macanita, *Conformational Relaxation of p-Phenylenevinylene Trimers in Solution Studied by Picosecond Time-Resolved Fluorescence*, ChemPhysChem **8**, 2657 (2007).

[20] J. R. Lakowicz, *Principles of fluorescence spectroscopy* (Springer, New York, 2006).

[21] F. C. Spano, *Modeling disorder in polymer aggregates: The optical spectroscopy of regioregular poly(3-hexylthiophene) thin films*, The Journal of Chemical Physics **122** (2005).

[22] F. C. Spano, *The Spectral Signatures of Frenkel Polarons in H- and J-Aggregates*, Accounts of Chemical Research **43**, 429 (2010).

[23] M. R. Philpott, *Theory of the Coupling of Electronic and Vibrational Excitations in Molecular Crystals and Helical Polymers*, The Journal of Chemical Physics **55**, 2039 (1971).

[24] F. C. Spano, J. Clark, C. Silva, and R. H. Friend, *Determining exciton coherence from the photoluminescence spectral line shape in poly(3-hexylthiophene) thin films*, The Journal of Chemical Physics **130**, 074904 (2009).

[25] N. J. Hestand and F. C. Spano, *Interference between Coulombic and CT-mediated couplings in molecular aggregates: H- to J-aggregate transformation in perylene-based π-stacks*, The Journal of Chemical Physics **143** (2015).

[26] H. Yamagata, D. S. Maxwell, J. Fan, K. R. Kittilstved, A. L. Briseno, M. D. Barnes, and F. C. Spano, *HJ-Aggregate Behavior of Crystalline 7,8,15,16-Tetraazaterrylene: Introducing a New Design Paradigm for Organic Materials*, The Journal of Physical Chemistry C **118**, 28842 (2014).

[27] H. Yamagata, C. M. Pochas, and F. C. Spano, *Designing J- and H-Aggregates through Wave Function Overlap Engineering: Applications to Poly(3-hexylthiophene)*, The Journal of Physical Chemistry B **116**, 14494 (2012).

[28] A. Perevedentsev, *Chain Conformation and the Photophysics of Polyfluorenes*, PhD thesis, Imperial College of Science, Technology and Medicine London, United Kingdom, 2015.

[29] F. C. Spano and C. Silva, *H-and J-aggregate behavior in polymeric semiconductors*, Annual review of physical chemistry **65**, 477 (2014).

[30] J. Clark, J.-F. Chang, F. C. Spano, R. H. Friend, and C. Silva, *Determining exciton bandwidth and film microstructure in polythiophene films using linear absorption spectroscopy*, Applied Physics Letters **94** (2009).

[31] T. Niles, Edwards, J. D. Roehling, H. Yamagata, J. Wise, Adam, S. Frank C., J. Moulé, Adam, and J. K. Grey, *J-Aggregate Behavior in Poly-3-hexylthiophene Nanofibers*, The Journal of Physical Chemistry Letters **3**, 259 (2012).

[32] M. Baghgar, E. Pentzer, A. J. Wise, J. A. Labastide, T. Emrick, and M. D. Barnes, *Cross-Linked Functionalized Poly(3-hexylthiophene) Nanofibers with Tunable Excitonic Coupling*, ACS Nano **7**, 8917 (2013).

[33] M. Baghgar, J. A. Labastide, F. Bokel, R. C. Hayward, and M. D. Barnes, *Effect of Polymer Chain Folding on the Transition from H- to J-Aggregate Behavior in P3HT Nanofibers*, The Journal of Physical Chemistry C **118**, 2229 (2014).

[34] F. Paquin, H. Yamagata, N. J. a. Hestand, M. Sakowicz, N. Bérubé, M. Côté, L. X. Reynolds, S. A. Haque, N. Stingelin, F. C. Spano, and C. Silva, *Two-dimensional spatial coherence of excitons in semicrystalline polymeric semiconductors: Effect of molecular weight*, Phys. Rev. B **88**, 155202 (2013).

[35] C. Hellmann, N. Treat, A. Scaccabarozzi, J. Hollis, F. Fleischli, J. Bannock, J. de Mello, J. Michels, J.-S. Kim, and N. Stingelin, *Solution Processing of Polymer Semiconductor: Insulator Blends-Tailored Optical Properties Through Liquid-Liquid Phase Separation Control*, JOURNAL OF POLYMER SCIENCE PART B-POLYMER PHYSICS **53**, 304 (2015).

[36] A. E. Becquerel, *On electric effects under the influence of solar radiation*, Compt. Rend. **9**, 561 (1839).

[37] S. H. Park, A. Roy, S. Beaupre, C. N. Cho, Shinuk and, J. S. Moon, D. Moses, M. Leclerc, K. Lee, and A. J. Heeger, *Bulk heterojunctions solar cells with internal quantm efficiency approaching 100%*, Nature Photonics **3**, 297 (2009).

[38] P. Peumans, A. Yakimov, and S. R. Forrest, *Small molecular weight organic thin-film photodetectors and solar cells*, Journal of Applied Physics **93**, 3693 (2003).

[39] G. Yu, J. Gao, J. C. Hummelen, F. Wudl, and A. J. Heeger, *Polymer Photovoltaic Cells: Enhanced Efficiencies via a Network of Internal Donor-Acceptor Heterojunctions*, Science **270**, 1789 (1995).

[40] M. Hiramoto, H. Fujiwara, and M. Yokoyama, *Three-layered organic solar cell with a photoactive interlayer of codeposited pigments*, Applied Physics Letters **58** (1991).

[41] C. J. Brabec, G. Zerza, G. Cerullo, S. D. Silvestri, S. Luzzati, J. C. Hummelen, and S. Sariciftci, *Tracing photoinduced electron transfer process in conjugated polymer/fullerene bulk heterojunctions in real time* , Chemical Physics Letters **340**, 232 (2001).

[42] P. K. H. Nemec and V. Sundstroem, *Charge transport in nanostructured materials for solar energy conversion studied by time-resolved terahertz spectroscopy* , Journal of Photochem. Photobiol., A **215**, 123 (2010).

[43] P. Ravirajan, A. M. Peiró, M. K. Nazeeruddin, M. Graetzel, D. D. C. Bradley, J. R. Durrant, and J. Nelson, *Hybrid Polymer/Zinc Oxide Photovoltaic Devices with Vertically Oriented ZnO Nanorods and an Amphiphilic Molecular Interface Layer*, The Journal of Physical Chemistry B **110**, 7635 (2006).

[44] M. Scarongella, *Charge carrier dynamics at organic interfaces for polymer photovoltaics*, PhD thesis, SB, Lausanne, 2015.

[45] A. L. Briseno, T. W. Holcombe, A. I. Boukai, E. C. Garnett, S. W. Shelton, J. J. M. Frechet, and P. Yang, *Oligo- and Polythiophene/ZnO Hybrid Nanowire Solar Cells*, Nano Letters **10**, 334 (2010).

[46] G. Li, V. Shrotriya, J. Huang, Y. Yao, T. Moriarty, K. Emery, and Y. Yang, *High-efficiency solution processable polymer photovoltaic cells by self-organization of polymer blends* , Nat Mater **4**, 864 (2005).

[47] M. H. Chan, J. Y. Chen, T. Y. Lin, and Y. F. Chen, *Direct evidence of type II band alignment in ZnO nanorods/poly(3-hexylthiophene) heterostructures*, Applied Physics Letters **100**, 021912 (2012).

[48] Y. Vaynzof, D. Kabra, L. Zhao, P. K. H. Ho, A. T.-S. Wee, and R. H. Friend, *Improved photoinduced charge carriers separation in organic-inorganic hybrid photovoltaic devices*, Applied Physics Letters **97**, 033309 (2010).

[49] M. Wang and X. Wang, *P3HT/ZnO bulk-heterojunction solar cell sensitized by a perylene derivative*, Solar Energy Materials and Solar Cells **92**, 766 (2008).

[50] W. J. E. Beek, M. M. Wienk, M. Kemerink, X. Yang, and R. A. J. Janssen, *Hybrid Zinc Oxide Conjugated Polymer Bulk Heterojunction Solar Cells*, The Journal of Physical Chemistry B **109**, 9505 (2005).

[51] W. Beek, M. Wienk, and R. J. Janssen, *Efficient Hybrid Solar Cells from Zinc Oxide Nanoparticles and a Conjugated Polymer*, Advanced Materials **16**, 1009 (2004).

[52] N. S. Sariciftci, L. Smilowitz, A. J. Heeger, and F. Wudl, *Photoinduced Electron Transfer from a Conducting Polymer to Buckminsterfullerene*, Science **258**, 1474 (1992).

[53] E. Buchaca-Domingo *et al.*, *Additive-assisted supramolecular manipulation of polymer:fullerene blend phase morphologies and its influence on photophysical processes*, Mater. Horiz. **1**, 270 (2014).

[54] M. Scarongella, A. A. Paraecattil, E. Buchaca-Domingo, J. D. Douglas, S. Beaupre, T. McCarthy-Ward, M. Heeney, J.-E. Moser, M. Leclerc, J. M. J. Frechet, N. Stingelin, and N. Banerji, *The influence of microstructure on charge separation dynamics in organic bulk heterojunction materials for solar cell applications*, J. Mater. Chem. A **2**, 6218 (2014).

[55] M. Scarongella, J. D. Jonghe-Risse, E. Buchaca-Domingo, M. CausaâÄô, Z. Fei, M. Heeney, J.-E. Moser, N. Stingelin, and N. Banerji, *A Close Look at Charge*

Generation in Polymer:Fullerene Blends with Microstructure Control, Journal of the American Chemical Society **137**, 2908 (2015).

[56] C. Muller, T. A. M. Ferenczi, M. Campoy-Quiles, J. M. Frost, D. D. C. Bradley, P. Smith, N. Stingelin-Stutzmann, and J. Nelson, *Binary Organic Photovoltaic Blends: A Simple Rationale for Optimum Compositions*, Advanced Materials **20**, 3510 (2008).

[57] H. Kallel, G. Latini, F. Paquin, R. Rinfret, N. Stingelin, and C. Silva, *Background-free quasi-steady-state photoinduced absorption spectroscopy by dual optical modulation*, http://arxiv.org/pdf/1007.3035v2.pdf (2010).

[58] B. P. Chhetri, *Ultrafast photophysics of π-conjugated polymers for organic photovoltaic applications* , PhD thesis, The University of Utah, 2012.

[59] E. Rezasoltani, M. Wang, I. G. Hill, and C. Silva, *The influence of molecular interface modification on the charge dynamics of polymeric semiconductor:ZnO heterostructure*, Journal of Applied Physics **116** (2014).

[60] Y. Wang, W. Wei, X. Liu, and Y. Gu, *Research progress on polymer heterojunction solar cells*, Solar Energy Materials and Solar Cells **98**, 129 (2012).

[61] Q. Shen, Y. Ogomi, S. K. Das, S. S. Pandey, K. Yoshino, K. Katayama, H. Momose, T. Toyoda, and S. Hayase, *Huge suppression of charge recombination in P3HT-ZnO organic-inorganic hybrid solar cells by locating dyes at the ZnO/P3HT interfaces*, Phys. Chem. Chem. Phys. **15**, 14370 (2013).

[62] W. Beek, M. Wienk, and R. Ä. Janssen, *Hybrid Solar Cells from Regioregular Polythiophene and ZnO Nanoparticles*, Advanced Functional Materials **16**, 1112 (2006).

[63] H. Zang, Z. Xu, and B. Hu, *Magneto-Optical Investigations on the Formation and Dissociation of Intermolecular Charge-Transfer Complexes at Donor-Acceptor Interfaces in Bulk-Heterojunction Organic Solar Cells*, The Journal of Physical Chemistry B **114**, 5704 (2010).

[64] Y. Vaynzof, A. A. Bakulin, S. Gélinas, and R. H. Friend, *Direct Observation of Photoinduced Bound Charge-Pair States at an Organic-Inorganic Semiconductor Interface*, Phys. Rev. Lett. **108**, 246605 (2012).

[65] Y.-Y. Lin, Y.-Y. Lee, L. Chang, J.-J. Wu, and C.-W. Chen, *The influence of interface modifier on the performance of nanostructured ZnO/polymer hybrid solar cells*, Applied Physics Letters **94**, 063308 (2009).

[66] H. Spanggaard and F. C. Krebs, *A brief history of the development of organic and polymeric photovoltaics* , Solar Energy Materials and Solar Cells **83**, 125 (2004).

[67] Y. Shi, F. Li, and Y. Chen, *Controlling morphology and improving the photovoltaic performances of P3HT/ZnO hybrid solar cells via P3HT-b-PEO as an interfacial compatibilizer*, New J. Chem. **37**, 236 (2013).

[68] C. Goh, S. R. Scully, and M. D. McGehee, *Effects of molecular interface modification in hybrid organic-inorganic photovoltaic cells*, Journal of Applied Physics **101**, 114503 (2007).

[69] Y.-Y. Lin, T.-H. Chu, S.-S. Li, C.-H. Chuang, C.-H. Chang, W.-F. Su, C.-P. Chang, M.-W. Chu, and C.-W. Chen, *Interfacial Nanostructuring on the Performance of Polymer/TiO2 Nanorod Bulk Heterojunction Solar Cells*, Journal of the American Chemical Society **131**, 3644 (2009).

[70] B. Johann, S. Chyla, M. S. P. Shaffer, J. R. Durrant, D. D. C. Bradley, and J. Nelson, *Hybrid Solar Cells from a Blend of Poly(3-hexylthiophene) and Ligand-Capped TiO2 Nanorods*, Advanced Functional Materials **18**, 622 (2008).

[71] J. Piris, T. E. Dykstra, A. A. Bakulin, P. H. van Loosdrecht, W. Knulst, M. T. Trinh, J. M. Schins, and L. D. Siebbeles, *Photogeneration and Ultrafast Dynamics of Excitons and Charges in P3HT/PCBM Blends*, The Journal of Physical Chemistry C **113**, 14500 (2009).

[72] K. Hara and N. Koumura, *Organic Dyes for Efficient and Stable Dye-Sensitized Solar Cells*, Alternative Energy Photovoltaics, Ionic Liquids, and MOFs , 91 (2009).

[73] K.-C. Liao, H. Anwar, I. G. Hill, G. K. Vertelov, and J. Schwartz, *Comparative Interface Metrics for Metal-Free Monolayer-Based Dye-Sensitized Solar Cells*, ACS Applied Materials and Interfaces **4**, 6735 (2012).

[74] A. Burke, S. Ito, H. Snaith, U. Bach, J. Kwiatkowski, and M. Grätzel, *The Function of a TiO2 Compact Layer in Dye-Sensitized Solar Cells Incorporating Planar Organic Dyes*, Nano Letters **8**, 977 (2008).

[75] E. L. Hanson, J. Schwartz, B. Nickel, N. Koch, and M. F. Danisman, *Bonding Self-Assembled, Compact Organophosphonate Monolayers to the Native Oxide Surface of Silicon*, Journal of the American Chemical Society **125**, 16074 (2003).

[76] S. B. Ambade, R. S. Mane, A. V. Ghule, M. Takwale, A. Abhyankar, B. Cho, and S.-H. Han, *Contact angle measurement: A preliminary diagnostic method for evaluating the performance of ZnO platelet-based dye-sensitized solar cells* , Scripta Materialia **61**, 12 (2009).

[77] B. Thompson and J. Fréchet, *Polymer-fullerene composite solar cells.*, Angew. Chem., Int. Ed. **47**, 58 (2008).

[78] P. Ruankham, S. Yoshikawa, and T. Sagawa, *Effects of the morphology of nanostructured ZnO and interface modification on the device configuration and charge transport of ZnO/polymer hybrid solar cells*, Phys. Chem. Chem. Phys. **15**, 9516 (2013).

[79] D. Bartesaghi, I. del Carmen Pérez, J. Kniepert, S. Roland, M. Turbiez, D. Neher, and L. J. A. Kosteri, *Competition between recombination and extraction of free charges determines the fill factor of organic solar cells*, Nature Communications. **6**, 7083 (2015).

[80] K. Noori and F. Giustino, *Ideal Energy-Level Alignment at the ZnO/P3HT Photovoltaic Interface*, Advanced Functional Materials **22**, 5089 (2012).

[81] Y. Liu, S. R. Scully, M. D. McGehee, J. Liu, C. K. Luscombe, J. M. J. Fréchet, S. E. Shaheen, and D. S. Ginley, *Dependence of Band Offset and Open-Circuit Voltage on the Interfacial Interaction between TiO2 and Carboxylated Polythiophenes*, The Journal of Physical Chemistry B **110**, 3257 (2006).

[82] B. Qi and J. Wang, *Open-circuit voltage in organic solar cells*, J. Mater. Chem. **22**, 24315 (2012).

[83] K. Yuan, F. Li, L. Chen, H. Wang, and Y. Chen, *Understanding the mechanism of poly(3-hexylthiophene)-b-poly(4-vinylpyridine) as a nanostructuring compatibilizer for improving the performance of poly(3-hexylthiophene)/ZnO-based hybrid solar cells*, J. Mater. Chem. A **1**, 10881 (2013).

[84] J. Clark, C. Silva, R. H. Friend, and F. C. Spano, *Role of Intermolecular Coupling in the Photophysics of Disordered Organic Semiconductors: Aggregate Emission in Regioregular Polythiophene*, Phys. Rev. Lett. **98**, 206406 (2007).

[85] H. Sirringhaus, P. J. Brown, R. H. Friend, M. M. Nielsen, K. Bechgaard, B. M. W. Langeveld-Voss, A. J. H. Spiering, R. A. J. Janssen, E. W. Meijer, P. Herwig, and D. M. de Leeuw, *Two-dimensional charge transport in self-organized, high-mobility conjugated polymers* , Nature **401**, 685 (1999).

[86] S. D. Oosterhout, M. M. Wienk, S. S. van Bavel, R. Thiedmann, L. Jan Anton Koster, J. Gilot, J. Loos, V. Schmidt, and R. A. J. Janssen, *The effect of three-dimensional morphology on the efficiency of hybrid polymer solar cells* , Nat Mater **8**, 818 (2009).

[87] R. Österbacka, C. P. An, X. M. Jiang, and Z. V. Vardeny, *Two-Dimensional Electronic Excitations in Self-Assembled Conjugated Polymer Nanocrystals*, Science **287**, 839 (2000).

[88] P. A. van Hal, M. P. T. Christiaans, M. M. Wienk, J. M. Kroon, and R. A. J. Janssen, *Photoinduced Electron Transfer from Conjugated Polymers to TiO2*, The Journal of Physical Chemistry B **103**, 4352 (1999).

[89] X. Jiang, R. Österbacka, O. Korovyanko, C. An, B. Horovitz, R. Janssen, and Z. Vardeny, *Spectroscopic Studies of Photoexcitations in Regioregular and Regiorandom Polythiophene Films*, Advanced Functional Materials **12**, 587 (2002).

[90] G. Dellepiane, C. Cuniberti, D. Comoretto, G. F. Musso, G. Figari, A. Piaggi, and A. Borghesi, *Long-lived photoexcited states in symmetrical polydicarbazolyldiacetylene*, Phys. Rev. B **48**, 7850 (1993).

[91] W. C. Editors: Choy, *Organic Solar Cells, Materials and Device Physics* (Springer, 2013).

[92] O. Epshtein, Y. Eichen, E. Ehrenfreund, M. Wohlgenannt, and Z. V. Vardeny, *Linear and Nonlinear Photoexcitation Dynamics in π-Conjugated Polymers*, Phys. Rev. Lett. **90**, 046804 (2003).

[93] C. Silva, D. M. Russell, A. S. Dhoot, L. M. Herz, C. Daniel, N. C. Greenham, A. C. Arias, S. Setayesh, K. Müllen, and R. H. Friend, *Exciton and polaron dynamics in a step-ladder polymeric semiconductor: the influence of interchain order*, Journal of Physics: Condensed Matter **14**, 9803 (2002).

[94] C. Silva, A. S. Dhoot, D. M. Russell, M. A. Stevens, A. C. Arias, J. D. MacKenzie, N. C. Greenham, R. H. Friend, S. Setayesh, and K. Müllen, *Efficient exciton dissociation via two-step photoexcitation in polymeric semiconductors*, Phys. Rev. B **64**, 125211 (2001).

[95] S. Gélinas, O. Paré-Labrosse, C.-N. Brosseau, S. Albert-Seifried, C. R. McNeill, K. R. Kirov, I. A. Howard, R. Leonelli, R. H. Friend, and C. Silva, *The Binding Energy of Charge-Transfer Excitons Localized at Polymeric Semiconductor Heterojunctions*, The Journal of Physical Chemistry C **115**, 7114 (2011).

[96] C.-N. Brosseau, M. Perrin, C. Silva, and R. Leonelli, *Carrier recombination dynamics in $In_xGa_{1-x}N/GaN$ multiple quantum wells*, Phys. Rev. B **82**, 085305 (2010).

[97] A. E. Colbert, E. M. Janke, S. T. Hsieh, S. Subramaniyan, C. W. Schlenker, S. A. Jenekhe, and D. S. Ginger, *Hole Transfer from Low Band Gap Quantum Dots to Conjugated Polymers in Organic/Inorganic Hybrid Photovoltaics*, The Journal of Physical Chemistry Letters **4**, 280 (2013).

[98] K. M. Noone, S. Subramaniyan, Q. Zhang, G. Cao, S. A. Jenekhe, and D. S. Ginger, *Photoinduced Charge Transfer and Polaron Dynamics in Polymer and Hybrid Photovoltaic Thin Films: Organic vs Inorganic Acceptors*, The Journal of Physical Chemistry C **115**, 24403 (2011).

[99] M. Berberan-Santos, E. Bodunov, and B. Valeur, *Mathematical functions for the analysis of luminescence decays with underlying distributions 1. Kohlrausch decay function (stretched exponential)*, Chemical Physics **315**, 171 (2005).

[100] M. T. Lloyd, R. P. Prasankumar, M. B. Sinclair, A. C. Mayer, D. C. Olson, and J. W. P. Hsu, *Impact of interfacial polymer morphology on photoexcitation dynamics and device performance in P3HT/ZnO heterojunctions*, J. Mater. Chem. **19**, 4609 (2009).

[101] D. C. Olson, S. E. Shaheen, R. T. Collins, and D. S. Ginley, *The Effect of Atmosphere and ZnO Morphology on the Performance of Hybrid Poly(3-hexylthiophene)/ZnO Nanofiber Photovoltaic Devices*, The Journal of Physical Chemistry C **111**, 16670 (2007).

[102] C. Deibel, D. Mack, J. Gorenflot, A. Schöll, S. Krause, F. Reinert, D. Rauh, and V. Dyakonov, *Energetics of excited states in the conjugated polymer poly(3-hexylthiophene)*, Phys. Rev. B **81**, 085202 (2010).

[103] J.-W. van der Horst, P. A. Bobbert, M. A. J. Michels, and H. Bassler, *Calculation*

of excitonic properties of conjugated polymers using the Bethe-Salpeter equation, The Journal of Chemical Physics **114**, 6950 (2001).

[104] M. C. Gwinner, Y. Vaynzof, K. K. Banger, P. K. H. Ho, R. H. Friend, and H. Sirringhaus, *Solution-Processed Zinc Oxide as High-Performance Air-Stable Electron Injector in Organic Ambipolar Light-Emitting Field-Effect Transistors*, Advanced Functional Materials **20** (2010).

[105] M. Onoda, K. Tada, A. Zakhidov, and K. Yoshino, *Photoinduced charge separation in photovoltaic cell with heterojunction of p- and n-type conjugated polymers* , Thin Solid Films **331**, 76 (1998).

[106] O. Epshtein, G. Nakhmanovich, Y. Eichen, and E. Ehrenfreund, *Dispersive dynamics of photoexcitations in conjugated polymers measured by photomodulation spectroscopy*, Phys. Rev. B **63**, 125206 (2001).

[107] J. D. Plumhof, T. Stöferle, L. Mai, U. Scherf, and R. F. Mahrt, *Room-temperature Bose-Einstein condensation of cavity exciton-polaritons in a polymer*, Nature materials **13**, 247 (2014).

[108] H. Zoubi and G. C. La Rocca, *Exciton-polariton kinematic interactions in organic microcavities*, Phys. Rev. B **77**, 159905 (2008).

[109] W. Barford, *Exciton transfer integrals between polymer chains*, The Journal of Chemical Physics **126** (2007).

[110] B. J. Schwartz, *CONJUGATED POLYMERS AS MOLECULAR MATERIALS: How Chain Conformation and Film Morphology Influence Energy Transfer and Interchain Interactions*, Annual Review of Physical Chemistry **54**, 141 (2003).

[111] A. Köhler, S. T. Hoffmann, and H. Bässler, *An Order-Disorder Transition in the Conjugated Polymer MEH-PPV*, Journal of the American Chemical Society **134**, 11594 (2012).

[112] H. Yamagata, N. J. Hestand, F. C. Spano, A. Köhler, C. Scharsich, S. T. Hoffmann, and H. Bässler, *The red-phase of poly[2-methoxy-5-(2-ethylhexyloxy)-1,4-phenylenevinylene] (MEH-PPV): A disordered HJ-aggregate*, The Journal of Chemical Physics **139**, 114903 (2013).

[113] K. Sripathy, R. W. MacQueen, J. R. Peterson, Y. Y. Cheng, M. Dvorak, D. R. McCamey, N. D. Treat, N. Stingelin, and T. W. Schmidt, *Highly efficient photochemical upconversion in a quasi-solid organogel*, J. Mater. Chem. C **3**, 616 (2015).

[114] J. F. Visjager, *Ultra-High Molecular Weight Polymers Processing and Properties of Polyethylene and Poly(tetrafluoroethylene)*, PhD thesis, Eidegenössische Technische Hochschule Zürich, 2001.

[115] K. W. Howard A. Barnes, John Fletcher Hutton, *An introduction to Rheology* (Elsevier, 1989).

[116] M. Kasha, *Characterization of electronic transitions in complex molecules*, Discuss. Faraday Soc. **9**, 14 (1950).

[117] Q. G. Zeng and Z. J. Ding, *Photoluminescence and Raman spectra study of paraphenylenevinylene at low temperatures*, Journal of Physics: Condensed Matter **16**, 5171.

[118] G. Wantz, L. Hirsch, N. Huby, L. Vignau, A. S. Barriére, and J. P. Parneix, *Temperature-dependent electroluminescence spectra of poly(phenylene-vinylene) derivatives-based polymer light-emitting diodes*, Journal of Applied Physics **97**, 034505 (2005).

[119] M. A. T. da Silva, I. F. L. Dias, J. L. Duarte, E. Laureto, I. Silvestre, L. A. Cury, and P. S. S. Guimarães, *Identification of the optically active vibrational modes in the photoluminescence of MEH-PPV films*, The Journal of Chemical Physics **128**, 094902 (2008).

[120] T. W. Hagler, K. Pakbaz, K. F. Voss, and A. J. Heeger, *Enhanced order and electronic delocalization in conjugated polymers oriented by gel processing in polyethylene*, Phys. Rev. B **44**, 8652 (1991).

[121] C. J. Collison, L. J. Rothberg, V. Treemaneekarn, , and Y. Li, *Conformational Effects on the Photophysics of Conjugated Polymers: A Two Species Model for MEH-PPV Spectroscopy and Dynamics*, Macromolecules **34**, 2346 (2001).

[122] J. M. Lupton, *Single-Molecule Spectroscopy for Plastic Electronics: Materials Analysis from the Bottom-Up*, Advanced Materials **22**, 1689 (2010).

[123] T. J. Pundsack, *Exciton Dynamics in Alternative Solar Cell Materials: Polymers, Nanocrystals, and Small Molecules*, PhD thesis, THE UNIVERSITY OF MINNESOTA, 2014.

Appendix I

Calculation of the surface coverage of dye molecules on the surface of ZnO nanocrystals

The carboxyl group from N3 and phosphonic acid group from 6TP can strongly graft to the surface of ZnO. In the following, we did a roughly calculation of the surface coverage of dye molecules on the surface of ZnO nanocrystals.

N3 Dye concentration: (1) 0.01 wt% (2) 0.1 wt% (3) 0.5 wt%.
ZnO concentration: 20 mg/ml, so the concentration of N3(1) was 0.001 mg/ml, N3(2) was 0.02 mg/ml and N3(3) was 0.1 mg/ml, when 0.1 wt% N3 molecule was used.

N3-dye molecule amount $= \frac{m}{M} \times 6.02 \times 10^{23} = \frac{0.02 \times 10^{-3}}{705.648} \times 6.02 \times 10^{23} = 1.77 \times 10^{16}$.
Suppose that the surface area of each dye molecule is $(2 \times 2)\,\mathrm{nm}^2$.
The total surface area of N3 molecules $= 1.77 \times 10^{16} \times (2 \times 10^{-9})^2 = 0.068\,\mathrm{m}^2$.
Surface area of each nanocrystal (Radius = 5 nm) $= 4\pi R^2 = 4\pi \times (5 \times 10^{-9})^2 = 3.14 \times 10^{-16}\,\mathrm{m}^2$.
Volume of total used ZnO nanocrystals: $V_{total} = m/\rho = 20 \times 10^{-3}/5.6 = 3.57 \times 10^{-9}\,\mathrm{m}^3$.
Volume of each ZnO nanocrystal (Radius = 5 nm): $\mathrm{V}_{nanocrystal} = \frac{4}{3}\pi R^3 = \frac{4}{3}\pi \times (5 \times 10^{-9})^3 = 5.23 \times 10^{-25}\,\mathrm{m}^3$.
Number of ZnO nanocrystals $= V_{total}/V_{nanocrystal} = 6.8 \times 10^{15}$.
The total surface area $= 6.8 \times 10^{15} \times 3.14 \times 10^{-16} = 2.135\,\mathrm{m}^2$.
Surface coverage ratio $= 0.068/2.13 = 0.032 = 3.2\%$.

We did a similar calculation for 6TP as well. According to the above calculation, when dye molecular content is at 0.01 wt% and 0.1 wt%, since the carboxyl group from N3 and phosphonic acid group from 6TP can strongly graft to the surface at ZnO. Almost 100% of N3 and 6TP assumed to have attached to the ZnO nanocrystals.

Appendix II

Journal Publications and presentations

Publications:

1) **Elham Rezasoltani**, Mingqing Wang, Ian G. Hill and Carlos Silva, *"The influence of molecular interface modification on the charge dynamics of polymeric semiconductor: ZnO heterostructure"*, Journal of Applied Physics 116(7): 074502-7, 2014, DOI: 10.1063/1.4893361.

2) **Elham Rezasoltani**, Jaime Martin Perez, Claudia M. Bazan, Natalie Stingelin and Carlos Silva *"Formation of a highly ordered red phase in a MEH-PPV:polystyrene gel"*, to be submitted to the journal of Macromolecules.

3) **Elham Rezasoltani**, Ester Buchaca-Domingo, Natalie Banerji, Natalie Stingelin, and Carlos Silva *"Controlling charge generation and recombination dynamics in semicrystalline polymer: fullerene blends with tailored phase morphology"*, invited review paper for Journal of Material Chemistry C, In preparation.

4) Fei Dou, Ester Buchaca-Domingo, Maciej Sakowicz, **Elham Rezasoltani**, Thomas McCarthy-Ward, Martin Heeney, Xinping Zhang, Natalie Stingelin, Carlos Silva *"The effect of phase morphology on the nature of long-lived charges in semiconductor polymer:fullerene systems"*, J. Mater. Chem. C, 2015, 3, 3722-3729 DOI: 10.1039/C4TC02637C.

5) P. Krstajic, **E. Rezasoltani**, P. vasilopoulos, *"Spin-dependent transport in waveguides with spatially modulated strengths of the Rashba and Dresselhaus terms of the spin-orbit interaction"* ,Phys. Rev. B 81, 155325, 2010.

Oral presentations:

December 2015, Material Research Society (MRS) Fall meeting, Boston Massachusetts, USA, **Elham Rezasoltani**, Jaime Martin Perez, Claudia M. Baz·n, Natalie Stingelin and Carlos Silva *"Formation of a highly ordered red phase in a MEH-PPV:polystyrene gel"*.

April 2015, MRS Spring meeting, San Francisco, California, USA, **Elham Rezasoltani**,

Pascal Grégoire, Eleonora Vella, Claudia Marcela Bazan, James H. Bannock, John de Mello, and Carlos Silva, *"The interplay of intra- and intermolecular excitonic coupling in regioregular poly(3-hexylthiophene)"*. (Due to the visa issue this talk was presented by Eleonora Vella)

June 2014, Canadian Association of Physics (CAP) Congress, Sudbury, ON, CA, **Elham Rezasoltani**, Mingqing Wang, Ian G. Hill, et Carlos Silva, *"The Influence of molecular interface modification on the charge dynamics of polymeric semiconductor / ZnO heterostructure"*.

Selected Poster presentations:

June 2014, IEEE PVSC 39 conference, Denver, Colorado, USA, **Elham Rezasoltani**, Mingqing Wang, Ian G. Hill and Carlos Silva, ?The influence of interface modification on the charge dynamics of polymeric semiconductor/ ZnO heterostructure".

May 2014, Next generation solar conference, Montreal, CA, **Elham Rezasoltani**, Mingqing Wang, Ian G. Hill and carlos Silva, *"The influence of interface modification on the charge dynamics of polymeric semiconductor/ZnO heterostructure"*.

May 2014, RQMP conference, Montreal, CA, **Elham Rezasoltani**, Mingqing Wang, Ian G. Hill and carlos Silva, *"The influence of interface modification on the charge dynamics of polymeric semiconductor/ZnO heterostructure"*.

December 2013, MRS Fall meeting, Boston Massachusetts, USA, **Elham Rezasoltani**, Mingqing Wang, Ian G. Hill and carlos Silva, *"The influence of interface modification on the charge dynamics of polymeric semiconductor/ZnO heterostructure"*.

May 2013, CAP Congress, Montreal, CA, **Elham Rezasoltani**, Mingqing Wang, Ian G. Hill and carlos Silva, *"The influence of interface modification on the charge dynamics of polymeric semiconductor/ZnO heterostructure"*.

May 2013, Next generation solar conference, Montreal, CA, **Elham Rezasoltani**, Mingqing Wang, Ian G. Hill and carlos Silva, *"The influence of interface modification on the charge dynamics of polymeric semiconductor/ZnO heterostructure"*.

May 2013, RQMP, Montreal, CA, **Elham Rezasoltani**, Mingqing Wang, Ian G. Hill and carlos Silva, *"The influence of interface modification on the charge dynamics of poly-*

meric semiconductor/ZnO heterostructure".

Stays in recognised centers:

February-May 2015, Prof. Natalie Stingelin's group. Preparation of ultra high molecular weight Polystyrene/MEH-PPV gel. Department of Materials, Imperial College London, London, UK.

July 2014, Prof. Alejandro Briseno's group. Preparation and fabrication of Pentacene solar cells, Department of Polymer Science and Engineering, University of Massachusetts Amherst, Amherst, MA, USA.

August 2013 , Solar Cell Fabrication Hands-On Training Program, at McMaster University, Hamilton, ON, CA.

March 2013 , Dr. Ian G. Hill's group. Fabricated hybrid organic/inorganic photovolatic devices, utilized photolithography, bell jar thermal evaporation system and reactive ion etching for device fabrication, tested devices using a Newport solar simulator, Dalhousie University, Halifax, NV, CA.